

Multi-scale modelling of thermal shock damage in refractory materials

Citation for published version (APA):

Özdemir, I. (2009). *Multi-scale modelling of thermal shock damage in refractory materials*. [Phd Thesis 1 (Research TU/e / Graduation TU/e), Mechanical Engineering]. Technische Universiteit Eindhoven.
<https://doi.org/10.6100/IR643228>

DOI:

[10.6100/IR643228](https://doi.org/10.6100/IR643228)

Document status and date:

Published: 01/01/2009

Document Version:

Publisher's PDF, also known as Version of Record (includes final page, issue and volume numbers)

Please check the document version of this publication:

- A submitted manuscript is the version of the article upon submission and before peer-review. There can be important differences between the submitted version and the official published version of record. People interested in the research are advised to contact the author for the final version of the publication, or visit the DOI to the publisher's website.
- The final author version and the galley proof are versions of the publication after peer review.
- The final published version features the final layout of the paper including the volume, issue and page numbers.

[Link to publication](#)

General rights

Copyright and moral rights for the publications made accessible in the public portal are retained by the authors and/or other copyright owners and it is a condition of accessing publications that users recognise and abide by the legal requirements associated with these rights.

- Users may download and print one copy of any publication from the public portal for the purpose of private study or research.
- You may not further distribute the material or use it for any profit-making activity or commercial gain
- You may freely distribute the URL identifying the publication in the public portal.

If the publication is distributed under the terms of Article 25fa of the Dutch Copyright Act, indicated by the "Taverne" license above, please follow below link for the End User Agreement:

www.tue.nl/taverne

Take down policy

If you believe that this document breaches copyright please contact us at:

openaccess@tue.nl

providing details and we will investigate your claim.

Multi-scale Modelling of Thermal Shock Damage in Refractory Materials

İzzet Özdemir

CIP-DATA LIBRARY TECHNISCHE UNIVERSITEIT EINDHOVEN

Özdemir İzzet

Multi-scale modelling of thermal shock damage in refractory materials.

Eindhoven University of Technology, 2009.

Proefschrift.

A catalogue record is available from the Eindhoven University of Technology Library.

ISBN: 978-90-386-1892-0

This thesis is prepared with L^AT_EX₂_ε

Cover design: Niels Groenendijk

Printed by the Universiteitsdrukkerij TU Eindhoven, Eindhoven, The Netherlands.

Multi-scale Modelling of Thermal Shock Damage in Refractory Materials

PROEFSCHRIFT

ter verkrijging van de graad van doctor aan de
Technische Universiteit Eindhoven, op gezag van de
rector magnificus, prof.dr.ir. C.J. van Duijn, voor een
commissie aangewezen door het College voor
Promoties in het openbaar te verdedigen
op donderdag 2 juli 2009 om 16.00 uur

door

İzzet Özdemir

geboren te Afyon, Turkije

Dit proefschrift is goedgekeurd door de promotor:

prof.dr.ir. M.G.D. Geers

Copromotor:

dr.ir. W.A.M. Brekelmans

Contents

Summary	ix
1 Introduction	1
2 A Thermo-mechanical Cohesive Zone Model	5
2.1 Introduction	6
2.2 Interface Heat Conductance and Thermal Expansion	7
2.3 Thermo-mechanics	11
2.4 Thermo-mechanical Analysis of a Granular Microstructure	15
2.5 Conclusion and Outlook	17
2.6 Appendix	18
3 Modelling Thermal Shock Damage in Refractory Materials via Direct Numerical Simulation (DNS)	21
3.1 Introduction	22
3.2 Material Microstructure	24
3.3 Experimental Characterization of Thermal Shock Response	24
3.4 Direct Numerical Simulation (DNS) of Thermal Shock Experiments	26
3.4.1 Grains	28
3.4.2 Matrix	28
3.4.3 Interfaces	32
3.4.4 Solution procedure	34
3.4.5 Parameter identification procedure	35
3.4.6 Parametric study	36
3.5 Summary and Conclusion	42
4 Computational Homogenization for Heat Conduction in Heterogeneous Solids	45
4.1 Introduction	46
4.2 Preliminaries	48
4.3 Formulation of the Thermal Problem at Both Scales	50
4.3.1 Micro-scale problem	50
4.3.2 Macro-scale problem	51

4.4	Scale Transitions	52
4.4.1	The macro-micro scale transition	52
4.4.2	Micro-scale RVE boundary conditions	54
4.4.3	The micro-macro scale transition	54
4.5	Two-Scale Numerical Solution Strategy	56
4.5.1	RVE boundary value problem	56
4.5.2	Extraction of the macroscopic heat flux	58
4.5.3	Extraction of the macroscopic conductivity	59
4.5.4	Nested solution strategy	60
4.6	Two-scale Homogenization Examples	61
4.6.1	Thermal homogenization in a cellular foam-like structure	61
4.6.2	Thermal homogenization in refractory-like materials	63
4.7	Summary and Conclusion	65
5	FE² Computational Homogenization for the Thermo-mechanical Analysis of Heterogeneous Solids	69
5.1	Introduction	70
5.2	Preliminaries	71
5.3	Micro and Macro-scale Problem Formulations	72
5.3.1	Micro-scale problem	72
5.3.2	Macro-scale problem	73
5.4	Scale transitions	74
5.4.1	The macro-micro scale transition	74
5.4.2	The micro-macro scale transition	76
5.5	Two-scale Numerical Solution Framework	77
5.5.1	Macroscopic boundary value problem	78
5.5.2	RVE level boundary value problem	79
	RVE-BVP coupled to the macroscopic thermal pass	79
	Extraction of the macroscopic heat flux	82
	Extraction of the macroscopic conductivity	82
	RVE-BVP coupled to the macroscopic mechanical pass	83
	Extraction of the macroscopic stresses	84
	Extraction of the macroscopic stiffness	85
5.6	Two-scale Homogenization Examples	86
5.6.1	Thermo-mechanically loaded plate	86
5.6.2	Thermally shocked channel	89
5.7	Summary and Conclusion	91
6	Multi-scale Thermo-mechanical Analysis of a Ladle Refractory Lining	95
6.1	Introduction	96
6.2	Representative Volume Element	96
6.3	Macroscopic Boundary Value Problem	97
6.4	Analysis Results	99
6.5	Summary and Conclusion	102

7 Conclusion and Outlook	103
Bibliography	107
Samenvatting	117
Acknowledgements	121
Curriculum Vitae	123

Multi-scale Modelling of Thermal Shock Damage in Refractory Materials

Summary

Refractories are high-temperature resistant materials used extensively in many engineering structures and assemblies in a wide spectrum of applications ranging from metallurgical furnace linings to thermal barrier coatings. Such structures are often exposed to severe thermal loading conditions in the form of rapid temperature changes (thermal shock) and/or temperature cycles. The understanding and modelling of the failure processes are definitely necessary to achieve reliable life-time predictions of the existing structures and to develop design rules for improvement.

Due to their high temperature resistance, alumina based refractory ceramics with a porous granular microstructure being far from homogenous are commonly used in the applications as mentioned above. In such heterogeneous material systems, local thermal expansion (CTE) mismatches, non-uniformities and anisotropy of the different constituents naturally lead to the appearance of internal stresses which are essentially the driving mechanisms for micro-cracking and damage. Under highly transient external thermal loading conditions, the resulting heterogeneous temperature distribution may lead to a complicated mechanical response along with a non-uniform mechanical and physical property degradation accompanied by irreversible geometry changes. The altered distribution of the mechanical properties dictates the macroscopic response when the external loading is further varied. Therefore, a strong coupling between the evolving microstructure and the macroscopic response arises. Moreover, microstructural configurational changes may trigger a significant interaction between the mechanical and thermal fields, for instance due to a reduced heat transport across a damaged interface. Therefore, an approach taking into account these mechanisms sufficiently well would render a versatile tool to improve the understanding of the influence of mechanical and thermal properties at the constituent level and their mutual interaction from a microstructural perspective.

In this thesis, a concurrent multi-scale framework for the thermo-mechanical analysis of heterogeneous materials is proposed, with a particular focus on coarse grained refractory ceramics. The framework is essentially based on a rigorous extension of the well established FE² computational homogenization technique, where the local macroscopic response is determined through the solution of a boundary value problem defined on a representative volume of the underlying microstructure. At first, the computational homogenization ideas are explored in the context of pure heat conduction processes in heterogeneous solids. Subsequently, the framework for coupled

thermo-mechanical analyses is constructed by combining the first order mechanical homogenization with the dual procedure developed for heat conduction, within an operator-split (or staggered) solution algorithm which is composed of incrementally uncoupled nested (FE²) solution blocks for thermal and mechanical equilibrium sub-problems.

For predictive computations, the mechanical and thermophysical properties of individual phases and interfaces at the microstructural level are required, which is a distinctive characteristic of such a multi-scale approach. Due to the lack of material data, particularly for interfaces, direct numerical simulations (DNS) are exploited to identify the parameters inversely by using a limited set of molten aluminium thermal shock test results. On the basis of a microstructure composed of mutually non-contacting large grains embedded in a homogeneous matrix reflecting a compound of very fine grains, molten aluminium thermal shock tests are reproduced in full detail under realistic boundary conditions and a computational procedure is developed to determine the damage distribution along the specimen which is compared to experimental results. The failure mechanisms at the matrix-grain interface level are resolved by introducing thermo-mechanical cohesive zone elements not only capable of accounting for the mechanical decohesion but also including the reduced heat transport through the mechanically damaged interfaces. Fine scale micro-cracks within the matrix are smeared out by using a well-established continuum damage mechanics formulation which is free of any pathological localization and mesh sensitivity problems. Direct numerical simulation of thermal shock tests has also served for the investigation of short range effects (due to the local CTE mismatch) and long range effects (elastic fields accompanying the temperature gradient) on the resulting thermo-mechanical damage profile, through variations of different microstructural material parameters.

In the last part of the thesis, predictive capabilities of the developed analysis framework are assessed by means of the two-scale analysis of a real size ladle refractory lining, based on the microstructural parameters identified through direct numerical simulations.

CHAPTER ONE

Introduction

In materials engineering, the term 'refractory' is used to indicate the class of materials which are resistant to harsh thermal environments and typically used in high temperature applications. The performance of high temperature resistant materials is decisive on the reliability and functionality of many engineering structures ranging from industrial furnace linings to thermal barrier coatings.

Under operation conditions, for instance in industrial furnaces, the temperatures reach extremely high values, which requires materials with high melting and transformation temperatures. Furthermore, there are other adverse effects, e.g. chemical interaction with the molten metal and slag, which threaten the integrity of the material and influences the selection of the material system for a specific application. Therefore, manufacturing and selection of high temperature resistant materials is a multi-faceted problem governed by multiple criteria.

Manufacturing of refractory materials is heavily based on oxides, e.g. Al_2O_3 , due to their relatively high melting temperatures. Through the sintering process, individual grains of the initial mix build up a coherent, unified microstructure as exemplified in figure 1.1. Under severe thermal conditions, the overall material response is dictated by the collective behaviour of individual components and interfaces.

When a refractory material experiences a temperature change, due to its heterogeneous microstructure, individual phases with different thermal expansion characteristics tend to expand/contract in a different way from the neighbouring phases, leading to micro-stresses. Furthermore, a temperature change within the material, in general, occurs in a non-uniform way due to sudden changes of the ambient temperature, e.g. thermal shock type loading. Non-uniformity of the temperature change induces non-uniform thermal strains and in turn micro-stresses within the material. As the stresses reach significant levels, damage and cracking at the micro level initiates which is the basis for mechanical and physical property degradation observed at the macro level. Models incorporating the associated micro-mechanisms would be

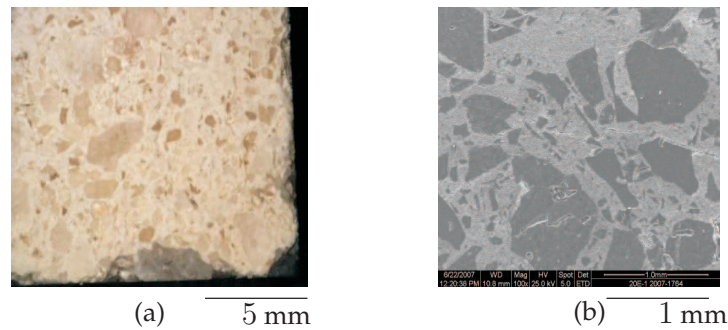


Figure 1.1: Typical microstructure of coarse grained refractory ceramics (Alumina-mullite composite), (a) light microscope image, (b) TEM image

instrumental to investigate the microstructural effects on the macroscopic properties and are desirable to assess the significance of microstructural parameters in view of designing an optimum microstructural lay-out for a particular application.

The development of analysis and predictive tools to determine the thermo-mechanical response of refractory materials have elucidated researchers for many years starting with the early works of Kingery and Hasselmann, [1–3]. In these works, quenching tests on fine grained technical ceramics were conducted and interesting relations between average grain size and residual strength were observed. Considering an equivalent homogeneous medium, analytical techniques based on linear elasticity and fracture mechanics were developed and confronted with the quenching test results. However, capturing the peculiar microstructural dependency of residual strength was out of scope with the analysis approaches developed. Different characteristic parameters reflecting different regimes, e.g. crack initiation and crack propagation, were devised to rank the resistance of materials under thermal shock loading conditions. However, contradictory rankings result [3–5], which indicated the necessity to unify the elaboration of different regimes as done in [6]. That study serves well to classify the materials in terms of thermal shock resistance on the basis of ‘homogenized’ macroscopic properties without giving any attention to the heterogeneous microstructure of refractories.

Focusing on the micro-mechanisms under uniform temperature change, analyses of geometrically simplified microstructural systems, e.g. a single grain embedded in a matrix or an array of hexagonal grains, have been carried out, [7–10]. These studies were useful to capture the grain size dependency of thermally induced micro-cracking, critical sites of crack initiation, the influence of mechanical and thermal anisotropy. Making use of the cohesive zone concept in a finite element framework, geometrically more complex granular assemblies were analyzed to investigate the sensitivity of microstructural parameters, [11, 12]. In these studies, the boundary conditions were prescribed whereas in a real material system, the strain and temperature change at a certain material point is intimately related to the local material properties. Under highly transient external thermal loading conditions, the resulting heterogeneous temperature distribution may lead to a complicated mechanical response and a non-uniform mechanical and physical property degradation accom-

panied by irreversible geometrical changes. An altered distribution of properties dictates the macroscopic response when the external loading is further varied. Therefore, a strong coupling between the evolving microstructure and the macroscopic response arises. For a realistic analysis, the link between the macro scale boundary conditions and the microscopic response should be constructed in a consistent way.

Concurrent multi-scale methods, which have been an active research field in the last decade, address the coupling of hierarchical scales with a wide range of constitutive models and damage mechanisms that can be embedded into the fine scale behaviour of heterogeneous materials, [13–20]. Instead of using a classical constitutive law at the macro scale, the macroscopic stresses are obtained from the solution of a boundary value problem (BVP) defined on a representative volume of the underlying material. Relying on the well-established constitutive descriptions that can be used for experimentally identified individual phases, the empirical character associated with phenomenological modeling approaches for heterogeneous material systems, is reduced. As opposed to classical constitutive models, mechanical and thermo-physical properties of the individual phases and interfaces are necessary to construct this framework and to carry out predictive computations. For well-identified phases, existing material data bases are quite useful but determination of interface characteristics and very fine composite phase characteristics are not straightforward and poses some experimental challenges as well. At the current state, inverse methods of parameter identification seem to be the only alternative which requires direct numerical simulation (DNS) techniques in the context of heterogeneous material system characterization.

Scope and Outline of the Thesis

In this thesis, a concurrent multi-scale framework for the thermo-mechanical analysis of heterogeneous materials is proposed along with a methodology to identify the parameters of a typical refractory material by means of a direct numerical simulation (DNS) technique. Focusing on coarse-grained refractory ceramics, first the failure mechanisms at the microstructural level are worked out by means of proper constitutive descriptions. To this end, in the second chapter, a thermo-mechanical cohesive zone formulation is presented, addressing not only the mechanical decohesion but also the reduced heat transport through the material interfaces. Due to the lack of material parameters at the microstructural level, a limited set of molten aluminium thermal shock test results are used to determine the material parameters inversely in chapter 3. A direct numerical simulation (DNS) technique is employed where the test specimens are reproduced in full detail and the essential micro-damage mechanisms are incorporated by means of thermo-mechanical cohesive zone elements at the interfaces and an implicit gradient damage mechanics formulation for the matrix. Following the thermal loading history, in order to determine the thermal shock damage along the sample, an equivalent procedure is developed and the results are compared with the experimentally determined damage distributions based on dynamic

Young's Modulus measurements. Furthermore, the influence of various parameters on the resulting damage profiles are investigated with the same direct numerical simulation framework. In chapter 4, exploiting the ideas of computational homogenization techniques for purely mechanical problems, an appropriate multi-scale framework is developed for heat conduction in heterogeneous solids. Subsequently in chapter 5, the framework for thermo-mechanical analyses is constructed by combining the first order mechanical homogenization with the procedure developed for heat conduction, within an operator-split solution algorithm which is composed of incrementally uncoupled nested (FE²) solution blocks for thermal and mechanical equilibrium subproblems. Thereafter, the predictive capabilities of the developed analysis framework are assessed by means of a two-scale analysis of a real size ladle refractory lining, in combination with microstructural parameters identified through direct numerical simulations. Finally the thesis closes with a conclusion and outlook chapter, in which the significance, advantages and disadvantages of the proposed framework are highlighted along with reflections on possible improvements and issues that can be addressed in future work.

A Thermo-mechanical Cohesive Zone Model¹

Abstract

In this chapter, a cohesive zone formulation that is suitable for the thermo-mechanical analysis of heterogeneous solids and structural systems with contacting/interacting components, is presented. Well established traction-opening relations are adopted and combined with micromechanically motivated heat flux-opening relations reflecting the evolving heat transfer through the interfaces. The finite element approach for a coupled analysis within an operator-split solution framework is presented and demonstrated with an example problem.

¹*Based on: I. Özdemir, W.A.M. Brekelmans, M.G.D. Geers (2008). A Thermo-mechanical Cohesive Zone Model. to be submitted.*

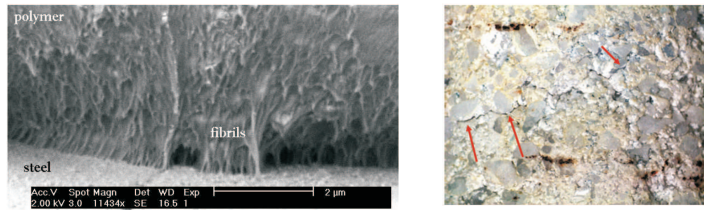


Figure 2.1: Cohesive cracking in different materials, reproduced from [21]

2.1 Introduction

For heterogeneous materials and multilayered structural systems, in general, interfaces are the weakest links. Knowledge and understanding of thermo-mechanical and physical features and behaviour of interfaces are of utmost importance to improve the performance and reliability of these material systems and engineering structures.

The basic tool for predicting failure of interfaces is linear elastic fracture mechanics (LEFM), which is limited essentially by the bulk constitutive response and the size of the fracture process zone as compared to the crack size. Furthermore, the LEFM solution cannot capture the real stress distribution at the vicinity of the crack tip. These limitations have been removed by the introduction of the ‘cohesive zone’ concept, which basically removes the crack tip singularity by employing a traction-opening law that reflects the limited strength of the material and the mechanisms of load transfer taking place within the fracture process zone, see figure 2.1. Typically, the interfacial details are not resolved explicitly and the associated load transfer mechanisms are lumped into cohesive zone constitutive relations (traction-opening relations). This approach has been used successfully for the prediction of failure of interfaces subjected to many different boundary conditions, see [21,22] and the cited references therein.

A vast amount of literature exists starting with the seminal work of Xu and Needleman [23], whereby the majority of papers focuses on the mechanical characteristics of the interfaces only. However, for a large number of cases, the actual loading case also includes severe temperature changes (thermal shock) and thermal cycles (thermo-mechanical fatigue) exposed to the system. As discontinuities (cracks) initiate and propagate, they act as barriers for heat flow, therefore affecting the evolving temperature profile within the solid. This clearly influences the thermal strains and may alter the mechanical response significantly in return. Meso-level modeling of concrete failure under fire and the reliability analysis of thermal protection layers are two examples which necessitate a proper thermo-mechanical interface description at different scales as presented in [24] and [25].

Within the framework of continuum thermodynamics, a thermo-mechanical interface description with damage is presented in [26], though it lacks some physical motivation for certain arguments. Similarly, the authors of [27] present a continuum

interface model which is to some extent, independent of the bulk, equipped with its particular thermodynamical potentials and connected/coupled to the bulk by certain assumptions. Furthermore, it requires some extra effort to convert the formulation into a favorable format considering implementation aspects, [28]. Motivated by ductile fracture problems, [29] presents a similar formulation in the sense that the interface has its own thermodynamical potentials and an efficient discretization is realized within an X-FEM framework.

Alternatively, [30] proposes a micromechanically motivated thermo-mechanical cohesive zone description for fiber-reinforced ceramic matrix composites, which however does not take into account the thermal strains of the bridging fibers. Pursuing a phenomenological approach, the same authors presented a model, [25], [30] where the heat transfer along the interface is neglected. Though it is sufficient for the loading conditions considered in these studies, in some other cases (e.g. mode II dominated situations), a more rigorous heat flow analysis may become necessary.

Considering idealized load and heat transfer mechanisms suggests to construct the thermal response of all micro-mechanisms and separating materials involved as the basis for quantifying heat transfer across the cohesive zone. Therefore, the conductivity of the bridging fibers or fibrils and the air within the crack enclosure determines the conductivity attributed to the cohesive zone model, see figure 2.1. Furthermore, thermal expansion of these microstructural components reveals itself as thermal strains in the corresponding traction-opening law and has to be taken into account properly. Moreover, in analogy with the mechanical response, at the crack tip a singularity in the temperature gradient arises [31], which can be effectively handled by introducing the thermal/cohesive zone concept.

It is the aim in the present chapter to develop a physically motivated, complete thermo-mechanical cohesive zone model including its finite element formulation, which can be used at the meso-level modeling of heterogenous materials and multi-layered structures.

In the next section, the heat transfer across a partially open interface is presented which is the basis for the heat flux-opening relations. The mechanical counter part of the problem is presented in section 3 within a thermo-mechanical context for the sake of completeness. Thereafter, a finite element formulation, which uses the presented interface constitutive laws and a solution algorithm based on the operator-split technique, is briefly summarized. An example problem is elaborated to demonstrate the merits of the presented formulation.

2.2 Interface Heat Conductance and Thermal Expansion

In case of heat flow, across a partially open cohesive crack, a temperature jump between the two faces of the discontinuity is observed since the coupling between the

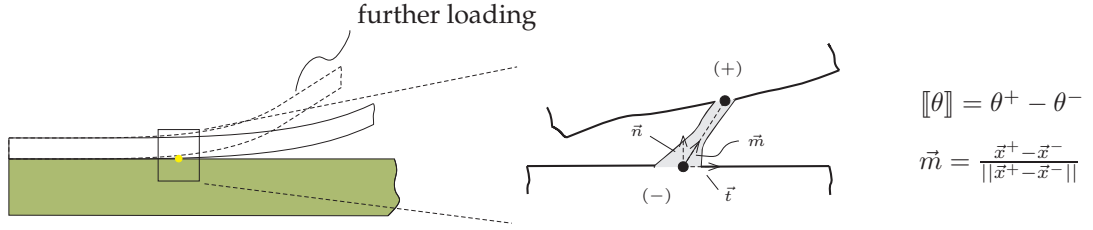


Figure 2.2: Discontinuity splitting a material point

interfacial load and heat transfer mechanisms are not explicitly resolved in a cohesive zone model. It is important to note that the heat flux through crack bridging matter (e.g. fibrils) has a certain direction which has to be properly accounted for in a coarse scale cohesive zone model.

To this end, the temperature jump is defined as a vectorial quantity according to

$$[[\vec{\theta}]] = [[\theta]]\vec{m} \quad (2.1)$$

where $[[\theta]] = \theta^+ - \theta^-$ is the temperature difference between the two material points (depicted as + and -), which were sharing the same position prior to the appearance of the discontinuity and \vec{m} is the unit vector directed along the line connecting these two points as shown in figure 2.2. The temperature jump is intimately linked to the heat conduction taking place within the crack, both through the bridging solid parts and air filling the crack enclosure. In fact upon further loading, the crack bridging material gradually disappears and the effective conductance diminishes due to the loss of a heat conducting solid medium. The concept of thermal damage mechanics fits very well to quantify the reduction in effective conductivity, i.e. the heat flow conducted through the interface solid connections/links can be expressed as,

$$\vec{q}^s = -(1 - d)k_s[[\vec{\theta}]] \quad (2.2)$$

where d is the damage variable further discussed in section 3 and k_s is an effective thermal conductivity that is largely determined by the conductivity of the crack bridging structures, their fraction within the unit cohesive surface and their geometric layout. Since cohesive surfaces lack the third dimension (the thickness), k_s of equation (2.2), is in fact a heat conductance coefficient, quantifying the heat transported between the two surfaces that is proportional to the conductivity of the bridging solid fractions and inversely proportional with the thickness of the interface. Theoretically, perfectly conducting interfaces should have infinitely large k_s values but in a computational setting sufficiently large values should be adopted instead, see section 4.

At this stage, it is more appropriate to decompose the heat flux vector into a normal

and a tangential component as,

$$q_n^s = -(1-d)k_s [[\theta]] \vec{m} \cdot \vec{n} \quad (2.3a)$$

$$q_t^s = -(1-d)k_s [[\theta]] \vec{m} \cdot \vec{t} \quad (2.3b)$$

where \vec{n} and \vec{t} are unit normal and tangent vectors shown in figure 2.2. It is important to note that both components are representing the heat transported from one side to the other side of the cohesive crack. The proposed form for the interfacial heat conduction preserves the geometrical information which can be linked to the current geometry of material crack bridging structures in an average sense.

Heat conducted through air contributes to the normal component of the heat flux. Approximating the temperature difference in normal direction by $[[\theta]] \vec{m} \cdot \vec{n}$, heat conducted through air can be expressed as

$$q_n^g = -k_g [[\theta]] \vec{m} \cdot \vec{n} \quad (2.4)$$

Additionally, heat is transported also by radiation between the two faces of the crack, but this contribution is very small as reported in [25] and is not taken into account here. Therefore, the normal and tangential components of the interface heat flux can be written as

$$q_n = -((1-d)k_s + k_g) [[\theta]] \vec{m} \cdot \vec{n} \quad (2.5a)$$

$$q_t = -(1-d)k_s [[\theta]] \vec{m} \cdot \vec{t} \quad (2.5b)$$

where q_n and q_t are defined as heat fluxes in \vec{n} and \vec{t} direction, respectively. The magnitude of the interface heat flux which is the heat transported from one side of the crack to the other side is,

$$q_i = \sqrt{q_n^2 + q_t^2} \quad (2.6)$$

In case of load reversal, the crack tends to close but the real contact area is limited by the surface asperities. When the two crack surfaces touch, the real contact localizes at certain spots due to the surface roughness. Then the contact conductance is a combination of contact pressure dependent spot conductance and the conductance through the gas in the cavities formed in between the asperities, [25, 32]. Obviously, such a model requires detailed information about the crack surface characteristics. Since the contact conductance is mainly governed by the ratio of the actual contact area to the total interfacial area, the concept of a contact damage d_c can be used to handle crack closure. Assuming that, the contact tangential openings are not significant (in other words \vec{m} and \vec{t} are mutually perpendicular), the components of the interface heat flow vector are defined as

$$q_{n,c} = -((1-d_c)k_s) [[\theta]] \vec{m} \cdot \vec{n} \quad (2.7a)$$

$$q_{t,c} = 0 \quad (2.7b)$$

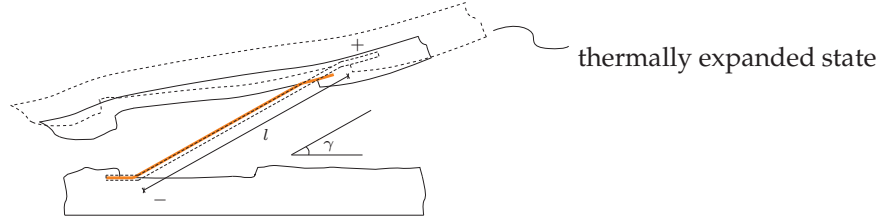


Figure 2.3: Free thermal expansion of a bridging fiber

Since the fraction of crack bridges are expected to be dominant in crack closure as well, one can assume that $d_c \approx d$, as long as full separation did not occur.

In figure 2.3, an idealized situation, with a cohesive crack and a bridging fiber is shown. It is assumed that the fiber is free to expand or contract without any mechanical constraints and a temperature difference is applied to the system leading to the deformed configuration as shown in figure 2.3. Due to thermal expansion and temperature difference, the fiber elongates or shortens, which results in an increment/decrement in the normal and tangential openings. Since fibers or other crack bridging structures are not explicitly resolved in a cohesive zone approximation of the interface, a correction needs to be made to account for the interfacial opening as a result of thermal expansion effects in the (constrained) interface. To this purpose, ‘temperature jump openings’ are introduced, discriminating the openings due to mechanical and thermal loading. Focusing on the deformed geometry and assuming a linear temperature profile along the fiber, when the temperature of the positive side is increased by $[[\theta]]$, one can write for a single fiber:

$$0.5\alpha[[\theta]]l\sin\gamma = \Delta_n^T \quad (2.8a)$$

$$0.5\alpha[[\theta]]l\cos\gamma = \Delta_t^T \quad (2.8b)$$

where α is the coefficient of thermal expansion (CTE) of the fiber, $[[\theta]]$ is the temperature difference, γ is the angle shown in figure, and Δ_n^T and Δ_t^T are normal and tangential openings due to the temperature jump, respectively.

For the cohesive zone description, $l\sin\gamma$ and $l\cos\gamma$ correspond to the current normal and tangential openings, respectively. Since the previous analysis is based on a single fiber only, the CTE of the fiber should be replaced by a more representative value, since the collective response of many crack bridging agents, their geometric arrangement and volumetric fraction influences the openings due to the temperature jump. Therefore in a more general format, equation (2.8a) and (2.8b), are reformulated as

$$\Delta_n^T = \alpha_{\text{int}}[[\theta]]\Delta_n \quad (2.9a)$$

$$\Delta_t^T = \alpha_{\text{int}}[[\theta]]\Delta_t \quad (2.9b)$$

where α_{int} is the CTE of the interface, Δ_n and Δ_t are the current normal and tangential openings, respectively. In [26], the openings due to the temperature jump appear

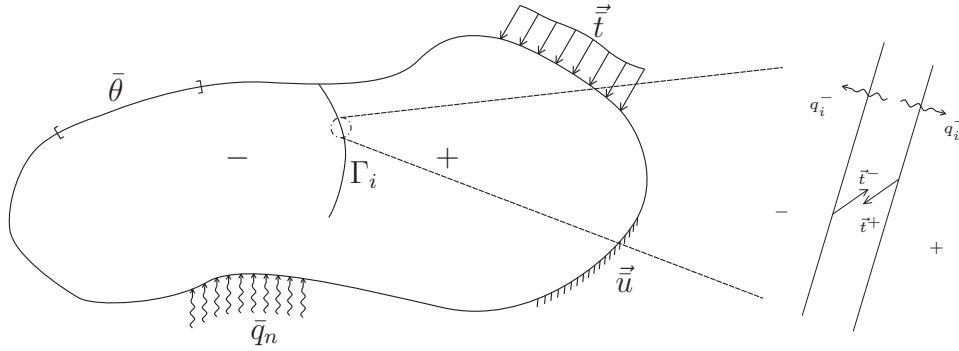


Figure 2.4: Solid body partially separated by a cohesive crack and interface continuity conditions

naturally as a result of the general interfacial free energy expression.

In the following section, the thermo-mechanics of a solid separated by an interface is elaborated both in strong and weak form. Thereafter, the presented concepts are recast in a discretized format suitable for application within a finite element framework.

2.3 Thermo-mechanics

In figure 2.4, a body partially separated by a cohesive crack across the internal boundary Γ_i is shown. In a geometrically nonlinear setting, the mechanical equilibrium in terms of the Cauchy stress tensor σ is written as,

$$\vec{\nabla} \cdot \sigma + \vec{b} = \vec{0} \quad (2.10)$$

where $\vec{\nabla}$ is the gradient with respect to the current configuration and \vec{b} is the body force vector. At the cohesive crack, the traction continuity condition,

$$\vec{t}^+ = -\vec{t}^- \quad (2.11)$$

has to be satisfied where the superscripts $^+$ & $^-$ indicate approaching to the interface from $+$ and $-$ sides (see figure 2.4) respectively.

In the absence of internal heat sources, the thermal equilibrium in current configuration is expressed as,

$$\rho c_v \dot{\theta} + \vec{\nabla} \cdot \vec{q} = 0 \quad (2.12)$$

where ρ is the density and c_v is the heat capacity of the material. Furthermore, taking the inflowing heat as positive, the heat flux vector \vec{q} has to satisfy the continuity

condition

$$q_i^+ = -q_i^- \quad (2.13)$$

everywhere along the cohesive crack. By applying the Galerkin procedure, the weak forms of the balance equations are obtained as,

$$\int_V \sigma : \vec{\nabla} \delta \vec{u} dV = \int_V \vec{b} \cdot \delta \vec{u} dV + \int_{\Gamma_t} \vec{t} \cdot \delta \vec{u} d\Gamma + \int_{\Gamma_i^+} \vec{t}^+ \cdot \delta \vec{u}^+ d\Gamma + \int_{\Gamma_i^-} \vec{t}^- \cdot \delta \vec{u}^- d\Gamma \quad (2.14a)$$

$$\int_V \rho c_v \dot{\theta} \delta \theta dV + \int_V \vec{q} \cdot \vec{\nabla} \delta \theta dV = \int_{\Gamma_q} \bar{q} \delta \theta d\Gamma + \int_{\Gamma_i^+} q_i^+ \delta \theta^+ d\Gamma + \int_{\Gamma_i^-} q_i^- \delta \theta^- d\Gamma \quad (2.14b)$$

which can be (by using equation 2.11 and 2.13) expressed as

$$\int_V \sigma : \vec{\nabla} \delta \vec{u} dV = \int_V \vec{b} \cdot \delta \vec{u} dV + \int_{\Gamma_t} \vec{t} \cdot \delta \vec{u} d\Gamma + \int_{\Gamma_i^+} \vec{t}^+ \cdot (\delta \vec{u}^+ - \delta \vec{u}^-) d\Gamma \quad (2.15a)$$

$$\int_V \rho c_v \dot{\theta} \delta \theta dV + \int_V \vec{q} \cdot \vec{\nabla} \delta \theta dV = \int_{\Gamma_q} \bar{q} \delta \theta d\Gamma + \int_{\Gamma_i^+} q_i^+ (\delta \theta^+ - \delta \theta^-) d\Gamma \quad (2.15b)$$

Here, $\Gamma_{\vec{t}}$ and $\Gamma_{\vec{q}}$ are the parts of the boundaries where the prescribed traction (\vec{t}) and prescribed normal heat fluxes (\bar{q}) are applied. The boundary integrals over Γ_i^+ in equation 2.15a and 2.15b are the non-standard extra terms due to the cohesive crack, detailed further hereafter.

Considering a discretization by 2-noded elements for a 2-D problem as shown in figure 2.5, the surface integral over Γ_i in equation (2.15a) is converted into the form,

$$\int_{\Gamma_i^+} \vec{t}^+ \cdot (\delta \vec{u}^+ - \delta \vec{u}^-) d\Gamma = \sum_{k=1}^{n_{el}} \int_{\Gamma_e^k} \underline{t} \delta \underline{\Delta} d\Gamma \quad (2.16)$$

where n_{el} is the number of interface elements in the discretization, $\underline{t} = [t_n \ t_t]$ and $\delta \underline{\Delta} = [\delta \Delta_n \ \delta \Delta_t]^T$. As shown in figure 2.5, Δ_n and Δ_t are defined with respect to the local coordinate system defined on the mid-plane of the interface element. t_n and t_t are the normal and tangential components of \vec{t}^+ with respect to the same local coordinate system. The determination of t_n and t_t requires constitutive relations in terms of openings, for which the improved Xu-Needleman law [33],

$$t_n = \frac{\phi_n}{\delta_n} \left(\frac{\Delta_{n,m}}{\delta_n} \right) \exp\left(-\frac{\Delta_{n,m}}{\delta_n}\right) \exp\left(-\frac{\Delta_{t,m}^2}{\delta_t^2}\right) \quad (2.17a)$$

$$t_t = 2 \frac{\phi_t}{\delta_t} \left(\frac{\Delta_{t,m}}{\delta_t} \right) \left(1 + \frac{\Delta_{n,m}}{\delta_n} \right) \exp\left(-\frac{\Delta_{t,m}^2}{\delta_t^2}\right) \exp\left(-\frac{\Delta_{n,m}}{\delta_n}\right) \quad (2.17b)$$

is adopted with the proper replacements $\Delta_{n,m}$ and $\Delta_{t,m}$ which are defined as

$$\Delta_{n,m} = \Delta_n - \Delta_n^T \quad (2.18a)$$

$$\Delta_{t,m} = \Delta_t - \Delta_t^T \quad (2.18b)$$

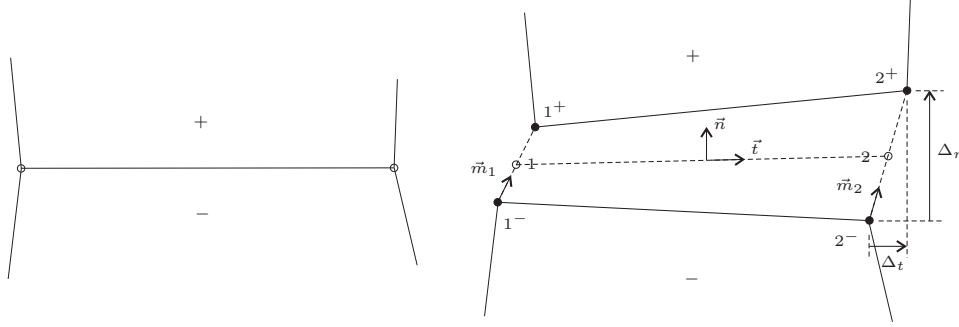


Figure 2.5: Two noded interface element, unreformed and deformed configurations

Typical traction-opening relations, with an unloading-reloading cycle are shown in figure 2.6. The irreversible behaviour is based on a single history parameter Δ_{max} , representing the maximum effective opening reached during the loading history whereby the effective opening is defined as

$$\Delta_{eff} = \sqrt{\beta^2 \Delta_t^2 + \Delta_n^2} \quad (2.19)$$

where β is a scaling parameter and taken as 0.5 in this work. Loading takes place when $\Delta_{eff} = \Delta_{max}$ and $\dot{\Delta}_{eff} \geq 0$ and unloading (or reloading) when $\Delta_{eff} < \Delta_{max}$. The traction expressions in case of unloading and the corresponding material tangents are given in the appendix 2.6.

The damage parameter d introduced in equation (2.2), is defined as the ratio of $\frac{\Delta_{max}}{\Delta_{cr}}$ with the critical effective opening,

$$\Delta_{cr} = \sqrt{\beta^2 \Delta_{t,cr}^2 + \Delta_{n,cr}^2} \quad (2.20)$$

where $\Delta_{t,cr}$ and $\Delta_{n,cr}$ are the tangential and normal openings corresponding to small traction values (in this work $0.1t_t^{max}$ and $0.1t_n^{max}$) in the post-peak regime of the traction opening curves, respectively. It is ensured that, $d \leq 1.0$ in case of excessive openings. The interface integral of equation (2.15b) is expressed as

$$\int_{\Gamma_i} q_i (\delta\theta^+ - \delta\theta^-) d\Gamma = \sum_{k=1}^{n_{el}} \int_{\Gamma_e^k} q_i \delta[\theta] d\Gamma \quad (2.21)$$

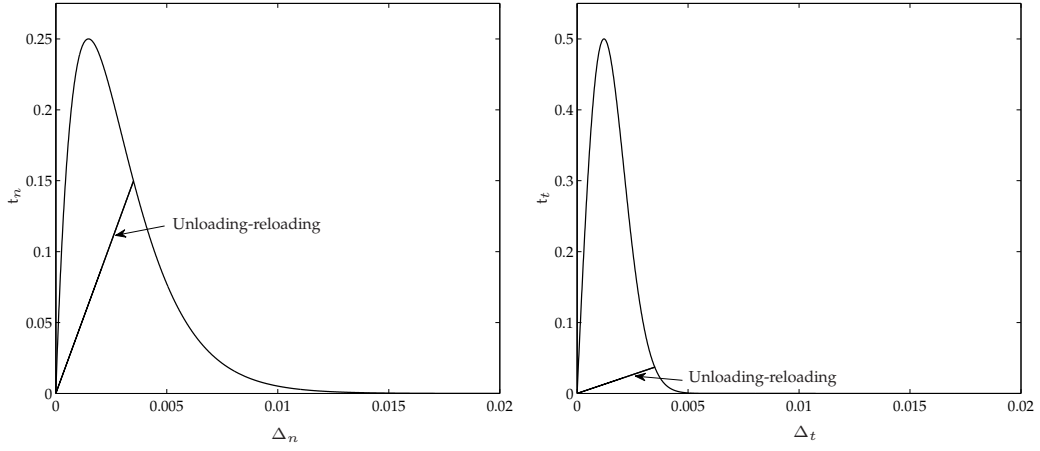


Figure 2.6: Left: normal traction-opening relation; Right: tangential traction-opening relation

In a discrete setting, the temperature jump vector introduced in equation (2.1), is expressed as

$$\begin{aligned} \vec{[\theta]} &= N_1 (\theta_{1+} - \theta_{1-}) \vec{m}_1 + N_2 (\theta_{2+} - \theta_{2-}) \vec{m}_2 \\ \text{with } \vec{m}_1 &= \frac{\vec{x}_{1+} - \vec{x}_{1-}}{\|\vec{x}_{1+} - \vec{x}_{1-}\|} \text{ and } \vec{m}_2 = \frac{\vec{x}_{2+} - \vec{x}_{2-}}{\|\vec{x}_{2+} - \vec{x}_{2-}\|} \end{aligned} \quad (2.22)$$

where N_1 and N_2 are the standard 1-D shape functions. With this approximation, at a particular integration point p , the normal and tangential components of the interface heat flux vector can be evaluated as

$$q_n = ((1.0 - d)k_s + k_g)[\vec{\theta}]|_p \cdot \vec{n} \quad (2.23a)$$

$$q_t = (1.0 - d)k_s[\vec{\theta}]|_p \cdot \vec{t} \quad (2.23b)$$

On the basis of equations (2.6) and (2.23), the interface heat flux is determined.

The presented element is implemented in a commercial FE software environment and the coupled thermo-mechanical analysis is carried out with a staggered solution scheme. In each load increment, two uncoupled sub-problems, namely the thermal and mechanical equilibrium are solved by the Newton-Raphson method, sequentially. The material tangent operators of the interface elements are presented in the appendix 2.6.

2.4 Thermo-mechanical Analysis of a Granular Microstructure

Due to their high temperature resistance, technical ceramics are used as the base material for specific structural parts and in some cases they are used as coating layers to protect vulnerable components from adverse effects of severe temperature changes. They have a granular microstructure with typical grain dimensions in the micron range or larger. An idealized example case focusing on the thermo-mechanical analysis of such a microstructure is presented in order to investigate the influence of thermo-mechanical cohesive zone description on the evolution of the thermal fields.

A small sub-domain of a coating layer, with the geometry and granular microstructure shown on the right-hand side of figure 2.7, is extracted in order to conduct the thermo-mechanical analysis. The microstructure is composed of single crystal alumina grains with a tetragonal crystal structure. The corresponding anisotropic mechanical constants are taken to be $c_{11} = 465$ GPa, $c_{22} = 465$ GPa, $c_{33} = 563$ GPa, $c_{12} = 124$ GPa, $c_{13} = 117$ GPa, $c_{44} = 233$ GPa and the conductivities in the principal directions are given as 38 W/mK and 10 W/mK [34]. The heat capacity and density values are $c_v = 1200$ J/kgK, $\rho = 2700$ kg/m³ and the principal values of the anisotropic thermal expansion coefficients are $7.9 \cdot 10^{-6}$ 1/K and $8.8 \cdot 10^{-6}$ 1/K. The orientation of the principal axis within each alumina grain is taken to be random and the difference between the neighbouring grains are large enough to exclude the presence of a certain texture within the microstructure. The top boundary is exposed to a ramp type prescribed temperature boundary condition which reaches the peak temperature of 1000 °C within 4 seconds and which is kept constant until the end of the loading duration of 10 s. The bottom surface is kept at 20 °C throughout the analysis. Mechanically, periodic boundary conditions are applied on the left and right boundaries as shown in the figure. Plane strain conditions are assumed and the thermo-mechanical cohesive zone elements are placed along the grain boundaries.

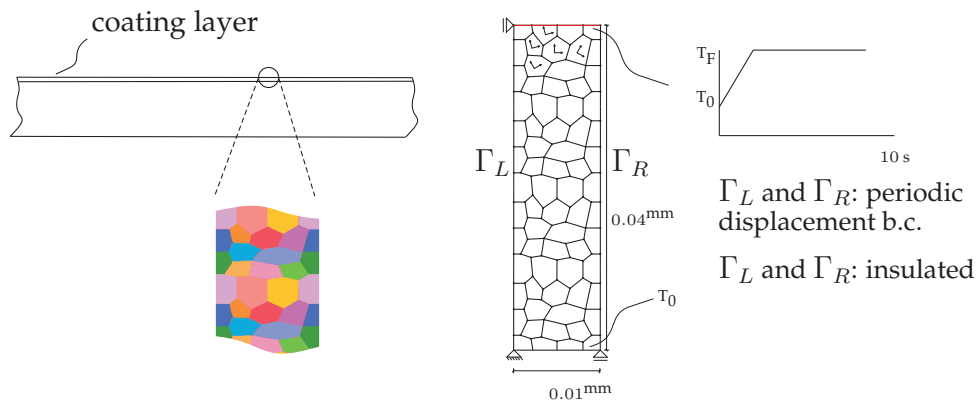


Figure 2.7: Thermo-mechanical analysis of a granular microstructure; geometry and boundary conditions

The k_s value for the interfaces is determined on the basis of the conductivity values for the bulk material and the characteristic openings for the interfaces calculated from the energies and maximum traction values. Furthermore, in case of mechanically intact interfaces, the influence of k_s on the resulting temperature profile should be very small which can be monitored on the basis of temperature jumps across the interfaces. As the k_s value is taken larger, the temperature jump diminishes and in the limit of infinitely large k_s , the temperature jump becomes zero. Therefore some preliminary analysis is carried out to determine the k_s values resulting in $k_s = 5 \cdot 10^3$ W/mm. It is also observed that the influences of Δ_n^T and Δ_t^T are negligibly small therefore interface thermal expansion, α_{int} , is taken to be zero. Keeping the values of $\phi_n = 40$ J/m² and $\phi_t = 80$ J/m² the same, two different analyses are carried out with $t_n^{\max} = 100$ MPa, $t_t^{\max} = 200$ MPa and $t_n^{\max} = 800$ MPa, $t_t^{\max} = 1600$ MPa, respectively.

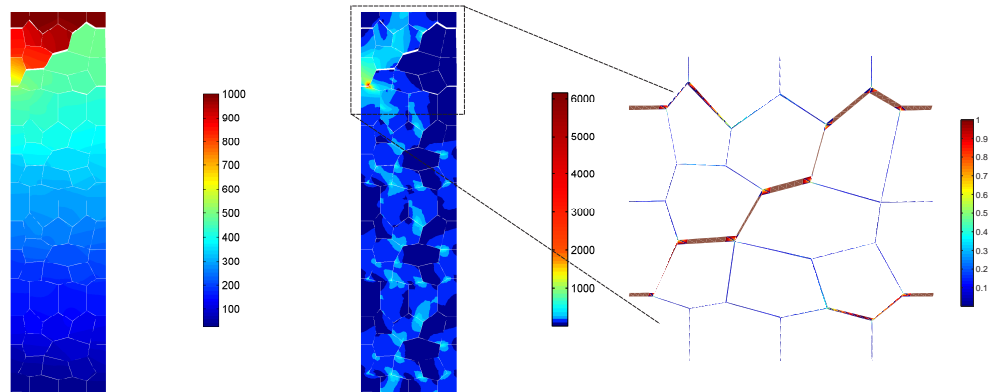


Figure 2.8: From left to right: Temperature (°C), magnitude of heat flux (W/mm²), interface damage for ductile interface; $t_n^{\max} = 100$ MPa, $t_t^{\max} = 200$ MPa

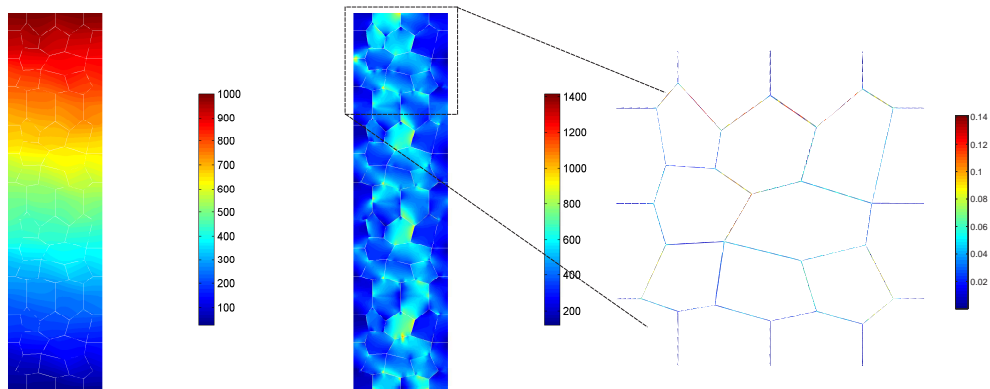


Figure 2.9: From left to right: Temperature (°C), magnitude of heat flux (W/mm²), interface damage for brittle interface; $t_n^{\max} = 800$ MPa, $t_t^{\max} = 1600$ MPa

These values are comparable with the values given in [12] which focuses on the response of fine grained alumina samples under dynamic mechanical loading. Obviously the former case leads to a more ductile interface response since smaller maximum traction values are used with the same energies.

In figure 2.8 and 2.9, the resulting temperature profiles, magnitude of the heat flux vectors along with the interfacial damage distribution are shown for both cases. As a matter of fact, as the interfacial damage increases, the heat flow through the interface becomes more difficult. Therefore one expects some sharp temperature discontinuities as suggested by the more ductile case which has more severe interface damage. Furthermore, the correlation between the damage and the magnitude of the heat flux distribution suggests that as the crack further opens up, heat flow is redirected to more conductive regions. A comparison of heat flow patterns for the two cases clearly shows this effect, as the heat follows the intact path in case of more severe interface damage. Furthermore, as shown in figure 2.10, in case of strong interface damage, the temperature jumps along the interfaces could reach very significant levels, which in turn will influence the local mechanical response as well which is hardly applicable here as no mechanical load is imposed.

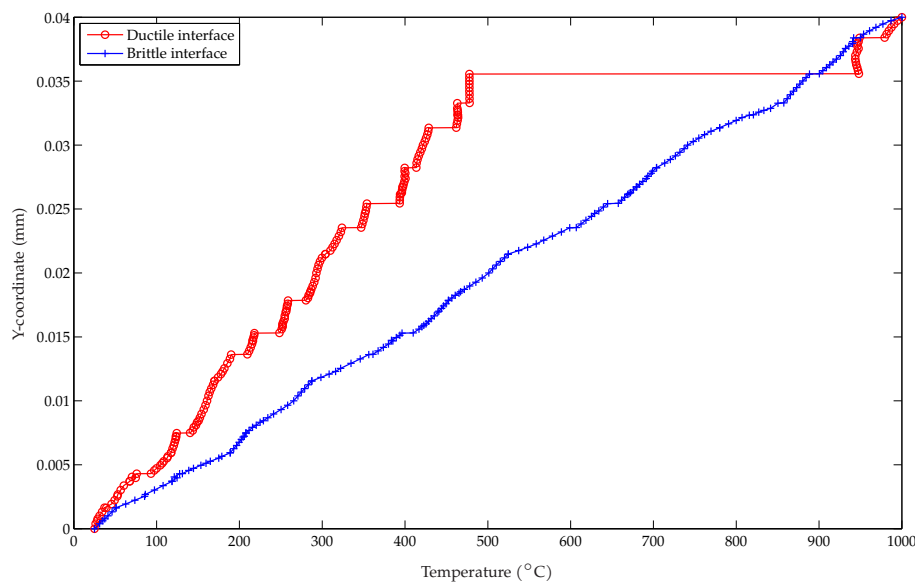


Figure 2.10: Temperature profile along the mid-section

2.5 Conclusion and Outlook

Motivated by the thermal shock analysis of heterogenous materials, a thermo-mechanical cohesive zone description is presented which is suitable for the analysis

of material interfaces at different scales, ranging from grain boundaries to multiply structural components. The physical heat transport mechanisms are taken into account within the limitations of a macroscopic cohesive zone formulation. As shown by the example problem, the evolution of mechanical damage might influence the thermal field quantities both qualitatively and quantitatively. As the heat conduction characteristics evolve due to interfacial damage, the heat flow pattern and local stress state might change significantly. Therefore, the proposed formulation assists in acquiring a better understanding of the failure initiation and propagation under severe thermal loading conditions. Furthermore, the efficiency of protective layers in terms of thermal performance can be investigated in a better way and can be optimized. Temperature dependency of the interface parameters, e.g. fracture energies, can be incorporated in the formulation easily provided that these dependencies are known. In conclusion, the thermo-mechanical analysis of material interfaces can be done in an effective way using the proposed formulation.

2.6 Appendix

The solution of the mechanical and thermal equilibrium equations are conducted within an incremental-iterative framework by means of the Newton-Raphson method. Since the problem is solved by an operator-split technique, incrementally the mechanical and thermal equilibrium equations are solved in an uncoupled way. The material tangent relations of the traction-opening relations, which are necessary for the consistent linearization of the mechanical equilibrium equations are given first.

In case of loading, the derivatives

$$\frac{\partial t_n}{\partial \Delta_{n,m}} = \frac{\phi_n}{\delta_n} \exp\left(-\frac{\Delta_{n,m}}{\delta_n}\right) \left(\frac{1}{\delta_n} - \frac{\Delta_{n,m}}{\delta_n^2}\right) \exp\left(-\frac{\Delta_{t,m}^2}{\delta_t^2}\right) \quad (2.24a)$$

$$\frac{\partial t_n}{\partial \Delta_{t,m}} = \frac{\phi_n}{\delta_n} \exp\left(-\frac{\Delta_{n,m}}{\delta_n}\right) \left(-2\frac{\Delta_{n,m}}{\delta_n} \frac{\Delta_{t,m}}{\delta_t^2} \exp\left(-\frac{\Delta_{t,m}^2}{\delta_t^2}\right)\right) \quad (2.24b)$$

$$\frac{\partial t_t}{\partial \Delta_{t,m}} = \left(1 + \frac{\Delta_{n,m}}{\delta_n}\right) \exp\left(-\frac{\Delta_{n,m}}{\delta_n}\right) \exp\left(-\frac{\Delta_{t,m}^2}{\delta_t^2}\right) 2\frac{\phi_t}{\delta_t^2} \left(1 - 2\frac{\Delta_{t,m}^2}{\delta_t^2}\right) \quad (2.24c)$$

$$\frac{\partial t_t}{\partial \Delta_{n,m}} = \frac{\phi_t}{\delta_n} \left(\frac{\Delta_{n,m}}{\delta_n}\right) \left(-2\frac{\Delta_{t,m}}{\delta_t^2}\right) \exp\left(-\frac{\Delta_{n,m}}{\delta_n}\right) \exp\left(-\frac{\Delta_{t,m}^2}{\delta_t^2}\right) \quad (2.24d)$$

are used to construct the material tangent operator. In case of unloading and reloading, there might be discontinuities in the traction-opening relations whenever the reloading direction differs from the unloading direction, see [35]. To prevent such

artificial jumps, the tractions are defined as:

$$t_n^{unl} = \frac{\Delta_{eff}}{\Delta_{max}} t_n (\Delta_{n,m}^*, \Delta_{t,m}^*) \quad (2.25a)$$

$$t_t^{unl} = \frac{\Delta_{eff}}{\Delta_{max}} t_t (\Delta_{n,m}^*, \Delta_{t,m}^*) \quad (2.25b)$$

$$(2.25c)$$

where

$$\Delta_{n,m}^* = \frac{\Delta_{max}}{\Delta_{eff}} \Delta_n \quad (2.26a)$$

$$\Delta_{t,m}^* = \frac{\Delta_{max}}{\Delta_{eff}} \Delta_t \quad (2.26b)$$

and Δ_{max} is the maximum effective opening reached during the history and Δ_{eff} is the current effective opening, both based on mechanical openings. The corresponding derivatives are:

$$\frac{\partial t_n}{\partial \Delta_{n,m}} = \frac{\partial t_n}{\partial \Delta_{n,m}^*} + \frac{\Delta_{n,m}}{\Delta_{max} \Delta_{eff}} t_n - \frac{\Delta_{n,m}^2}{\Delta_{eff}^2} \frac{\partial t_n}{\partial \Delta_{n,m}^*} - \frac{\Delta_{n,m} \Delta_{t,m}}{\Delta_{eff}^2} \frac{\partial t_n}{\partial \Delta_{t,m}^*} \quad (2.27a)$$

$$\frac{\partial t_n}{\partial \Delta_{t,m}} = \frac{\partial t_n}{\partial \Delta_{t,m}^*} + \beta^2 \frac{\Delta_{t,m}}{\Delta_{max} \Delta_{eff}} t_n - \beta^2 \frac{\Delta_{t,m}^2}{\Delta_{eff}^2} \frac{\partial t_n}{\partial \Delta_{t,m}^*} - \beta^2 \frac{\Delta_{n,m} \Delta_{t,m}}{\Delta_{eff}^2} \frac{\partial t_n}{\partial \Delta_{n,m}^*} \quad (2.27b)$$

$$\frac{\partial t_t}{\partial \Delta_{t,m}} = \frac{\partial t_t}{\partial \Delta_{t,m}^*} + \beta^2 \frac{\Delta_{t,m}}{\Delta_{max} \Delta_{eff}} t_t - \beta^2 \frac{\Delta_{t,m}^2}{\Delta_{eff}^2} \frac{\partial t_t}{\partial \Delta_{t,m}^*} - \beta^2 \frac{\Delta_{n,m} \Delta_{t,m}}{\Delta_{eff}^2} \frac{\partial t_t}{\partial \Delta_{n,m}^*} \quad (2.27c)$$

$$\frac{\partial t_t}{\partial \Delta_{n,m}} = \frac{\partial t_t}{\partial \Delta_{n,m}^*} + \frac{\Delta_{n,m}}{\Delta_{max} \Delta_{eff}} t_t - \frac{\Delta_{n,m}^2}{\Delta_{eff}^2} \frac{\partial t_t}{\partial \Delta_{n,m}^*} - \frac{\Delta_{n,m} \Delta_{t,m}}{\Delta_{eff}^2} \frac{\partial t_t}{\partial \Delta_{t,m}^*} \quad (2.27d)$$

The expression for $\frac{\partial t_t}{\partial \Delta_{t,m}^*}$ and the other comparable terms are identical to the corresponding expressions given above provided that, for example $\Delta_{t,m}$ and $\Delta_{n,m}$ are replaced by $\Delta_{t,m}^*$ and $\Delta_{n,m}^*$.

The linearization of the thermal equilibrium requires the sensitivity of the interface heat flux with respect to temperature jump. In case loading and unloading, the derivative,

$$\frac{\partial q_i}{\partial \Delta \theta} = \frac{1}{2} \frac{1}{\sqrt{q_n^2 + q_t^2}} (2q_n((1-d)k_s + k_g) \vec{m} \cdot \vec{n} + 2q_t(1-d)k_s \vec{m} \cdot \vec{t}) \quad (2.28)$$

is used in the solution of the linearized thermal equilibrium equations. In case of contact, the derivative takes the following form,

$$\frac{\partial q_i}{\partial \Delta \theta} = \frac{1}{2} \frac{1}{q_n} (2q_n((1-d_c)k_s) \vec{m} \cdot \vec{n}) \quad (2.29)$$

CHAPTER THREE

Modelling Thermal Shock Damage in Refractory Materials via Direct Numerical Simulation (DNS)¹

Abstract

In this chapter, a computational investigation on thermo-mechanically induced damage in refractory materials resulting from severe thermal shock conditions is presented. On the basis of an idealized two-phase material system, molten aluminium thermal shock tests [36] are computationally modeled by means of direct numerical simulations (DNS). The interfacial and bulk damage evolution within the material are described by thermo-mechanical cohesive zones and continuum damage mechanics (CDM), respectively. Reported experimental results [36] are used to identify the parameters of the model. Furthermore, a parametric study is carried out to investigate the relative significance of various microstructure parameters in the context of thermal shock response.

¹*Based on: I. Özdemir, W.A.M. Brekelmans, M.G.D. Geers. Modelling Thermal Shock Damage in Refractory Materials via Direct Numerical Simulation. to be submitted.*

3.1 Introduction

In metal production plants, molten metal is transported and processed by means of structures made of high temperature resistant (refractory) materials. Under operation conditions, these structures are exposed to rapid temperature changes (thermal shock) and temperature change cycles, mainly due to contact with molten metal. Refractories with a high Alumina (Al_2O_3) content and relatively large grained ceramics are used for the production of such structures. Making use of raw base materials in the production of these ceramics, the resulting microstructures are far from homogeneous.

When a heterogeneous material system experiences a temperature change, a stress field develops depending on the boundary conditions, the coefficient of thermal expansion (CTE) mismatch between the phases and the uniformity/non-uniformity of the temperature change within the domain of interest. To illustrate the essential mechanisms of the internal stress development, a representative two-phase material system of isotropic phases (both mechanically and thermally) is considered as shown in figure 3.1. In case of identical CTE's, a uniform temperature change within the body in combination with the given boundary conditions would lead to a stress free expansion or contraction. If a difference between the CTE's exists, under the same loading and boundary conditions, a self-equilibrated internal stress profile develops due to the mechanical strains resulting from non-uniform thermal expansion/contraction. Similarly, a non-uniform temperature change, e.g. occurrence of a temperature gradient, under certain external constraints, leads to internal stresses even in the case of matching CTE's. Therefore for common engineering materials and loading conditions, there are two mechanisms which lead to internal stresses. The first mechanism is associated with the CTE mismatch of the phases and the second mechanism is related to gradients in the resulting temperature profile which lead to non-uniform expansion or contraction. In this simple reasoning, it is implicitly assumed that the interface remains mechanically intact and acts as a perfect heat conductor. However, in real material systems, in general, the interfaces degrade mechanically after a certain threshold and consequently lose their ability to transmit stresses and to act as a perfect conductor. Therefore, when the thermal loading conditions reach significant levels, the initiation and propagation of material failure is dictated by the collective behavior of the interfaces, individual phases, and the contrast in their mechanical and thermo-physical properties and fracture characteristics. For example, the average grain size dependency of residual strength observed in quenching tests on fine grained technical ceramics [4, 37, 38], illustrates the microstructure-property relation under thermal shock conditions. The micromechanical origin of cracking in fine grained material systems upon temperature change has been investigated by relatively simple micromechanical models (semi-) analytically in [7, 9, 10]. The characteristics of the solutions, e.g. stress singularities, were particularly useful to understand the significant role of grain size and to identify the potential sites of crack nucleation. Computational models have been used to investigate more complex geometries and different boundary conditions at the micro level often relying on

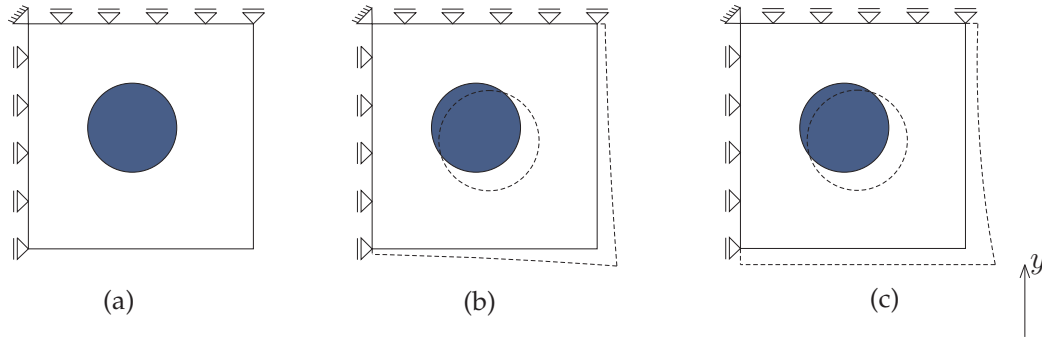


Figure 3.1: Two-phase material system with different CTE's, (a) initial configuration (b) Uniform temperature change, (c) Temperature gradient in y direction (dashed lines correspond to the deformed shape)

the concept of a representative volume elements (RVE) and extracting macroscopic elastic properties, [39].

Approaching the problem from the macro scale, to enhance the understanding and modeling of thermo-mechanically induced damage, such as failure of refractory linings [40] and concrete failure under high temperatures [41, 42], predictive computational tools within the framework of continuum damage mechanics, have been developed. In such approaches, the heterogeneous microstructure is replaced by an equivalent 'homogeneous' material, which inevitably implies the loss of information associated with the heterogeneous nature of the microstructure. In some of these models, the local mechanisms, e.g. stresses due to a CTE mismatch, are smeared out by some extra terms in damage evolution laws in a phenomenological way, see [43]. These approaches are computationally feasible tools for damage analysis of engineering structures but rather limited for the investigation of fundamental mechanisms determining the behaviour at the level of the microstructure.

Multi-scale computational models incorporating fine-scale physical mechanisms in their coarse-scale constitutive response are an accurate and feasible alternative for the analysis of engineering structures, see [44]. However, the capabilities of such models heavily depend on the proper characterization of micro scale material parameters. Direct measurement of physical properties at the scale of individual phases and interfaces, e.g. strength of an interface, is still a challenging task for experimentalists. Therefore, direct numerical simulations (DNS) within an inverse analysis framework constitute an alternative to determine these parameters, at least the correct order of magnitude, which can be a reliable data base for a multi-scale model.

To investigate the influence of microstructural parameters and to improve the understanding of material response under thermal loading conditions, thermal shock experiments are reproduced in a computational setting through fully resolved Direct Numerical Simulation (DNS) models.

In the next section, the composition of the material microstructure is presented. Then, the experimental characterization and conducted experiments are summa-

Chemical Composition (Relative weight of components)		Volumetric Composition (Volume percentages)	
Al ₂ O ₃	90.9 %	Alumina	59 %
SiO ₂	8.8 %	Mullite	41 %
Na ₂ O	0.2 %		

Table 3.1: Initial chemical composition and final volume fractions

ized. Thereafter, the construction of the DNS model, the constitutive modeling of each phase and the solution procedure are outlined. Parameters of the model are determined on the basis of an equivalent static procedure, which is detailed in section 3.4.5. Then, the focus is shifted on the influence of different material parameters, which is particularly relevant for the industry that processes these refractories. The chapter is closed by the summary and conclusions.

3.2 Material Microstructure

The initial chemical composition of the considered batch with a certain grading of particles is given in table 3.1. The mixture is first mechanically pressed in a mould, resulting in a 'green product' and then sintered at 1900 °C - 2000 °C to achieve a certain coherence and strength. During the sintering process (phase), fine SiO₂ (approximately 0.2 μm) and Al₂O₃ particles react and result in a composite of mullite (3Al₂O₃2SiO₂) which is by weight 71.8 % Al₂O₃ and 28.2 % SiO₂. Accordingly, the resulting product consists of 35.5 % Mullite with a very fine microstructure and 64.5 % Al₂O₃ of various particle sizes. However, the reaction of SiO₂ and Al₂O₃ is never fully complete and additionally an amorphous glass phase is formed consisting mainly of Al₂O₃, SiO₂ and impurities. In the following sections, the presence of this glass phase is neglected. Based on the measurements given in [45], the difference between the theoretical and measured density reveals that there exists a porosity of approximately 14 %. Furthermore, it can be safely assumed that relatively large Al₂O₃ particles (particles of 3 mm and 0.875 mm respectively) are free of any porosity. Representative images of the resulting microstructure is given in figure 3.2.

3.3 Experimental Characterization of Thermal Shock Response

Experimental investigations dealing with the thermal shock response of refractory materials are extensively reported in the literature, see [36] and the references cited therein. Typically, down-quenching experiments have been conducted by using different quenching mediums ranging from water to molten salt. For up-quenching,

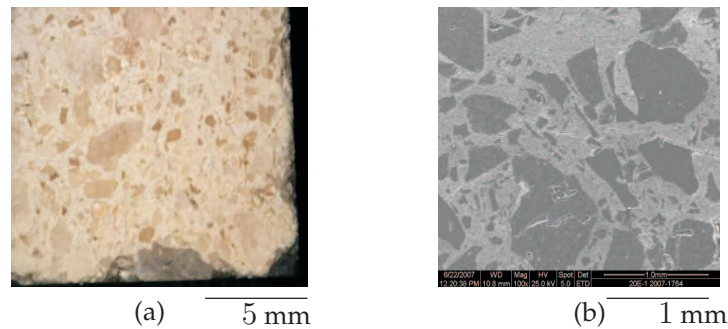


Figure 3.2: Microstructure of the material, (a) light microscope image (b) TEM image

burners, molten metals and other techniques and devices have been utilized. Due to difficulties associated with the determination of the heat transfer conditions, these methods are not really suitable to adequately quantify the thermal shock response of different material systems.

Motivated by the shortcomings of the existing methods, mainly in realizing reproducible heat transfer conditions, in [36] refractory specimens were subjected repeatedly to surface contact with molten aluminium followed by passively cooling of the samples in ambient air. By measuring the transit time of longitudinal ultrasonic waves at various locations on the samples, the local damage is characterized in terms of reduction in the dynamic Young's modulus. The use of transit time measurement techniques to determine the damage in refractory materials with coarse grains is validated by independent experiments, see [36]. The test set-up, the so-called 'molten aluminium thermal shock test' is schematically shown in figure 3.3. An equivalent computational testing procedure is developed starting with a DNS model of the experiment as presented in the next section.

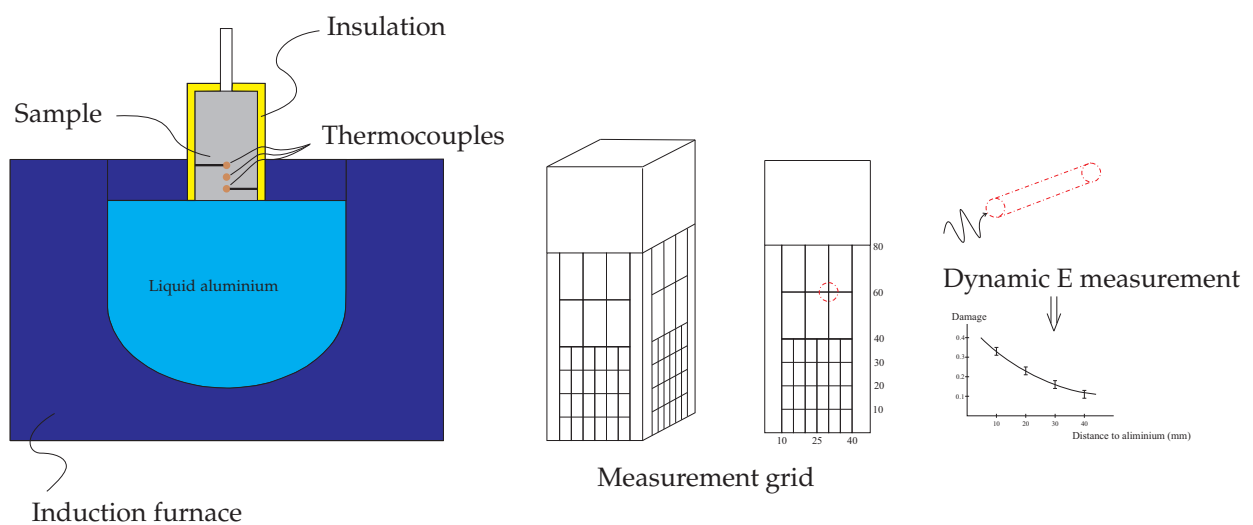


Figure 3.3: Molten aluminium thermal shock test set-up

3.4 Direct Numerical Simulation (DNS) of Thermal Shock Experiments

As shown in figure 3.2, the resulting microstructure is composed of two distinguishable phases at a mm scale. Relatively large grains are identifiable, which can be assumed to be embedded in a compound of fine grains that constitute a rather monolithic continuous phase, i.e. the matrix. Therefore the microstructure is idealized as a two phase composite with large, non-interacting grains of two different sizes (3 mm and 0.875 mm respectively), embedded in a matrix of Al_2O_3 and mullite which is in fact the sintered, continuous structure of grains smaller than $0.5\mu m$. Therefore, grains, matrix and their interfaces are the three distinct components which collectively determine the response of the material and have to be addressed in the computational model.

Due to unaffordable computational costs of a 3-D model, a fully detailed 2-D model of the test sample is constructed as shown in figure 3.4. To this end, volume fractions and basic geometrical information is used to construct, geometrically and physically representative volumetric units of the material. To achieve a geometric randomness in the distribution of the particles, four geometrically different unit volumes and their arbitrarily rotated versions are combined to built-up the full DNS model.

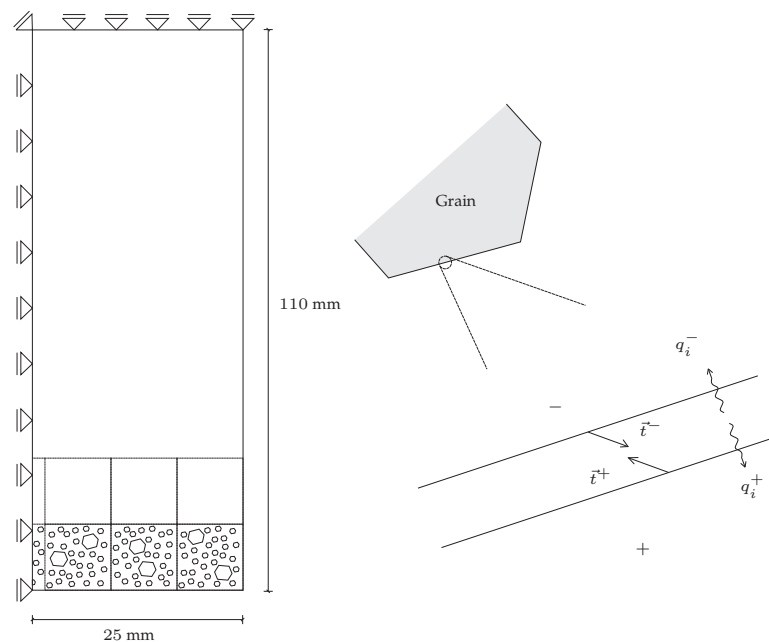


Figure 3.4: Direct numerical simulation model and traction and heat flux conditions across a grain-matrix interface

The sample is brought into contact with the molten aluminium reservoir (which is at $1000\text{ }^\circ\text{C}$) for 20 minutes ('thermal shock phase'). This is followed by a passive

‘cooling phase’ of 48 hours at room temperature (25 °C). The heat transfer characteristics between the sample and the reservoir are identified in [46] and resulted in temperature dependent heat transfer coefficient according to

$$h = 204.56 + e^{0.0082\theta_f} [\text{W}/\text{m}^2 \text{K}] \quad (3.1)$$

where θ_f is the film temperature defined as $\theta_f = 0.5(\theta_{\text{ambient}} + \theta_{\text{surface}})$. The same study revealed that the heat loss from the sample during passive cooling takes place at a very slow rate compared to the thermal shock phase and therefore this stage is not really relevant as far as damage initiation and evolution is concerned. Half of the sample is modeled due to symmetry and rigid body motions are properly constrained as shown in figure 3.4. Sides and top surfaces of the sample are thermally insulated which is reflected by imposing heat flux free boundary conditions on these surfaces. The stress/strain state is assumed to satisfy plane strain conditions, which is of course an approximation since the real stress state is 3-D due to loading conditions and specimen dimensions. The results of a 2-D analysis are reliable for a qualitative investigation and they are representative in terms of trends in damage distribution as a function of the model parameters.

A thermo-mechanical analysis is carried out to determine the evolution of stresses, damage and temperature within the domain. Based on the conservation of linear momentum and energy, the quasi-static mechanical equilibrium in terms of Cauchy stresses

$$\vec{\nabla} \cdot \sigma + \vec{b} = \vec{0} \quad (3.2)$$

and the transient heat conduction equation,

$$\rho c_v \dot{\theta} + \vec{\nabla} \cdot \vec{q} = 0 \quad (3.3)$$

apply. In here, \vec{b} is the body force vector, $\vec{\nabla}$ is the gradient operator with respect to the current configuration, c_v is the heat capacity, ρ is the density, θ is temperature and \vec{q} is the heat flux vector. In addition to external boundary conditions, along the material interfaces between the grains and the matrix, the conditions,

$$\vec{t}^+ = -\vec{t}^- \text{ and } q_i^+ = -q_i^- \quad (3.4)$$

have to be satisfied, where \vec{t} and q_i are the tractions and interface heat fluxes as shown in figure 3.4. Furthermore subscripts and superscripts + and – indicate that the interface is approached from two different bulk sides of the interface. Solution of these equations requires the constitutive laws for σ , \vec{q} and in the context of thermo-mechanical cohesive interfaces also for \vec{t} and q_n . In the following subsections, the constitutive laws for each phase, (grains, matrix and interfaces) are summarized.

3.4.1 Grains

In figure 3.5, microscopic images of thermally shocked samples are shown. As far as large alumina grains are concerned, these images support that micro-cracking occurs along the boundaries of large grains while the grains themselves remain intact. In addition to these experimental investigations, analytical studies on simplified material systems [7], reveal that above a critical grain size, upon a uniform temperature change, the cracking occurs along matrix-grain interfaces. Therefore the large alumina grains are assumed to behave elastic and not damaging. Based on the data given for 99.5 % pure alumina technical ceramics, the Young's modulus is taken to be 400 GPa with the corresponding temperature dependency as shown in figure 3.6. The same reference suggests a temperature independent value of 0.28 for Poisson's ratio. Similarly, temperature dependent conductivity, heat capacity and CTE of the grains are given in figure 3.7, based on the data given in [reference]. A linear relation between the Cauchy stresses and logarithmic strains is adopted and heat fluxes are determined by Fourier's law of heat conduction.

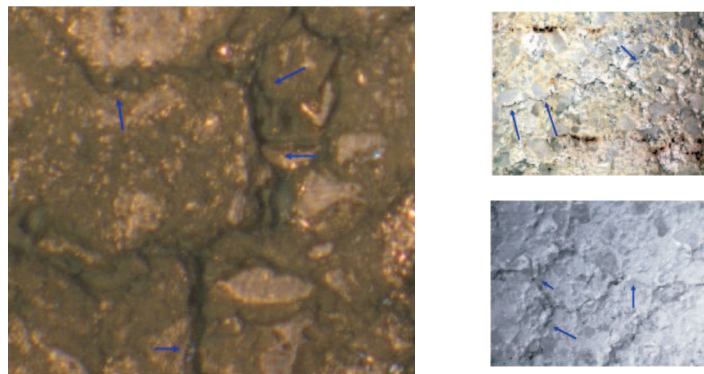


Figure 3.5: Microstructure after thermal shock (arrows indicating cracks)

3.4.2 Matrix

The failure within the matrix takes place through a distributed micro-cracking mechanism. In spite of remarkable achievements in the modeling of discontinuities by novel discretization techniques (X-FEM, generalized FEM), the resolution of complex micro-cracking processes such as multiple micro-cracking and crack bridging can not be tackled trivially with the aid of these tools. Therefore the failure of matrix phase is handled in an average sense by using a continuum damage mechanics (CDM) approach.

The volumetric percentages of mullite, alumina and porosity within the matrix are

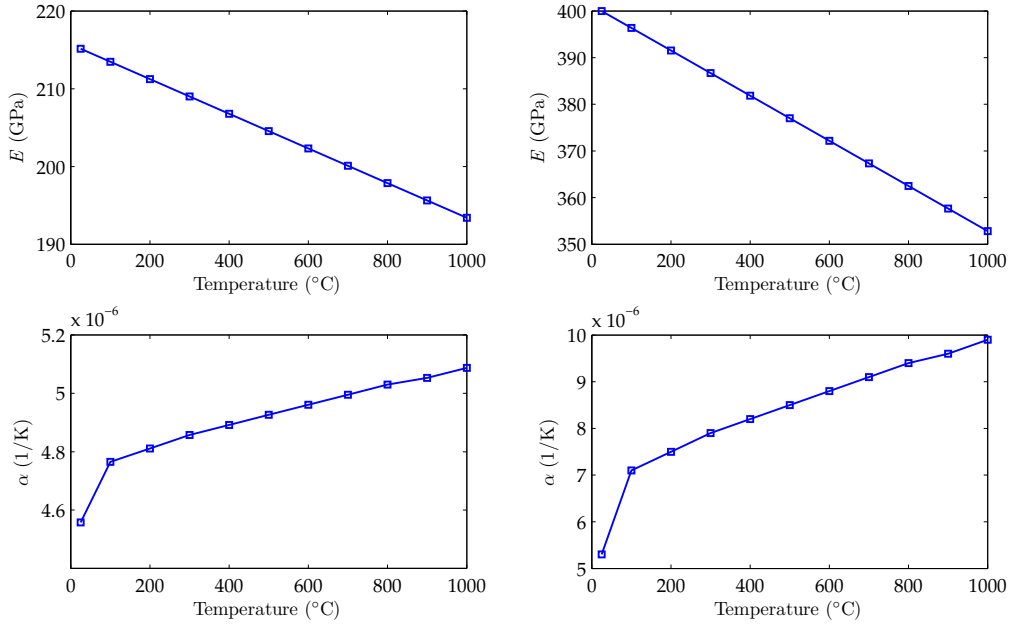


Figure 3.6: Temperature dependency of Young's Modulus (E) and coefficient of thermal expansion (α), left column for matrix, right column for grains; based on [47–50]

74.48 %, 11.52 % and 14 %, respectively. Mechanical and thermo-physical properties of the matrix are determined by the rule of mixtures, whereby the percentages of alumina and porosity are low in the matrix mixture. The resulting properties and their temperature dependencies are given in figure 3.6 and 3.7. As micro-cracks nucleate and propagate within the matrix phase, the coherent structure disintegrates and the stiffness of the matrix decreases. Continuum damage mechanics provides a versatile and computationally feasible framework to model the failure process in an average sense, in a continuum setting without resolving the discontinuities explicitly. The isotropic damage (D) is introduced as a field variable, which governs (determines) the current material stiffness as,

$$\mathbb{E} = (1 - D)\mathbb{E}_0 \quad (3.5)$$

where \mathbb{E} is the current stiffness tensor. The evolution of damage represents the onset or 'nucleation' of micro-cracks and the material gradually loses its stiffness until a complete crack is formed at $D=1$. The propagation is governed by the local stress/strain distribution within the close vicinity of the process zone. It can be shown easily that damage models based on a classical local continuum description yield results that are dependent on the spatial discretization. More precisely, the results converge to a non-physical solution upon mesh refinement, while less and less energy (zero in the limit) for crack propagation is required. By introducing non-locality in the damage law, either through spatial averaging or through gradient

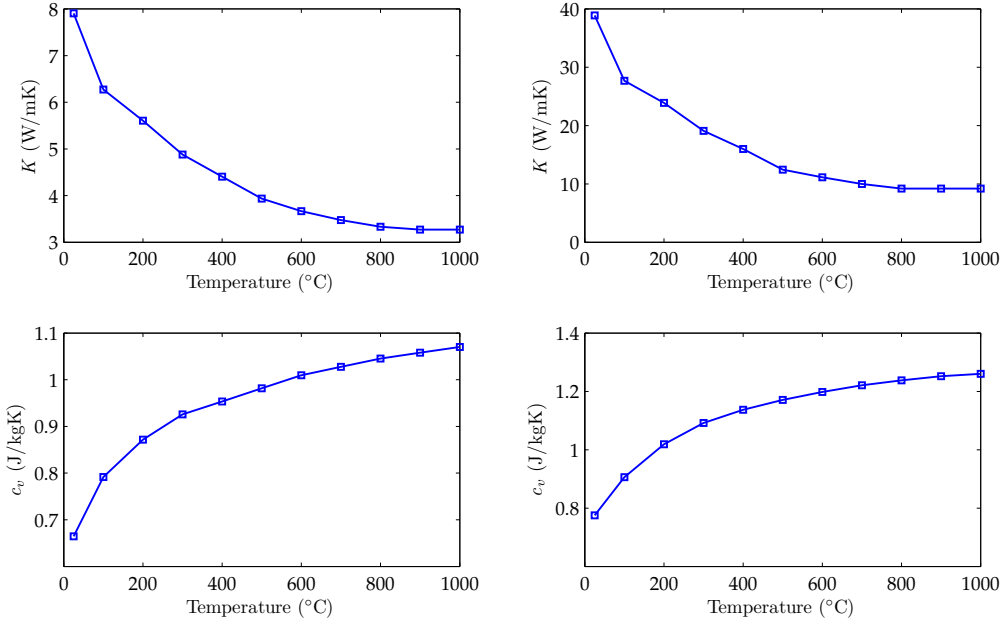


Figure 3.7: Temperature dependency of conductivity (K) and heat capacity (c_v), left column for matrix, right column for grains; based on [50–53]

terms, these non-physical results are avoided.

In here, the damage evolution is expressed as a function of a nonlocal equivalent strain and the damage increases as soon as the nonlocal equivalent strain level surpasses the maximum nonlocal equivalent strain value attained during loading history. In an implicit gradient formulation [54], non-local equivalent strain, $\bar{\epsilon}$, which governs the evolution of damage, is determined through the solution of the Helmholtz equation,

$$\bar{\epsilon} - l^2 \nabla^2 \bar{\epsilon} = \tilde{\epsilon} \quad (3.6)$$

which is driven by the local equivalent strain $\tilde{\epsilon}$ in the right-hand side. In equation 3.6, ∇^2 is the nabla operator and l is the internal length scale. Since the non-local strain is not given explicitly in terms of $\tilde{\epsilon}$ and its derivatives, but obtained through the solution of equation 3.6 over the domain, the resulting formulation is referred to as the implicit gradient formulation distinguishing it from explicit formulations existing in the literature.

The solution of equation (3.6) requires the definition of proper boundary conditions on the external boundaries and the boundaries between the matrix and the non-damaging grains, which are commonly adopted the natural boundary conditions,

$$\vec{\nabla} \bar{\epsilon} \cdot \vec{n} = 0 \quad (3.7)$$

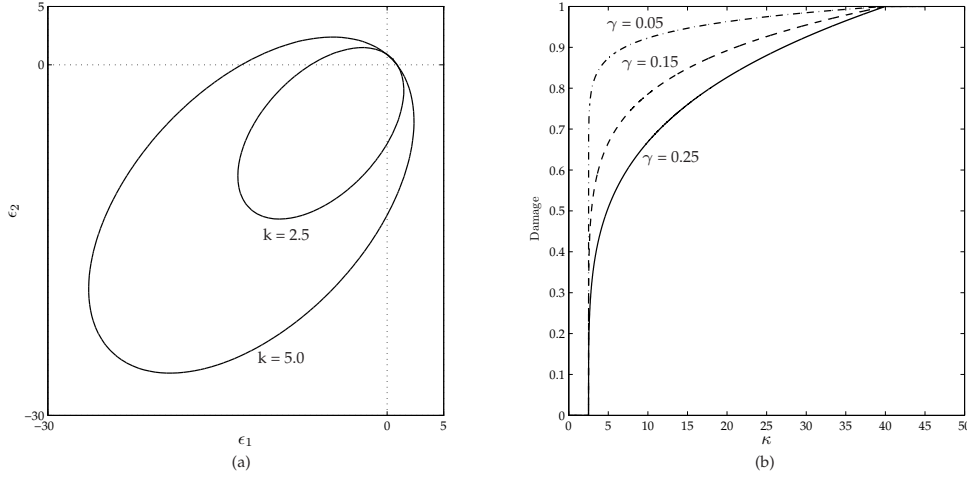


Figure 3.8: (a) Equivalent local strain definition in principal strain space (for $\bar{\epsilon} = 1.5$, $\mu = 0.2$, plane strain conditions) (b) Damage evolution law

Based on [55], the equivalent local strain is defined as,

$$\bar{\epsilon} = \frac{k-1}{2k(1-2\nu)} I_1 + \frac{1}{2k} \sqrt{\frac{(k-1)^2}{(1-2\nu)^2} I_1^2 - \frac{12k}{(1+\nu)^2} J_2} \quad (3.8)$$

where I_1 and J_2 are the first invariant of the strain tensor and second invariant of the deviatoric strain tensor, respectively. Under uni-axial loading conditions, the equivalent local strain is defined such that, a compressive stress of $k\sigma$ leads to the same damage growth as a tensile stress of σ . The characteristic large ratio of compressive strength vs. tensile strength of quasi-brittle materials is incorporated by the variable $k = \frac{f_c}{f_t}$. The particular damage law used here has the form,

$$D = \begin{cases} 0 & \text{if } \kappa < \kappa_0 \\ \left(\frac{\kappa - \kappa_0}{\kappa_f - \kappa_0}\right)^\gamma & \text{if } \kappa > \kappa_0 \\ 1 & \text{if } \kappa > \kappa_f \end{cases}$$

which is complemented with the conventional loading/unloading conditions,

$$\dot{\kappa} \geq 0, \quad \bar{\epsilon} - \kappa \leq 0, \quad \dot{\kappa}(\bar{\epsilon} - \kappa) = 0 \quad (3.9)$$

κ_0 denotes the damage initiation threshold and κ_f is the upper bound leading to a critical damage equalling unity. A constant- $\bar{\epsilon}$ curve and the damage evolution law are shown in figure 3.8. As the Poisson's ratio (ν) approaches to 0.5 and/or under strongly deviatoric strain states, special care has to be taken since the expression within the square root might become undefined or negative.

3.4.3 Interfaces

Since the mechanical behaviour and heat transfer mechanisms heavily depend on the status of the interfaces, the modeling and characterization of the interfaces are crucial. Refractory materials exhibit a quasi-brittle response upon mechanical loading which indicates that the micro-cracking mechanisms have a cohesive nature due to crack bridging mechanisms, connecting the surfaces of newly forming micro-cracks. Therefore, the interfaces between the grains and the matrix are modeled as thermo-mechanical cohesive zones where the load and heat transfer mechanisms weaken as the opening between the two faces of the newly forming crack (crack increment) increases. Direct experimental characterization of the interfaces still remains a challenging task for the experimentalists since it is intrinsically difficult to develop an experimental set-up and suitable samples that enable reliable measurements at such small scales. Therefore, the parameters of the traction-opening laws are determined inversely by using the thermal shock test results.

The cohesive nature of interfaces are described by the well-established mechanical interface relations through which the damage at the micro-crack tip is lumped into traction-opening relations. These relations are typically characterized by the shape of the response curve, fracture energy and the peak traction values. As reported in [22], the decisive parameters are the fracture energy and the strength of the interface rather than the particular formulation of the traction opening law. Therefore, in this chapter, normal and tangential tractions are described by the smooth expressions (improved Xu–Needleman traction–opening laws, see [56]),

$$t_n = \frac{\phi_n}{\delta_n} \left(\frac{\Delta_n}{\delta_n} \right) \exp \left(-\frac{\Delta_n}{\delta_n} \right) \exp \left(-\frac{\Delta_t^2}{\delta_t^2} \right) \quad (3.10a)$$

$$t_t = 2 \frac{\phi_t}{\delta_t} \left(\frac{\Delta_t}{\delta_t} \right) \left(1 + \frac{\Delta_n}{\delta_n} \right) \exp \left(-\frac{\Delta_t^2}{\delta_t^2} \right) \exp \left(-\frac{\Delta_n}{\delta_n} \right) \quad (3.10b)$$

where ϕ_n and ϕ_t are the fracture energies in pure opening and pure sliding modes, respectively [33]. δ_n and δ_t are the mechanical openings in normal and tangential directions as shown in figure 3.9, in a finite element discretization setting. For a consistent description of unloading-reloading, a damage parameter based on the definition of an effective opening measure,

$$\Delta_{eff} = \sqrt{\Delta_n^2 + \beta^2 \Delta_t^2} \text{ with } \beta = 0.5 \quad (3.11)$$

is introduced and the maximum effective opening attained is traced at every integration point of the interface element. Loading takes place when $\Delta_{eff} = \Delta_{max}$ and $\Delta_{eff} \geq 0$ and unloading (or reloading) when $\Delta_{eff} < \Delta_{max}$. In the context of thermo-mechanical loading, the heat conduction through the interfaces will decrease as well if the opening increases. In fact, the heat transfer through the solid phase is obstructed and the air filling the crack will act as a substitute secondary conducting medium for the heat flow between the two faces of the crack. To quantify the heat

flow along the interfaces on the basis of physical mechanisms, the mechanical interface description is supplemented with a thermal interface element description as presented in [57] where the heat flux through the interface is defined as,

$$q_i = \sqrt{q_n^2 + q_t^2} \quad (3.12)$$

with the components

$$q_n = ((1 - d)k_s + k_g) \llbracket \theta \rrbracket \vec{m} \cdot \vec{n} \quad (3.13a)$$

$$q_t = (1 - d)k_s \llbracket \theta \rrbracket \vec{m} \cdot \vec{t} \quad (3.13b)$$

to be determined at each integration point based on the interpolation

$$\begin{aligned} \llbracket \theta \rrbracket &= N_1 (\theta_{1+} - \theta_{1-}) \vec{m}_1 + N_2 (\theta_{2+} - \theta_{2-}) \vec{m}_2 \\ \text{with } \vec{m}_1 &= \frac{\vec{x}_{1+} - \vec{x}_{1-}}{\|\vec{x}_{1+} - \vec{x}_{1-}\|} \text{ and } \vec{m}_2 = \frac{\vec{x}_{2+} - \vec{x}_{2-}}{\|\vec{x}_{2+} - \vec{x}_{2-}\|} \end{aligned} \quad (3.14)$$

$\llbracket \theta \rrbracket$ is the temperature difference between two material points on opposite faces of the discontinuity which were coincident before the crack separated them, see figure 3.9. k^s and k^g are the conductance of the interface due to solid crack bridging mechanisms and the gas filling the cavity, respectively. The interface conductance can be considered as a penalty parameter which enforces an identical temperature value at both sides in the case of an undamaged interface. The interfacial damage parameter d of equation 3.12 is defined as the ratio $\frac{\Delta_{eff}^{max}}{\Delta_{crt}}$ where

$$\Delta_{crt} = \sqrt{\Delta_n^2|_{0.1t_n^{max}} + \beta^2 \Delta_t^2|_{0.1t_t^{max}}} \quad (3.15)$$

and $\Delta_{n,t}|_{0.1t_{n,t}^{max}}$ corresponds to the normal and tangential openings corresponding to the residual values $0.1t_n^{max}$ and $0.1t_t^{max}$ in the post-peak regime of the traction-opening curves, respectively. In case of crack closure, the contact conductance is mainly governed by the ratio of the actual contact area to the total interface area. A contact damage variable representing this ratio can be used in the case of crack closure as,

$$q_{n,c} = -((1 - d_c)k_s) \llbracket \theta \rrbracket \vec{m} \cdot \vec{n} \quad (3.16a)$$

$$q_{t,c} = 0 \quad (3.16b)$$

Since the fraction of crack bridges are expected to be dominant in crack closure as well, one can assume that $d_c \approx d$, as long as full separation did not occur.

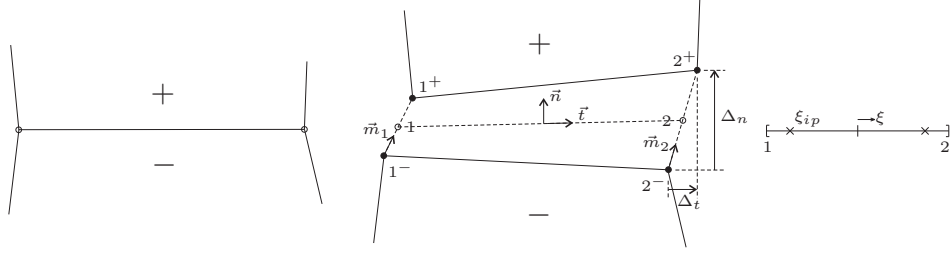


Figure 3.9: Two-noded interface element, undeformed and deformed configurations

3.4.4 Solution procedure

In addition to the quasi-static equilibrium and the heat balance, the nonlocality (Helmholtz) equation has to be fulfilled at every material point of the matrix. The quasi-static equilibrium equation and the Helmholtz equation are coupled through the direct dependence of stresses on the damage field and the dependence of damage values on the nonlocal equivalent strains.

An incremental-iterative solution procedure within a finite element framework, is adopted to solve the three coupled field equations. Here, instead of solving the coupled equations in a combined way, the global problem is split-up into three incrementally uncoupled problems

$$\int_V \vec{q} \cdot \vec{\nabla} \delta \theta dV = \int_{\Gamma_q} \bar{q} \delta \theta d\Gamma + \int_{\Gamma_i} (q_n|_+ (\delta \theta^+ - \delta \theta^-)) d\Gamma \quad (3.17a)$$

$$\int_V \sigma : \vec{\nabla} \delta \vec{u} dV = \int_V \vec{b} \cdot \delta \vec{u} dV + \int_{\Gamma_t} \vec{t} \cdot \delta \vec{u} d\Gamma + \int_{\Gamma_i} \vec{t}|_+ \cdot (\delta \vec{u}^+ - \delta \vec{u}^-) d\Gamma \quad (3.17b)$$

$$\int_{V_m} \bar{\epsilon} \delta \bar{\epsilon} dV - \int_{V_m} l^2 \vec{\nabla} \bar{\epsilon} \cdot \vec{\nabla} \delta \bar{\epsilon} dV = \int_{V_m} \tilde{\epsilon} \delta \bar{\epsilon} dV \quad (3.17c)$$

where $\Gamma_{\bar{q}}$ and $\Gamma_{\vec{t}}$ are the parts of external boundaries where the heat fluxes and the tractions are prescribed, respectively. Γ_i is the area of the grain-matrix interfaces and V_m is the matrix volume. These equations are solved sequentially within a time increment. Therefore, on a mechanically frozen state, the heat conduction equation is solved and the temperature profile is updated accordingly. Thereafter, the stress analysis is carried out with the updated temperature values but assuming a frozen damage state. Finally, the Helmholtz equation is solved with the equivalent strain values which are the driving force for the evolution of non-local equivalent strains. Typical increment of the resulting algorithm is summarized in table 3.2. The outlined solution procedure, has been successfully used in the context of numerical damage-plasticity simulations [58, 59]. The main disadvantage of the above operator-split solution procedure is its conditional stability which requires sufficiently small time steps. However, as soon as non-linearities are triggered, the incremental-iterative framework requires small time steps in any case. Therefore, the operator-split technique does not substantially increase the real computational costs.

Table 3.2: Staggered solution scheme for the thermo–mechanically induced damage analysis

<p>Next increment</p> <p>I. Thermal pass :</p> <p>(a) Next iteration</p> <ul style="list-style-type: none"> ▷ assemble the tangent conductivity ▷ solve the system and update θ ▷ loop over all integration points and calculate heat flux and tangent conductivity ▷ assemble the internal nodal fluxes ▷ check for convergence, if not repeat step (a), else continue <p>II. Mechanical pass :</p> <p>(b) Next iteration</p> <ul style="list-style-type: none"> ▷ assemble the tangent stiffness ▷ solve the system and update \underline{u} ▷ loop over all integration points and calculate stresses and material tangent ▷ assemble the internal nodal forces ▷ check for convergence, if not repeat step (b), else continue <p>III. Non–local field pass :</p> <ul style="list-style-type: none"> ▷ assemble the system matrices (left–hand side of equation 3.17c) based on updated geometry ▷ assemble the right–hand side of equation 3.17c based on the updated local equivalent strain $\bar{\epsilon}$ ▷ solve the system, update $\bar{\epsilon}$, κ and D ▷ continue with the next increment
--

3.4.5 Parameter identification procedure

As concisely mentioned in section 3.3, use is made of ultrasonic wave propagation measurements on thermally shocked specimens at various locations along the height as shown in figure 3.3; for a detailed treatment see [36]. Based on the wave speed measurements, the dynamic Young’s modulus is calculated using an inverse method. The same procedure is repeated for undamaged samples and based on the Young’s moduli ratio, the damage distribution curve along the height has been determined.

To use the experimental results as a reference to identify the parameters of the numerical model, the following static analysis procedure is pursued. From the computational model (DNS model), subjected to the thermal shock history, uni-axial ‘specimens’ are cut out at the locations corresponding to the positions of the transducers used for the measurements. The cross-section of the uni-axial specimens is determined by the size of the transducer. The damage and interface opening histories are transferred to these uni-axial specimens.

After extraction of these specimens, they are exposed to uni-axial tensile loading,

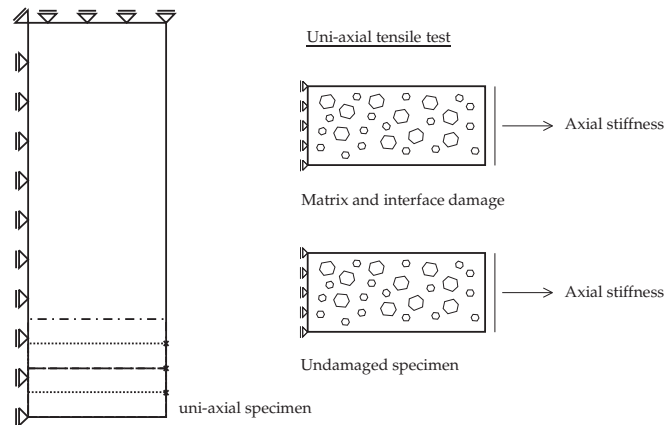


Figure 3.10: Equivalent static procedure

from which the axial static stiffness of the damaged specimen is determined and compared with the axial stiffness of the corresponding undamaged specimen, see figure 3.10.

Following this procedure, the damage evolution law and interface parameters are tuned towards the computational results presented on figure 3.11(a). Internal length scale of the matrix damage model is taken as 0.4 mm based on the edge length of the small grains which is linked to the stress ligaments developing between the grains. Preliminary computations indicated that the damage values at locations far from the thermally shocked end of the specimen are essentially determined by the matrix damage parameters κ_0 and κ_f . These values are taken as $0.08 \cdot 10^{-5}$ and $0.09 \cdot 10^{-2}$ which yielded good agreement with the experimental results.

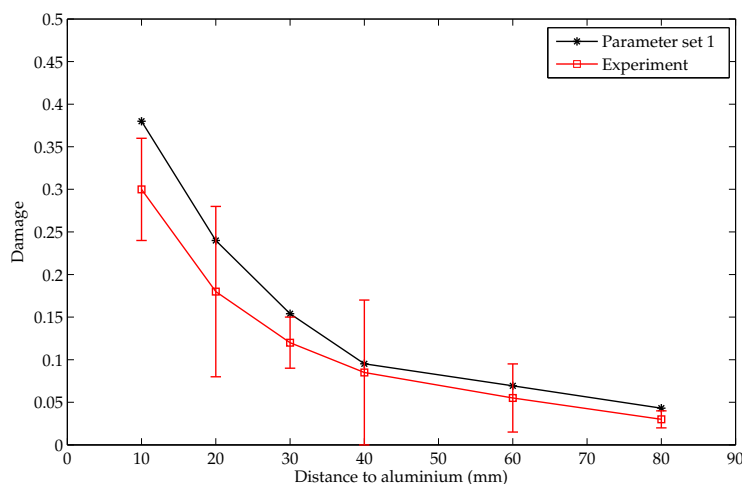
Computational results capture the experimentally observed trends well whereas quantitatively the results are over estimating the damage distribution particularly in the close neighborhood of the thermally shocked end of the sample. In this context, it is important to re-emphasize the fact that the experimental measurements result in dynamic Young's modulus whereas the computational results are static values. Typically, the dynamic modulus tends to be smaller than the one estimated from the static modulus [36], as done in the model.

It is important to note that the computational results could have been reproduced by using a different set of parameters. In other words, the identified parameters are non-unique essentially due to the lack of experimental data.

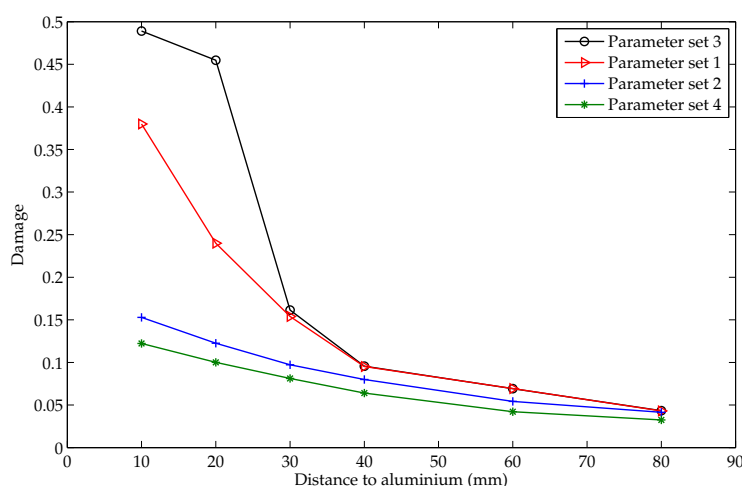
3.4.6 Parametric study

To investigate the influence of different material parameters, a parametric study is carried out which uses the equivalent static procedure as the basis for damage quantification.

Fully resolved models are particularly powerful in capturing the direct influence of



(a)



(b)

Figure 3.11: (a) Damage distribution along the height, experimental vs. computed results (b) Damage distribution with different interface parameters

parameters which are difficult to incorporate into equivalent homogenous continuum models. In this context, first the mechanical strength of the interfaces is considered. In figure 3.11(b), computational results with 4 different parameter sets are presented. The model without mechanical interfaces (fully bonded) yields the lower bound solution (parameter set 4), as seen from the figure. The damage values in the close vicinity of the thermally shocked end are increasing as the strength of the interfaces increases with the same fracture energies (more brittle interface). The resulting damage distribution for the bottom strip is shown in figure 3.12 for two different cases. As seen from the figure, islands of fully damaged zones are formed for higher strength values.

In fact, the damage is initiated in the compression regions between the grains. As the

	Set 1	Set 2	Set3	Set4	Set 5
$\phi_n(\text{J/m}^2)$	25	25	25	-	25
$\phi_t(\text{J/m}^2)$	50	50	50	-	50
$t_n^{\max}(\text{MPa})$	42	14	56	-	700
$t_t^{\max}(\text{MPa})$	84	28	112	-	1400
κ_0	$0.08 \cdot 10^{-5}$	$0.08 \cdot 10^{-5}$	$0.08 \cdot 10^{-5}$	$0.08 \cdot 10^{-5}$	$0.08 \cdot 10^{-5}$
κ_f	$0.09 \cdot 10^{-2}$	$0.09 \cdot 10^{-2}$	$0.09 \cdot 10^{-2}$	$0.09 \cdot 10^{-2}$	$0.09 \cdot 10^{-2}$
γ	0.95	0.95	0.95	0.95	0.95
$l(\text{mm})$	0.4	0.4	0.4	0.4	0.4

Table 3.3: Model parameters used for different cases

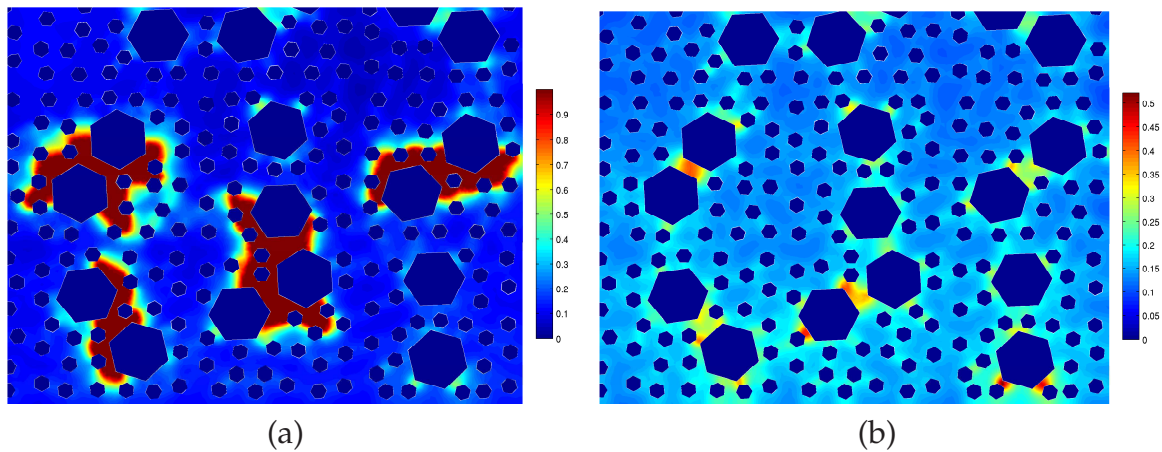


Figure 3.12: Damage distribution at the bottom strip of the sample, (a) based on parameter set 1 (b) based on parameter set 2

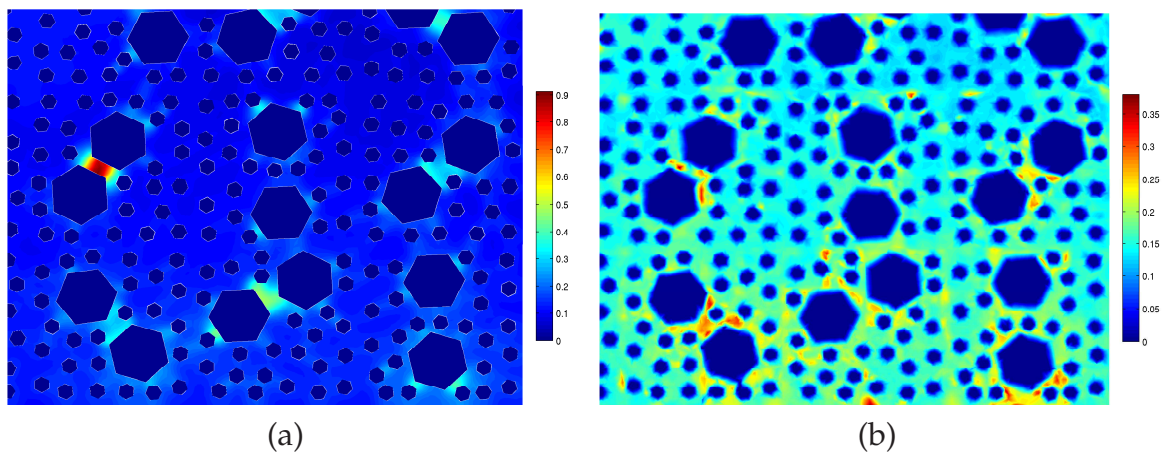


Figure 3.13: Damage distribution at the bottom strip of the sample, (a) based on parameter set 5 (b) based on parameter set 4 (without interfaces)

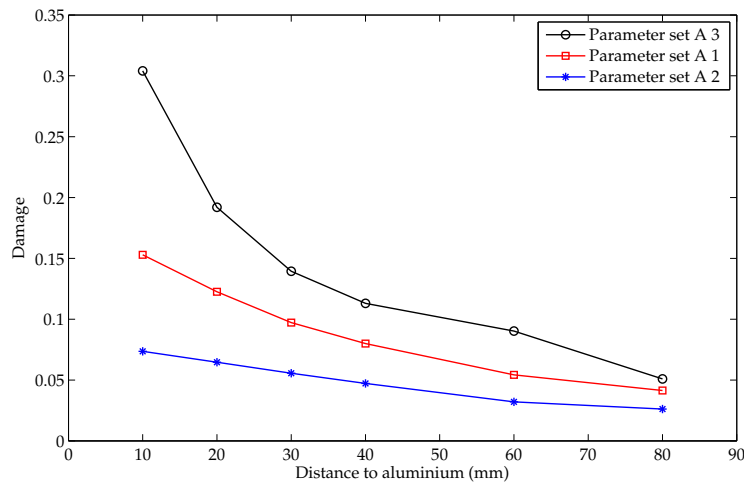
interface becomes more brittle, especially the tangential openings (sliding) of the interfaces located on the faces of larger grains get larger (compared to the more ductile case) whereby the grains tend to rotate due to geometric lay-out. It means that the compressive action between the grains and the matrix becomes pronounced, leading to high damage values. The damage spreads to a certain area as the compressive region evolve as the matrix damages. Accordingly, as the traction strengths are further increased as done with parameter set 5, the failure pattern disappears, see figure 3.13, as the tangential opening values become very small since almost all of the interfaces remain within the pre-peak, stiff regime of the traction-opening relations. In the limit, the pattern should approach to the case where there are no interfaces in the system (i.e. fully bonded), which is presented in figure 3.13. Motivated by the ‘short range’ and ‘long range’ effects introduced in section 3.1, the influence of the CTE mismatch between the grains and the matrix (‘short range’ effect) is investigated next. As shown in figure 3.14(a), in case of identical CTE’s, damage values are much smaller than in the reference case. On the other hand, a slight increase in the CTE mismatch yields a considerable difference in the resulting damage profile, which indicates a strong sensitivity.

In figure 3.14(b), the damage values obtained by increasing the matrix stiffness are compared with the reference solution (parameter set E 1 and E 2, table 3.5). A more stiff matrix results in reduced damage values throughout the specimen.

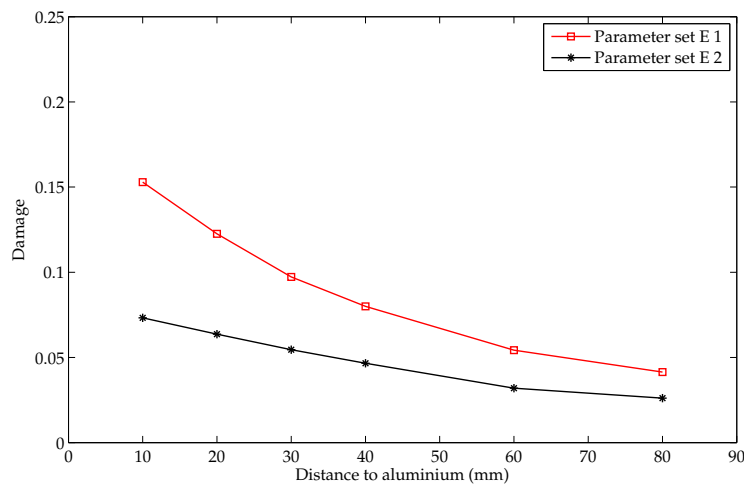
	A 1	A 2	A 3	K 1	K 2	K 3
$\phi_n(\text{J/m}^2)$	25	25	25	25	25	25
$\phi_t(\text{J/m}^2)$	50	50	50	50	50	50
$t_n^{\text{max}}(\text{MPa})$	14	14	14	14	14	56
$t_t^{\text{max}}(\text{MPa})$	28	28	28	28	28	112
κ_0	$0.08 \cdot 10^{-5}$	$0.08 \cdot 10^{-5}$	$0.08 \cdot 10^{-5}$	$0.08 \cdot 10^{-5}$	$0.08 \cdot 10^{-5}$	$0.08 \cdot 10^{-5}$
κ_f	$0.09 \cdot 10^{-2}$	$0.09 \cdot 10^{-2}$	$0.09 \cdot 10^{-2}$	$0.09 \cdot 10^{-2}$	$0.09 \cdot 10^{-2}$	$0.09 \cdot 10^{-2}$
γ	0.95	0.95	0.95	0.95	0.95	0.95
$l(\text{mm})$	0.4	0.4	0.4	0.4	0.4	0.4
$K_m(\text{W/m}^2\text{K})$	7.91	7.91	7.91	7.91	79.1	79.1
$K_g(\text{W/m}^2\text{K})$	38.90	38.90	38.90	38.90	389.0	389.0
$E_m(\text{GPa})$	215.14	215.14	215.14	215.14	215.14	215.14
$E_g(\text{GPa})$	400	400	400	400	400	400
$\alpha_m(1/\text{K})$	$4.56 \cdot 10^{-6}$	$4.56 \cdot 10^{-6}$	$4.56 \cdot 10^{-6}$	$4.56 \cdot 10^{-6}$	$4.56 \cdot 10^{-6}$	$4.56 \cdot 10^{-6}$
$\alpha_g(1/\text{K})$	$5.3 \cdot 10^{-6}$	$4.56 \cdot 10^{-6}$	$5.472 \cdot 10^{-6}$	$5.3 \cdot 10^{-6}$	$5.3 \cdot 10^{-6}$	$5.3 \cdot 10^{-6}$

Table 3.4: Model parameters used for different cases (room temperature values)

The ‘long range’ effect is associated with the temperature gradient which is determined by the diffusivity of the material and the heat transfer conditions across the boundaries. To investigate this effect, the conductivities of the both phases have been



(a)



(b)

Figure 3.14: (a) Damage distribution as a function of CTE mismatch (b) Damage distribution as a function of matrix stiffness

increased significantly as reported in table 3.4 (parameter set K 1 and K 2). The resulting temperature profile along the indicated section for two cases are shown in figure 3.15. In case of higher conductivities, the temperature difference between the top and bottom faces of the specimen gets considerably smaller compared to the reference case, which also implies a deformation mode closer to a homogenous state. The resulting damage values are shown in figure 3.16. This result suggests that as the temperature profile gets milder, the damage values tend to be smaller and approximately constant throughout the specimen. To investigate the influence of interfaces when the material is highly conductive, another set of computations is carried out as given in table 3.4 (parameter set K 3). The results given in figure 3.16(b) suggests that as the material gets more conductive, the influence of interface parameters be-

	E 1	E 2
ϕ_n (J/m ²)	25	25
ϕ_t (J/m ²)	50	50
t_n^{\max} (MPa)	14	14
t_t^{\max} (MPa)	28	28
κ_0	$0.08 \cdot 10^{-5}$	$0.08 \cdot 10^{-5}$
κ_f	$0.09 \cdot 10^{-2}$	$0.09 \cdot 10^{-2}$
γ	0.95	0.95
l (mm)	0.4	0.4
K_m (W/m ² K)	7.91	7.91
K_g (W/m ² K)	38.90	38.90
E_m (GPa)	215.14	322.71
E_g (GPa)	400	400
α_m (1/K)	$4.56 \cdot 10^{-6}$	$4.56 \cdot 10^{-6}$
α_g (1/K)	$5.3 \cdot 10^{-6}$	$5.3 \cdot 10^{-6}$

Table 3.5: Model parameters used for different cases (room temperature values)

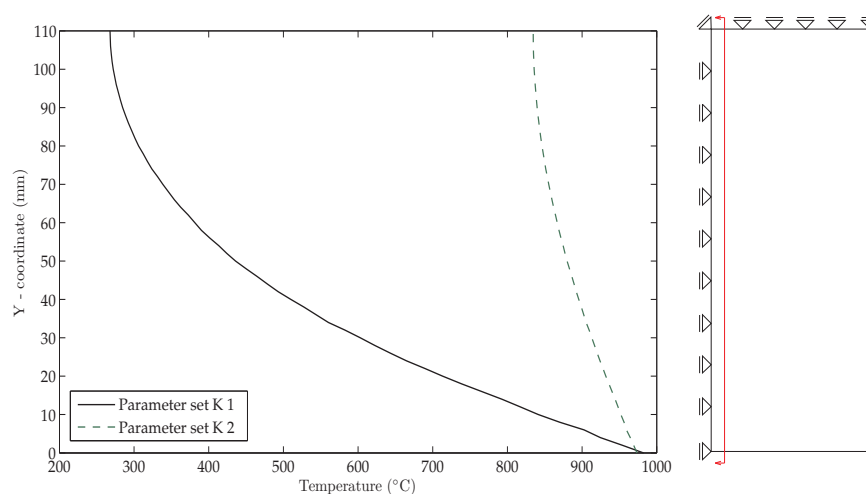
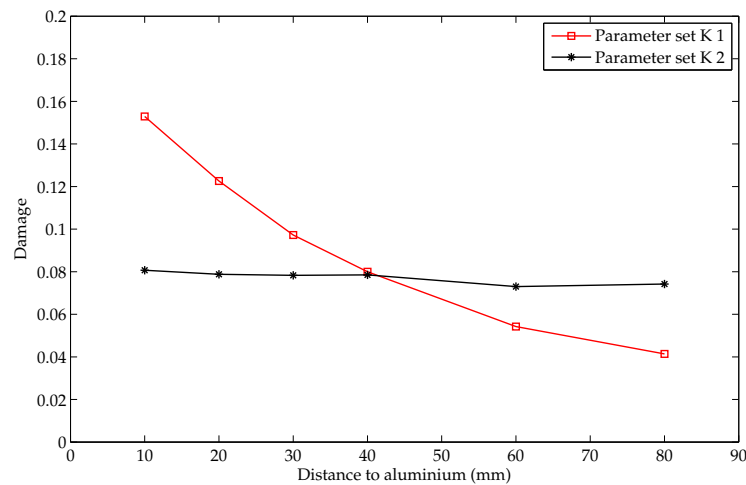
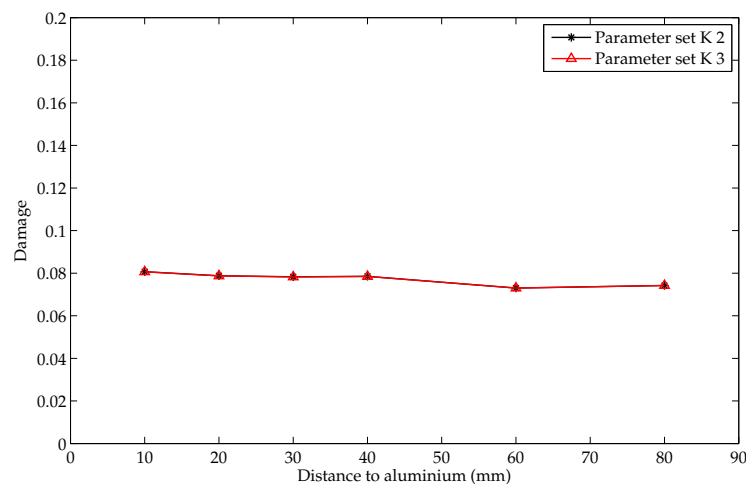


Figure 3.15: Temperature profile at the end of loading history for parameter set K 1 and K 2

come negligible since the two data sets are almost coincident. As the deformation approaches to a homogenous state, the interfacial characteristics become less influential.



(a)



(b)

Figure 3.16: (a) Damage distribution for a more conductive material, (b) influence of the interface strength in case of more conductive material

3.5 Summary and Conclusion

On the basis of an idealized two phase material system, direct numerical simulations are used to investigate the thermal shock response of refractory ceramics. Molten aluminium tests are reproduced within a computational framework and the parameters of the model are identified relying on a static equivalent computational procedure. Furthermore the influence of certain material parameters are investigated qualitatively.

On the basis of this parametric study, it can be concluded that:

- In case of strong temperature gradients, the damage evolution is markedly sen-

sitive to the CTE mismatch between the phases. Damage values increase significantly as a result of a slight change in the contrast between the CTE of the phases.

- The brittleness of the interfaces has a strong influence as long as there exists a strong temperature gradient. More brittle interfaces (with a limited strength) yield higher damage values. However, as the temperature profile gets milder, the influence of the mechanical characteristics of the interfaces become less significant.
- For highly conductive materials, the damage distribution tends to be uniform throughout the specimen. The influence of interface parameters diminishes since the deformation mode is approaching a homogenous state and the damage values are smaller since the CTE mismatch is the only mechanism of the damage evolution.
- Increasing the stiffness of the matrix has a favorable effect in the context of thermal shock response since the damage values are getting smaller.

Obviously, a more extensive parametric study can be carried out to investigate the relations between different parameters. Nevertheless, the modeling approach and the parametric study provides information on the mechanisms of damage evolution and the significance of certain parameters of the material system of interest. Such information can not be extracted on the basis of a continuum model which does not consider the heterogeneities explicitly. Furthermore, the identified parameters can be useful in a multi-scale modeling framework.

CHAPTER FOUR

Computational Homogenization for Heat Conduction in Heterogeneous Solids¹

Abstract

In this chapter, a multi-scale analysis method for heat transfer in heterogeneous solids is presented. The principles of the method rely on a two-scale computational homogenization approach which is applied successfully for the stress analysis of multi-phase solids under purely mechanical loading. The present chapter extends this methodology to heat conduction problems. The flexibility of the method permits one to take into account local microstructural heterogeneities and thermal anisotropy, including nonlinearities which might arise at some stage of the thermal loading history. The resulting complex microstructural response is transferred back to the macro level in a consistent manner. A proper macro to micro transition is established in terms of the applied boundary conditions and likewise a micro to macro transition is formulated in the form of consistent averaging relations. Imposition of boundary conditions and extraction of macroscopic quantities are elaborated in detail. A nested finite element solution procedure is outlined and the effectiveness of the approach is demonstrated by some illustrative example problems.

¹Based on: I. Özdemir, W.A.M. Brekelmans, M.G.D. Geers (2008). Computational Homogenization for Heat Conduction in Heterogeneous Solids. *International Journal for Numerical Methods Engineering*, 130(3).

4.1 Introduction

Materials with a high temperature resistance are indispensable in many engineering applications. Refractories used in furnace linings, thermal coatings and microelectronic components are just a few examples indicating the wide range of applications where a structure is exposed to strong temperature changes and cycles. The materials selected for such applications are generally far from being homogeneous due to their multi-phase, porous microstructure. Under severe thermal conditions, it is well documented that the damage mechanism originates from the induced stress gradients, the thermal expansion anisotropy and the non-uniformity and mismatches between the constituents at the meso or micro level [7]. Therefore an accurate prediction of the deterioration process and failure of such components requires a comprehensive understanding of the temperature distribution at all relevant levels of observation, e.g. at the meso and micro level.

Initial research efforts to analyze the behavior of heterogeneous solids were based on variational principles which resulted in bounds for the effective material properties [60]. The approach has been applied to thermo-elasticity problems to derive bounds for the thermal expansion coefficient and was further improved to yield tighter bounds on the effective properties [61, 62]. In order to obtain closed form expressions for effective properties rather than bounds, analytical models were developed that are mainly based on the solution of the problem of an inclusion in an infinite medium. A concise overview of different approaches in the context of heat conduction problems and a comparative study are presented in [63]. However, the predictions of these analytical and variational approaches are restricted to relatively simple geometries with a simple material response, not yielding accurate results when the contrast between the properties of the constituents is large, or when non-continuous interfaces are present.

Asymptotic homogenization approaches, which were originally developed for the solution of differential equations with periodic coefficients, have been exploited for the determination of the (mechanical) constitutive tensor of composites with a periodic microstructure. The method is based on an asymptotic expansion of the unknown field with respect to a micro-scale length parameter, yielding homogenized properties upon truncation of higher-order terms. Due to its generality, this approach is also applicable to different field problems as for instance heat conduction problems [64], including higher order models used to capture size effects [65].

The finite element solution of the fine-scale problem considered in an asymptotic homogenization framework, from which the relevant material characteristics were obtained numerically, led to the homogenization approach which is introduced in [66]. The method has been extended for thermo-mechanics and the heat conduction problem in [67–70]. This solution strategy departs from the asymptotic expansion of the temperature field in addition to the displacement field and ends up with a homogenized thermal conductivity and thermal expansion coefficients which in turn are used for the solution of the macroscopic thermo-mechanical problem [71, 72]. How-

ever, the problems considered were restricted to small strain linear thermo-elasticity and constant conductivity. Moreover, the steady-state heat conduction problem was the main point of interest whereas for some cases the transient effects are pronounced and non-negligible, e.g. in the case of thermoshock.

Relying on the steady evolution of computational tools, analysis methods which are based on the determination of the response from the underlying physics at the finer scales, according to a so-called multi-scale approach, have become feasible. The basic idea is to construct a link between two scales and investigate the interaction between the microstructure and the resulting macroscopic property by using basic material models at the level of single phases on the micro-scale. A particularly relevant strategy is the computational homogenization approach [15–18,73–75], which can be considered as a variant of a global-local analysis. Essentially, the macroscopic predictions are not based on closed-form constitutive equations but the entire material response is computed numerically at each material point by detailed modeling of the microstructure at the point under consideration.

Due to its high computational cost, some alternatives trying to approximate the problem at the micro level with a reduced number of unknowns have been constructed [76,77]. A particularly relevant one is presented in [76] in which the microstructure is divided into subcells with an assumed order of temperature distribution, in which the unknown coefficients are determined by enforcing the compatibility conditions at the subcell walls. Temperature dependency of conductivity is taken into account. The procedure circumvents the heavy computational work but deviates from the experimental data for some geometrical configurations, e.g. twisted yarns. Microstructural details and accuracy of the temperature field at the micro level is important for failure scenarios which initiate from a micro mechanism, e.g. debonding at a fiber matrix interface [78]. Therefore, detailed microstructural information, which can be incorporated via computational homogenization, is essential for reliable material response predictions. Furthermore, novel approximate techniques may be properly assessed by taking the computational homogenization results as a reference.

Almost all material properties depend on temperature. Hence a comprehensive understanding and modeling of the governing phenomena within a multi-scale formalism requires reliable temperature information at all relevant scales. The goal of the present contribution is to construct a computational homogenization approach for the coupled multi-scale analysis of evolving thermal fields in heterogeneous solids with complex microstructures including temperature and orientation dependent conductivities. The proposed framework is based on principles used in the computational homogenization approach for stress analyses as presented in [17] and up to the authors' knowledge has not been introduced for thermal problems before. It will be shown that, the construction of the framework for heat conduction problems poses some fundamental differences compared to its mechanical counterpart and therefore requires a comprehensive treatment.

The chapter is outlined as follows. In the next section, the basic principles and assumptions are introduced. Then the problems at the two levels are defined, i.e. at

macro and at micro scale. Scale transitions are presented in terms of appropriate boundary conditions and the consistency of the bridging structure is shown on the basis of physically motivated principles. The two scale computation strategy with a nested solution algorithm is briefly described thereafter. Finally, the applicability and the potential of the method is demonstrated on the basis of two example problems followed by some concluding comments.

4.2 Preliminaries

Computational homogenization is a multi-scale analysis approach in which the material response is obtained from the underlying microstructure by solving a boundary value problem defined on a representative volume of the microstructure. Although multiple scales can be embedded within the framework, in this particular case, two distinct levels (scales) are considered which will be referred to as the macro level for the engineering structure and the micro level for the typical fine scale microstructure of the material under investigation. As will be clarified shortly, there are some basic principles to be taken into account in the definition and distinction of the different scales. First, the fundamental steps of the computational homogenization will be introduced as schematized in figure 4.1.

As illustrated in figure 4.1, idealization and discretization of an engineering structure towards the solution of a boundary value problem results in a computational model which is used to predict the response, e.g. mechanical or thermal, of the structure under certain loading conditions. To begin with, computational homogenization requires the definition of a microstructural representative volume element (RVE) where characteristic physical and geometrical properties of the fine scale (different phases, internal boundaries, flaws etc.) are embedded. The scale bridging from macro to micro is achieved by the formulation of consistent boundary conditions in terms of macroscopic quantities passed to the micro level (RVE input, shown as step I in figure 4.1). Then, the microscopic field excited by the prescribed boundary conditions is resolved by a proper discretization technique applied to the micro-scale BVP (step II in figure 4.1). The resulting microscopic quantities are used to extract the macroscopic quantities (step III in figure 4.1) via a consistent averaging scheme. Furthermore, the linear relation between infinitesimal variations of the RVE output quantities in relation to infinitesimal variations of the input quantities are extracted, i.e. the tangent operator.

In fact, the relevant quantities at both scales involved in the boundary value problem statement are resolved numerically by the finite element method.

The scale separation made in such a framework relies on some basic assumptions. The composition of any heterogeneous solid can generally be considered as an assembly of different phases, imperfections, flaws and interfaces. However, as the characteristic dimensions of these microstructural features are still much larger than the molecular dimensions, the use of a continuum approach at this level remains

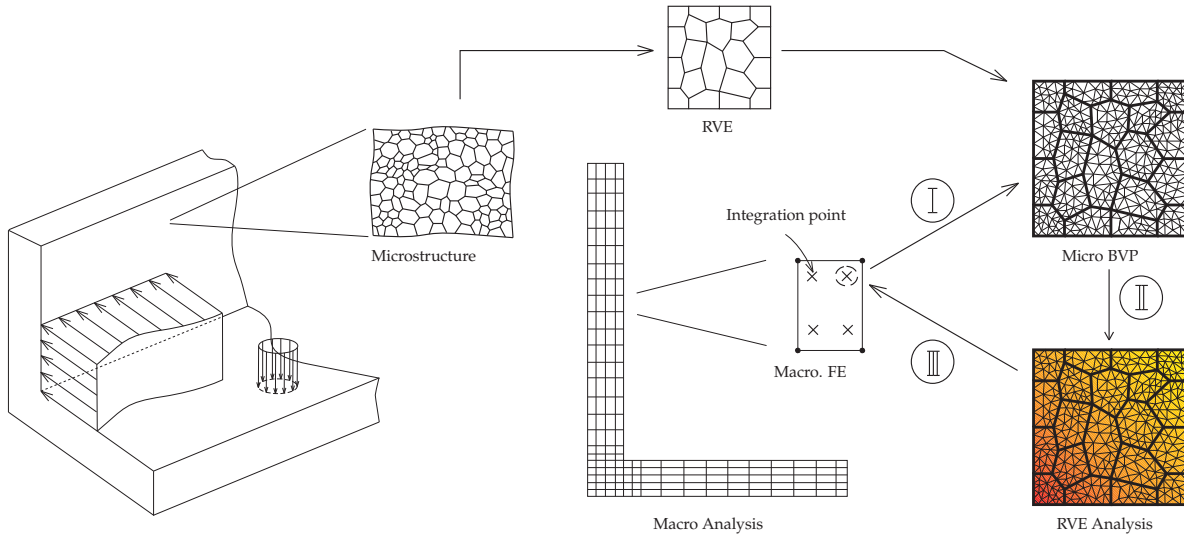


Figure 4.1: Schematic representation of the computational homogenization scheme

justified. Meanwhile, the microscopic length scale is often much smaller than the characteristic length over which the macroscopic excitation varies in space. The distinct hierarchy of scales is known as the principle of scale separation. This principle states that the characteristic length scale over which the macroscopic field variables vary, should be much larger than the size of the microscopic volume considered. In other words, macroscopic quantities are nearly constant at the level of an RVE. Consequently, the presented framework loses its reliability and validity as the spatial profile of the macroscopic temperature gradient gets steeper within typical RVE sizes used in the model.

In a conventional heat conduction analysis, the conductivity tensor determining the heat flux vector is expressed in closed form in terms of material parameters and state variables which requires dedicated experimental investigations especially for heterogeneous materials. However, in computational homogenization, the heat flux vector and conductivity tensor are extracted from the solution of a micro heat flow analysis carried out at the RVE level. To elaborate the principles further, a rectangular 2D RVE will be considered in the sequel, without loss of generalization to three dimensional cases. In a computational finite element setting, at each macroscopic integration point, temperature and temperature gradient will be calculated through interpolation of the (iteratively corrected) nodal temperature data. This set of macroscopic data is used to define the boundary conditions to be imposed on the microscopic problem associated with this particular integration point. After solving the microscopic RVE boundary value problem (BVP), the macroscopic heat flux is obtained by volume averaging the resulting heat flux field over the RVE and the macroscopic (tangent) conductivity is extracted from the microstructural conductivity. Due to the negligibly small size of the microstructural domain, the heat conduction at the micro level will be assumed to be insensitive to the time variations of the heat storage at this level. In other words, it may be assumed that a steady-state micro temperature pro-

file is reached instantaneously. Additionally, the thermal constitutive behaviour of each phase at the micro level is assumed to be known, which in general is governed by Fourier's law of heat conduction. On the other hand, the macroscopic heat flow problem remains completely general, i.e. transient with any kind of boundary conditions and does not require an explicitly formulated thermal constitutive behaviour.

Following the proper definitions of the problem at both scales in sections 4.3.1 and 4.3.2, the micro to macro scale transition (step I) will be elaborated in section 4.4.1. Next, a consistent scheme for the micro to macro transition will be introduced in section 4.4.3. The solution of the boundary value problem at the micro level (step II) and the extraction of the macroscopic quantities (step III) will be treated in section 4.5 in detail.

In what follows, the superscript or subscript 'M' denotes macroscopic quantities whereas a lower case 'm' will be the indicator for microscopic quantities, including some differential operators, e.g. the gradient operator $\vec{\nabla}_M$ or $\vec{\nabla}_m$. Following conventions are used in the notations of vectors, tensors and related products:

- scalars a
- vectors \vec{a}
- second order tensors \mathbf{A}
- matrices and rows/columns \underline{A} or \underline{a}
- $\vec{a} \cdot \vec{b} = a_i b_i$
- $\mathbf{A} \cdot \vec{a} = A_{ij} a_j \vec{e}_i$

At both scales, the componentwise representation of the vectors, tensors and gradient operators are based on a common cartesian basis with the triad, $\vec{e}_1, \vec{e}_2, \vec{e}_3$.

4.3 Formulation of the Thermal Problem at Both Scales

4.3.1 Micro-scale problem

The micro scale problem is defined on a representative volume element (RVE), where physical and geometrical properties of the material microstructure components are embedded. The choice of the RVE is a delicate task, particularly for materials with random microstructures, see e.g. [79]. Here it is assumed that the appropriate RVE has already been selected.

Due to negligibly small RVE size, the time variation of the heat storage may be neglected within the microstructural domain (see section 4.2). This assumption leads

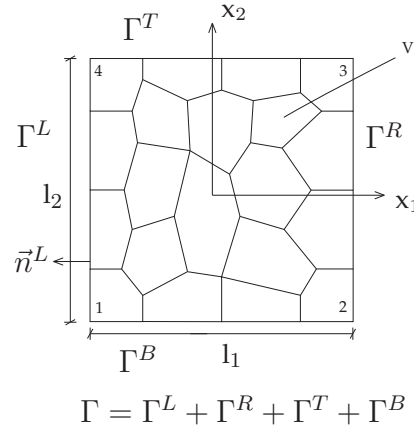


Figure 4.2: Micro-domain

to the steady-state micro thermal equilibrium which is expressed as

$$\vec{\nabla}_m \cdot \vec{q}_m(\vec{x}) = 0 \quad (4.1)$$

where \vec{q}_m is the microscopic heat flux vector. In a two-dimensional context, a rectangular micro domain is shown in figure 4.2. The volume of the RVE is designated by V and the boundaries, Γ , are labeled with L(left), R(right), T(top) and B(bottom). The same convention is also used for the unit outward normal vectors along the boundaries, e.g. \vec{n}^L . Four corner points are numbered in counter-clockwise direction starting from the lower left corner as shown in figure 4.2. For the solution of equation (4.1) in V , the boundary value problem needs to be complemented with proper boundary conditions which can be formulated in terms of a prescribed temperature or a prescribed normal heat flux on the boundary Γ . As mentioned in section 4.2, the thermal characterization of the microstructural components is described by Fourier's law of heat conduction, through which the microscopic heat flux \vec{q}_m can be determined. It is important to note that there are no a priori restrictions on the specification of the constitutive laws and material parameters (e.g. constant, temperature dependent and/or anisotropic) other than the basic thermodynamical limitations.

4.3.2 Macro-scale problem

At the macro level, the heat balance equation takes the general time dependent form according to

$$(\rho c_v)_M \dot{\theta}_M + \vec{\nabla}_M \cdot \vec{q}_M = 0 \quad (4.2)$$

where θ_M , \vec{q}_M and $(\rho c_v)_M$ represent the temperature, the heat flux and the heat capacity, respectively. This balance equation is to be complemented by macroscopic boundary conditions and additionally by initial conditions. Within a general setting, numerical approximation techniques (i.e. the finite element method) have to be used

to solve the macroscopic heat flow problem.

Within the proposed computational homogenization procedure the heat flux is obtained from the solution of the micro-scale thermal problem, which is defined on the underlying microstructure. In addition to the macroscopic heat flux, the discretized weak form of the macroscopic governing equation requires the homogenized conductivity for the solution of the resulting system of equations. The evaluation of the macroscopic heat flux and the extraction of the macroscopic conductivity are elaborated in the following sections.

For the determination of the macroscopic heat storage to be substituted in eq. (4.2) the following volume averaging is proposed

$$(\rho c_v)_M = \frac{1}{V} \int_V (\rho c_v)_m dV \quad (4.3)$$

which can be also obtained by the asymptotic homogenization method as done in [64]. This equation reflects that the heat capacity is consistently preserved upon scale bridging. In a computational context, in addition to the macroscopic heat flux and the conductivity, also the macroscopic volumetric heat capacity parameter, i.e. $(\rho c_v)_M$ in eq. (4.3) should be extracted from the micro level in case of a macroscopically transient problem.

4.4 Scale Transitions

4.4.1 The macro-micro scale transition

Within the framework of a multi-scale analysis, the actual microscopic temperature profile, $\theta_m(\vec{x})$ with \vec{x} the position vector, can be decomposed without loss of generality in a spatially linear mean (macroscopic) field and a fluctuation field $\theta_f(\vec{x})$ as

$$\theta_m(\vec{x}) = \theta_m^k + \vec{\nabla}_M \theta_M \cdot (\vec{x} - \vec{x}^k) + \theta_f(\vec{x}) \quad (4.4)$$

which can be interpreted as a perturbation of a mean (macroscopic) field with a fluctuation at the micro scale due to variations in material properties (e.g. conductivity) within the RVE. In eq. (4.4), θ_m^k is the temperature at an arbitrary point, \vec{x}^k , within the RVE and yet undetermined.

More conveniently, the microscopic temperature profile can be expressed with respect to the temperature value of corner 1 according to

$$\theta_m(\vec{x}) = \theta_m^1 + \vec{\nabla}_M \theta_M \cdot (\vec{x} - \vec{x}^1) + \theta_f(\vec{x}) \quad (4.5)$$

which can simply be accomplished using the difference of the temperature value of corner 1 and the temperature value of any other arbitrary point according to eq. (4.4).

In eq. (4.5), θ_m^1 is the microscopic temperature value at corner 1 with position vector \vec{x}^1 .

The temperature profile at the micro level results from the imposed boundary conditions and the distinct conductivities of the microstructural phases, which may be temperature dependent. Therefore, the determination of the reference temperature in the micro domain, which has been indicated by θ_m^1 , is important for an adequate and unique solution. To this end, an additional constraint, which enforces the consistency of the stored heat at the macro and the micro level is proposed

$$(\rho c_v)_M \theta_M = \frac{1}{V} \int_V (\rho c_v)_m \theta_m dV \quad (4.6)$$

in addition to the macroscopic heat capacity already introduced in eq. (4.3). This condition is sufficient to obtain a unique temperature profile and enforces a temperature distribution that respects the consistency of the stored heat at micro and macro level. It will be referred to as the thermal energy consistency condition in the following sections.

The driving mechanism for heat conduction is the temperature gradient developing in the volume as a result of the boundary conditions. Therefore, an important characteristic of the scale transition between the micro and the macro level is the transfer of temperature gradients. Recalling that the temperature field is additively split in its macro and micro contributions (see eq. (4.4)) the volume averaged micro temperature gradient can be written as

$$\frac{1}{V} \int_V \vec{\nabla}_m \theta_m dV = \vec{\nabla}_M \theta_M + \frac{1}{V} \int_{\Gamma} \theta_f \vec{n} d\Gamma \quad (4.7)$$

where the volume integral involving the fluctuation field is converted into a boundary (Γ) integral with the aid of the Gauss divergence theorem.

The gradient $\vec{\nabla}_M \theta_M$ reflects the thermal effect of the macroscopic heat flow which has to be transferred through the boundary conditions to the RVE. A scale transition relation that enforces the macroscopic temperature gradient to equal the volume average of its microscopic counterpart is therefore introduced. This condition leads to the constraint

$$\int_{\Gamma} \theta_f \vec{n} d\Gamma = \vec{0} \quad (4.8)$$

which can be satisfied by different sets of RVE boundary conditions.

4.4.2 Micro-scale RVE boundary conditions

If the scale transition constraint (4.8) is written explicitly as

$$\int_{\Gamma^L} \{\theta_f^L - \theta_f^R\} \vec{n}^L d\Gamma + \int_{\Gamma^B} \{\theta_f^B - \theta_f^T\} \vec{n}^B d\Gamma = \vec{0} \quad (4.9)$$

it is immediately clear that the sufficient conditions, in terms of macroscopic and microscopic quantities, can be formulated as

$$\theta_m^R - \theta_m^L = \vec{\nabla} \theta_M \cdot (\vec{x}^R - \vec{x}^L) \quad (4.10a)$$

$$\theta_m^T - \theta_m^B = \vec{\nabla} \theta_M \cdot (\vec{x}^T - \vec{x}^B) \quad (4.10b)$$

These are the so-called periodic boundary conditions which naturally result in anti-periodic normal flux boundary conditions

$$q_{m_n}^L = -q_{m_n}^R \quad (4.11a)$$

$$q_{m_n}^T = -q_{m_n}^B \quad (4.11b)$$

according to the heat flux balance. In eq. (4.11) the normal heat flux components over the boundaries, $q_{m_n}^{(L,R,T,B)}$, are defined as

$$q_{m_n}^{(L,R,T,B)} = \vec{q}_m^{(L,R,T,B)} \cdot \vec{n}^{(L,R,T,B)} \quad (4.12)$$

It is trivial that, under steady state conditions the inflowing heat flux should be equal to the outgoing flux.

Based on the macro to micro transition structure, different boundary conditions satisfying eq. (4.8) can be constructed, e.g. $\theta_f = 0$ on Γ for prescribed temperature boundary conditions. Alternatively, it is possible to prescribe flux boundary conditions in terms of the macroscopic heat flux. However, in the sequel of this chapter, periodic boundary conditions will be used, since it is known that they provide the best approximation for a fixed RVE size in a purely mechanical analysis, see e.g. [80]. Note that the periodic boundary conditions have a purely mathematical motivation and therefore do not imply any kind of geometric restrictions on the micro-domain, e.g. geometrically periodic RVE.

4.4.3 The micro-macro scale transition

The second law of thermodynamics leads to Fourier's inequality, in its standard form given by

$$-\frac{1}{\theta} \vec{\nabla} \theta \cdot \vec{q} \geq 0 \quad (4.13)$$

which is essentially the entropy change due to heat conduction. Eliminating the temperature appearing in the denominator (as proposed in [81]) and enforcing the consistency of the entropy change at the macro and the micro level, one can write

$$\frac{1}{V} \int_V \vec{\nabla}_m \theta_m \cdot \vec{q}_m dV = \vec{\nabla}_M \theta_M \cdot \vec{q}_M \quad (4.14)$$

stating that the entropy change due to heat conduction at the macroscopic point level should be consistent with that of the underlying microstructure. Since the scale bridging relation for the temperature gradient is already introduced, according to the equations (4.7) and (4.8), the entropy consistency condition constitutes the basis for linking micro and macro heat flux fields. For the following considerations it is more appropriate to transform the left-hand side of eq. (4.14) according to

$$\frac{1}{V} \int_V \vec{\nabla}_m \theta_m \cdot \vec{q}_m dV = \frac{1}{V} \int_{\Gamma} \theta_m q_{m_n} d\Gamma \quad (4.15)$$

for which the identity $\vec{\nabla}_m \cdot (\theta_m \vec{q}_m) = \vec{\nabla}_m \theta_m \cdot \vec{q}_m$ due to the balance of heat, has been used.

Additionally, to be exploited in the following, the volume averaged microscopic heat flux field can be written as

$$\frac{1}{V} \int_V \vec{q}_m dV = \frac{1}{V} \int_{\Gamma} \vec{x} q_{m_n} d\Gamma \quad (4.16)$$

with the aid of the identity

$$\vec{\nabla}_m \cdot (\vec{x}_m \vec{q}_m) = \vec{\nabla}_m \vec{x}_m \cdot \vec{q}_m + \vec{x}_m (\vec{\nabla}_m \cdot \vec{q}_m) = \vec{q}_m \quad (4.17)$$

which holds in view of the heat balance and the identity $\vec{\nabla}_m \vec{x}_m = \mathbf{I}$. In the case of periodic temperature and the associated anti-periodic normal heat flux boundary conditions, the volume averaged micro entropy change (the right-hand side of eq. (4.15)) can be expressed as

$$\begin{aligned} \frac{1}{V} \int_{\Gamma} \theta_m q_{m_n} d\Gamma &= \\ \frac{1}{V} \vec{\nabla}_M \theta_M \cdot \int_{\Gamma^L} (\vec{x}_L - \vec{x}_R) \vec{q}_m \cdot \vec{n}^L d\Gamma &+ \frac{1}{V} \vec{\nabla}_M \theta_M \cdot \int_{\Gamma^B} (\vec{x}_B - \vec{x}_T) \vec{q}_m \cdot \vec{n}^B d\Gamma = \\ \vec{\nabla}_M \theta_M \cdot \frac{1}{V} \int_{\Gamma} \vec{x} q_{m_n} d\Gamma &= \vec{\nabla}_M \theta_M \cdot \frac{1}{V} \int_V \vec{q}_m dV \end{aligned} \quad (3.18)$$

Comparing eq. (4.18) with eq. (4.14) and eq. (4.15) leads to the identification

$$\frac{1}{V} \int_V \vec{q}_m dV = \vec{q}_M \quad (4.19)$$

showing the equivalence of the volume averaged micro heat flux field and the macroscopic heat flux. If investigated for other boundary conditions, the scale bridging strategy leads to the same consistent result that the macroscopic heat flux is equal to the volume averaged microscopic heat flux field over the RVE domain.

4.5 Two-Scale Numerical Solution Strategy

Once the boundary conditions for the RVE and the constitutive laws for each constituent of the microstructure are defined, the boundary value problem at the micro level can be solved by the finite element method numerically. The 2D RVE problem will be elaborated, where its extension to 3D is relatively straightforward.

4.5.1 RVE boundary value problem

The discretization of the weak form of the microscopic heat balance equation leads to a system of (non-)linear algebraic equations in the unknown nodal temperatures stored in the column $\underline{\theta}$, which can be written as

$$\underline{q}_{int}(\underline{\theta}) = \underline{q}_{ext} \quad (4.20)$$

Eq. (4.20) states that the externally applied nodal heat fluxes are equilibrated by the nodal internal fluxes. The system is excited by the macroscopic loading term $\underline{\Upsilon}_M$, a column consisting of the macroscopic temperature and the components of the macroscopic temperature gradient with respect to the base vectors $\{\vec{e}_1, \vec{e}_2\}$

$$\underline{\Upsilon}_M = \begin{bmatrix} \theta_M \\ (\vec{\nabla}_M \theta_M)_1 \\ (\vec{\nabla}_M \theta_M)_2 \end{bmatrix} \quad (4.21)$$

According to the scale separation adopted, these quantities remain constant at the level of the microscopic problem for a single macroscopic incremental iteration. The temperature column is next decomposed in, $\underline{\theta}_e$, the nodal temperatures at the edge nodes (excluding nodes located at the four corners of the RVE), $\underline{\theta}_i$, internal nodal temperatures (excluding nodes located at the RVE boundaries) and $\underline{\theta}_c$, the nodal temperatures of the corner nodes. The columns \underline{q}_{int} and \underline{q}_{ext} are split up likewise. In case of temperature dependent conductivities at the micro level, the equilibrium solution satisfying eq. (4.20) can be obtained iteratively using a classical Newton-Raphson scheme. To this purpose, the system of equations (4.20) is linearized with respect

to the incremental estimates $\underline{\theta}^k$, which yields the following system for the iterative corrections $\delta\underline{\theta}$

$$\underline{K} \delta\underline{\theta} = \underline{q}_{ext} - \underline{q}_{int}(\underline{\theta}^k) \quad (4.22)$$

where the matrix \underline{K} is defined by

$$\underline{K} = \left. \frac{\partial \underline{q}_{int}}{\partial \underline{\theta}} \right|_{\underline{\theta}^k} \quad (4.23)$$

The resulting system of equations takes the following decomposed format

$$\begin{bmatrix} \underline{K}_{ee} & \underline{K}_{ei} & \underline{K}_{ec} \\ \underline{K}_{ie} & \underline{K}_{ii} & \underline{K}_{ic} \\ \underline{K}_{ce} & \underline{K}_{ci} & \underline{K}_{cc} \end{bmatrix} \begin{bmatrix} \delta\underline{\theta}_e \\ \delta\underline{\theta}_i \\ \delta\underline{\theta}_c \end{bmatrix} = \begin{bmatrix} \underline{q}_e^{ext} \\ \underline{0} \\ \underline{q}_c^{ext} \end{bmatrix} - \begin{bmatrix} \underline{q}_e^{int}(\underline{\theta}^k) \\ \underline{q}_i^{int}(\underline{\theta}^k) \\ \underline{q}_c^{int}(\underline{\theta}^k) \end{bmatrix} \quad (4.24)$$

To proceed further, the column $\underline{\theta}_e$ is subdivided in a first sub-column with the independent values $\underline{\theta}_n$ containing the nodal temperature unknowns of the left and bottom edges and a second sub-column with the dependent degrees of freedom $\underline{\theta}_d$ (i.e. the nodal temperature unknowns of the right and top edges which will be eliminated by a master-slave approach via tying relations). To ease the implementation, the RVE domain is discretized in such a way that the nodes on opposite sides match geometrically. The periodic boundary conditions applied to the edge nodes lead to a set of constraints of a non-homogeneous type which can be expressed as

$$\underline{\theta}_r = \underline{\theta}_l + \underline{C}_{rl} \underline{\Upsilon}_M \quad (4.25a)$$

$$\underline{\theta}_t = \underline{\theta}_b + \underline{C}_{tb} \underline{\Upsilon}_M \quad (4.25b)$$

where \underline{C}_{rl} and \underline{C}_{tb} are the coefficient matrices of the tying relations, resulting from eq. (4.10). Consequently, the edge degrees of freedom $\underline{\theta}_e$ can be expressed as

$$\underline{\theta}_e = \underline{T} \underline{\theta}_n + \underline{G} \underline{\Upsilon}_M \quad (4.26)$$

where the matrices \underline{T} and \underline{G} are implicitly defined through the above relations. Note that periodicity assumption induces that the external nodal heat flux column \underline{q}_e^{ext} on the right-hand side of eq. (4.24) reflects anti-periodicity (see eq. (4.11)). Using this information and the introduced transformation (eq. (4.26)), the equation system (4.24) can be condensed to following form

$$\begin{bmatrix} \underline{T}^T \underline{K}_{ee} \underline{T} & \underline{T}^T \underline{K}_{ei} & \underline{T}^T \underline{K}_{ec} \\ \underline{K}_{ie} \underline{T} & \underline{K}_{ii} & \underline{K}_{ic} \\ \underline{K}_{ce} \underline{T} & \underline{K}_{ci} & \underline{K}_{cc} \end{bmatrix} \begin{bmatrix} \delta\underline{\theta}_n \\ \delta\underline{\theta}_i \\ \delta\underline{\theta}_c \end{bmatrix} = \begin{bmatrix} -\underline{q}_n^{int} - \underline{q}_d^{int} \\ -\underline{q}_i^{int} \\ \underline{q}_c^{ext} - \underline{q}_c^{int} \end{bmatrix} \quad (4.27)$$

\underline{q}_n^{int} and \underline{q}_d^{int} appearing on the right hand side are the corresponding sub-columns of the internal nodal heat flux column of edge nodes introduced as \underline{q}_e^{int} in eq. (4.24). Due

to the structure of the transformation matrix \underline{T}^T and the anti-periodicity condition, the non-zero entries of the column \underline{q}_e^{ext} cancel out and therefore do not appear in equation system (4.27). Note that, variations $\delta\theta_e$, are purely expressed in $\delta\theta_n$ since the variations of the macroscopic quantities, $\delta\underline{\Upsilon}_M$, are zero upon solving the micro problem. Further on, the periodic temperature boundary conditions for the corner nodes lead to three independent equations according to

$$\theta^2 = \theta^1 + (\underline{\Upsilon}_M)_2 l_1 \tag{4.28a}$$

$$\theta^3 = \theta^1 + (\underline{\Upsilon}_M)_2 l_1 + (\underline{\Upsilon}_M)_3 l_2 \tag{4.28b}$$

$$\theta^4 = \theta^1 + (\underline{\Upsilon}_M)_3 l_2 \tag{4.28c}$$

Finally, the equation system is completed by the stored heat consistency condition eq. (4.6), which, upon discretization, can be written as

$$\underline{C}\theta = (\underline{\Upsilon}_M)_1 \tag{4.29}$$

where \underline{C} is the coefficient row corresponding to this constraint. In a variational form, the four equations (eq. (4.28) and eq. (4.29)) can be compactly expressed as

$$\begin{bmatrix} \underline{M}_{ce} & \underline{M}_{ci} & \underline{M}_{cc} \end{bmatrix} \begin{bmatrix} \delta\theta_e \\ \delta\theta_i \\ \delta\theta_c \end{bmatrix} = \begin{bmatrix} \underline{M}_{ce} \underline{T} & \underline{M}_{ci} & \underline{M}_{cc} \end{bmatrix} \begin{bmatrix} \delta\theta_n \\ \delta\theta_i \\ \delta\theta_c \end{bmatrix} = \underline{0} \tag{4.30}$$

where the matrices $\underline{M}_{(ce, ci, cc)}$ contain the coefficients corresponding to this set of constraints. By replacing the last four (corner node) equations in (4.27) by the set of 4 equations (4.30), the resulting system can be solved in a straight forward manner since the right-hand side is known. Using this solution, the column θ is updated followed by a re-evaluation of the internal nodal fluxes. The iterative process is repeated until the right-hand side gets sufficiently small.

4.5.2 Extraction of the macroscopic heat flux

After a microstructural heat conduction analysis has been performed, the macroscopic heat flux vector is extracted through volume averaging. This is done by numerically evaluating the boundary integral in the right hand side of eq. (4.16) which will be further simplified in the following.

With the aid of the anti-periodic heat flux boundary conditions (see eq.(4.11)), eq. (4.16) can be formulated as

$$\vec{q}_M = (\vec{x}_L - \vec{x}_R) \int_{\Gamma_L} q_{m_n}^L d\Gamma + (\vec{x}_B - \vec{x}_T) \int_{\Gamma_B} q_{m_n}^R d\Gamma + \vec{x}_c \underline{q}_c^{ext} \tag{4.31}$$

which, upon discretization and due to thermal equilibrium, takes the following final

form

$$\vec{q}_M = \frac{1}{V} ((\vec{x}_L - \vec{x}_R) \sum \underline{q}_L^{ext} + (\vec{x}_B - \vec{x}_T) \sum \underline{q}_B^{ext} + \vec{x}_c \underline{q}_c^{ext}) \quad (4.32)$$

In eq. (4.32), \underline{q}_L^{ext} and \underline{q}_B^{ext} are the columns of nodal heat fluxes developing at the left and bottom edges, respectively. Using the obtained complete nodal temperature column $\underline{\theta}$ at the micro level, the internal and external nodal heat flux columns can be obtained by simple substitution into eq. (4.20). The summations in eq. (4.32) are to be performed over the components of the corresponding columns. The last term $\vec{x}_c \underline{q}_c^{ext}$ (with \vec{x}_c , a row with corner node position vectors) represents the contribution of the heat fluxes at the corner nodes. Eq. (4.32) can be conveniently expressed in a matrix-column format as

$$\underline{q}_M = [\underline{L}_n \quad \underline{L}_c] \begin{bmatrix} \underline{q}_n^{ext} \\ \underline{q}_c^{ext} \end{bmatrix} \quad (4.33)$$

where \underline{L}_n and \underline{L}_c are implicitly defined. Eq. (4.33) is exploited for the evaluation of the macroscopic heat flux. In the next section, this expression will be used as the point of departure for the calculation of the macroscopic (tangent) conductivity.

4.5.3 Extraction of the macroscopic conductivity

To solve the macroscopic problem, a relation between the variation of the macroscopic heat flux and the variation of the macroscopic temperature gradient in the form

$$\delta \underline{q}_M = \underline{K}_M \delta (\nabla_M \theta_M) \quad (4.34)$$

should be constructed, where \underline{K}_M is the macroscopic (tangent) conductivity at integration point level of the macroscopic discretization. To this end, the variation of the macroscopic heat flux expression in its matrix-column format (eq. (4.33)) is taken:

$$\delta \underline{q}_M = [\underline{L}_n \quad \underline{L}_c] \begin{bmatrix} \delta \underline{q}_n^{ext} \\ \delta \underline{q}_c^{ext} \end{bmatrix} \quad (4.35)$$

Although $\underline{\Upsilon}_M$ was fixed during incremental iterations at the microscopic level, the converged micro equilibrium state can be used to determine the effect of the variations in the macroscopic quantities on the resulting micro heat flux field. Obviously, this step is essential for the determination of the macroscopic conductivity. Therefore, eq. (4.26) is again linearized, but this time with the variation $\delta \Upsilon$ included:

$$\delta \underline{\theta}_e = \underline{T} \delta \underline{\theta}_n + \underline{G} \delta \underline{\Upsilon}_M \quad (4.36)$$

This variation is substituted into eq. (4.24) where the right-hand side vanishes since the conductivity terms in (4.24) are taken in a converged state of the RVE problem.

Condensation of the result, using the anti-periodicity conditions, (eq. (4.11)) reveals

$$\begin{bmatrix} \underline{T}^T \underline{K}_{ee} \underline{T} & \underline{T}^T \underline{K}_{ei} & \underline{T}^T \underline{K}_{ec} \\ \underline{K}_{ie} \underline{T} & \underline{K}_{ii} & \underline{K}_{ic} \\ \underline{K}_{ce} \underline{T} & \underline{K}_{ci} & \underline{K}_{cc} \end{bmatrix} \begin{bmatrix} \delta \underline{\theta}_n \\ \delta \underline{\theta}_i \\ \delta \underline{\theta}_c \end{bmatrix} = - \begin{bmatrix} \underline{T}^T \underline{K}_{ec} \underline{G} \\ \underline{K}_{ie} \underline{G} \\ \underline{K}_{ce} \underline{G} \end{bmatrix} \delta \underline{\Upsilon}_M \quad (4.37)$$

from which, the variations $\delta \underline{q}_n^{ext}$ and $\delta \underline{q}_c^{ext}$ can be extracted as

$$\begin{bmatrix} \delta \underline{q}_n^{ext} \\ \delta \underline{q}_c^{ext} \end{bmatrix} = \begin{bmatrix} -\underline{T}^T \underline{K}_{ec} \underline{G} \\ -\underline{K}_{ce} \underline{G} \end{bmatrix} \delta \underline{\Upsilon}_M \quad (4.38)$$

Using this information in eq. (4.35) finally yields the macroscopic tangent conductivity as

$$\underline{K}_M = (-\underline{L}_n \underline{T}^T \underline{K}_{ec} \underline{G} - \underline{L}_c \underline{K}_{ce} \underline{G}) \quad (4.39)$$

4.5.4 Nested solution strategy

After having examined each of the ingredients of the homogenization scheme separately, the global algorithmic framework is outlined in the following.

The temperature field on the macroscopic domain is spatially discretized by finite elements and in case of transient problems, a proper numerical time integration scheme is introduced to convert the governing differential equations into a fully discrete form. Thermal boundary conditions are parameterized in a (pseudo-)time setting and applied incrementally. For transient cases, the macroscopic problem should be complemented by initial conditions. Assuming that the time discretization is done in a convenient way, the (non-)linear equations resulting from the heat balance have to be solved with an incremental-iterative (if necessary) solution procedure. To incorporate the constitutive behaviour (relating the macroscopic temperature gradient and the macroscopic heat flux), an RVE is attributed to each macroscopic integration point which is subdivided in finite elements.

At the micro level, the macroscopic temperature gradient is used to formulate the boundary conditions to be imposed on the RVE and the macroscopic temperature is supplied to the thermal energy consistency condition rendering the microscopic temperature profile unique. Upon the solution, the macroscopic heat flux vector and the macroscopic conductivity are extracted as outlined in section 4.5 and transferred to the macroscopic level (integration point). In case of transient problems, the macroscopic heat capacity is calculated through volume averaging (eq. (4.3)) and also passed to the macro level.

Upon completing the RVE computations, the macroscopic heat flux vector and the macroscopic heat capacity are available at each integration point and the macroscopic nodal heat balance can be evaluated. If the heat balance is satisfied (within the limits set by a predefined convergence criterion), the next time increment can be computed.

Otherwise, the iterative macroscopic temperature field has to be updated using the macroscopic (tangent) conductivities which are already available in each integration point from the micro level analysis.

The high computational effort can be reduced by parallel computing which has a simple algorithmic structure due to the proposed solution procedure. In a parallel computing framework, the macroscopic mesh (data) is handled by a single master processor and the micro level problems are distributed to the slave processors which receive (RVE input) and send data (RVE output) to the master processor. The slave processors do not need to communicate with each other and therefore the parallel algorithm turns out to be very effective and simple, see [18, 75] for equivalent mechanical problems.

4.6 Two-scale Homogenization Examples

The proposed algorithm is implemented in a commercial finite element software framework (MSC Marc) through user defined material routines. To illustrate the applicability of the proposed method and to emphasize its added value, two examples are worked out in this section.

For both examples the time integration is achieved by the backward-Euler integration scheme.

4.6.1 Thermal homogenization in a cellular foam-like structure

The first problem analyses the temperature evolution through the thickness of a wall, which serves as a separation and fire retardance unit and which is made of a closed-cell aluminium foam. The structural details and boundary conditions are depicted in figure 4.3. Due to the assumed boundary conditions, the macroscopic system can be modeled as a one-dimensional heat conduction problem over the wall thickness of 150 mm. On the outer side of the wall, a convection boundary condition with a film coefficient of $50 \text{ W/m}^2\text{K}$ is used, combined with an ambient temperature $T_0 = 20 \text{ }^\circ\text{C}$. The inner face of the wall is exposed to a final temperature T_F equal to $400 \text{ }^\circ\text{C}$ starting from an initial temperature of $20 \text{ }^\circ\text{C}$. The final temperature level is reached in 1 second and it is kept constant thereafter, see the left-hand side of figure 4.3. A typical strip of the macroscopic domain is discretized by 32 4-noded quadrilateral elements with 4 integration points (total dofs = 66) and a constant time step size of 0.5 is used. The microscopic mesh consists of 652 elements (total dofs = 702).

Aluminium foams have favorable heat isolating and fire retardance properties and are classified by their basic cell geometry. Here, a perfect hexagonal geometry ($h = 1$) is considered, see figure 4.3, with a relative density equal to 0.05, which is essentially the ratio of solid volume with respect to the total cell volume. In reality, three mechanisms of heat transfer (conduction, convection and radiation) take place at the micro

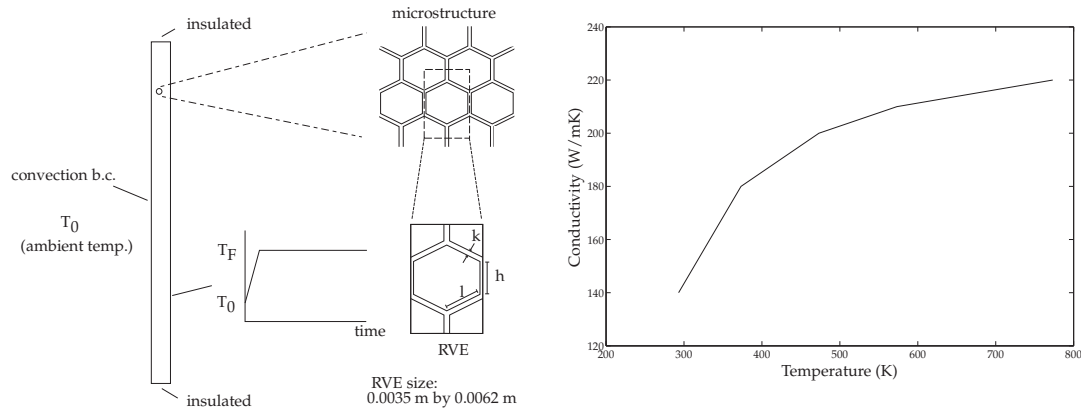


Figure 4.3: Typical hexagonal structure and the representative volume element (i.e. a unit cell) selected

level. For the geometry and the cell type as selected here, the contribution of convection and radiation can be neglected (see [82] for details). Therefore, a hexagonal RVE composed of a solid skeleton and air through which heat can be transferred by conduction only is considered. Both constant and temperature dependent conductivities are considered. For the temperature dependent case, a temperature vs. conductivity relation is given in the right-hand side of figure 4.3, showing an improved conductivity at increasing temperature. In the constant conductivity case, a conductivity of 200 W/mK is taken for the solid skeleton, which is the value corresponding to approximately 200 °C in figure 4.3. For air, the conductivity value is taken as 0.025 W/mK. For the solid skeleton, the density and heat capacity values are taken to be 2700 kg/m³ and 940 J/kgK respectively. For air, the values used are 1.25 kg/m³ and 1005 J/kgK, respectively. Therefore memory effects mentioned in [64] do not appear since the ratio $(c_v)_{\text{air}}/(c_v)_{\text{alum.}}$ is also low, see [64] for the details. For constant conductivity case, the computation time can be reduced extensively since it is sufficient to obtain the homogenized conductivity just once from the analysis of the microstructure under arbitrary loading conditions. Therefore the computational cost for constant conductivity case is comparable with that of a conventional finite element analysis. However, in case of temperature dependent conductivities at the micro level, the computational cost increases considerably, for this particular case approximately 40 hours on a single processor machine for 150 time steps. In figure 4.4, a comparison of temperature profiles at different times, for a constant and for a temperature dependent conductivity is presented. For comparison purposes, the result based on the conductivity obtained from the rule of mixtures (using the constant average conductivity) is also presented. It is clear from figure 4.4 that, the comparison of constant conductivity case and the rule of mixtures results reveals that the rule of mixture solution overestimates the temperature values considerably.

For the constant conductivity case, a good agreement between the macroscopic conductivity obtained here and the one given in reference [83], is obtained. The latter results are based on an analytical approach mainly valid for small k/l (k : thickness of the solid skeleton, see figure 4.3) ratios. However, for larger k/l ratios, the ana-

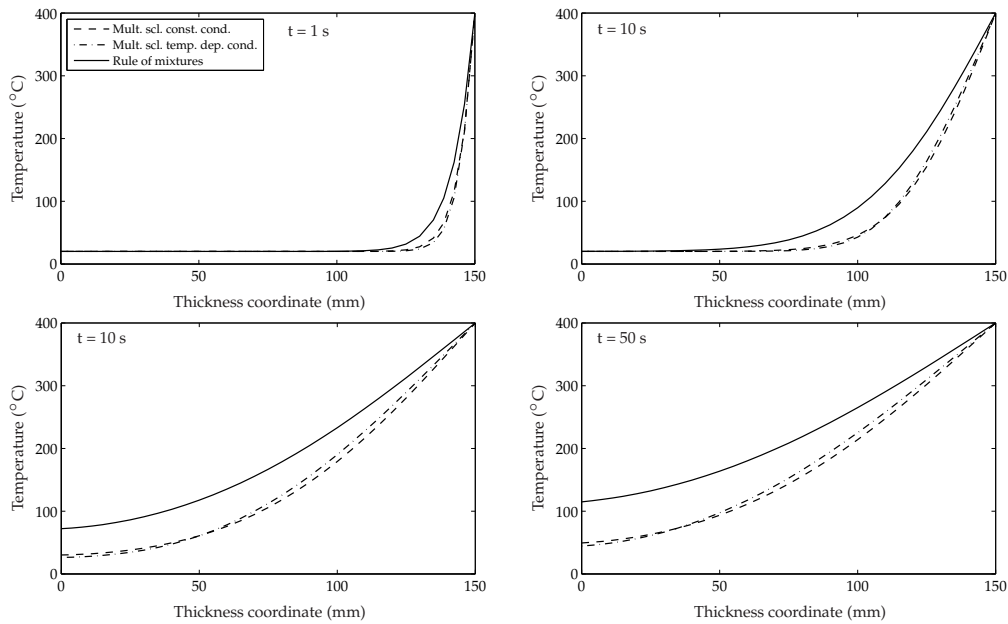


Figure 4.4: Comparison of temperature profiles over the thickness at different times

lytical model (reference [83]) and our findings deviate since the analytical model is based on a one dimensional heat conduction along the solid skeleton parts.

4.6.2 Thermal homogenization in refractory-like materials

The second problem specification is inspired by the furnace linings used in steel production plants. Typically, refractory bricks with a granular microstructure are used for the linings. Due to the production stages and an inherent anisotropic (mechanically and thermally) granular structure, a material microstructure composed of discretely connected (or disconnected) grains with different principal heat conduction directions should be dealt with. Schematically, the rotated coordinate systems, see figure 4.5, represent the anisotropy of each grain of the microstructure. To obtain a better understanding of the effect of the anisotropy, two different cases are considered. In the first case, the scatter of the principal directions between the grains is taken to be small. This reflects a strong texture, where the principal directions of any grain are close to those of the neighboring grains, the difference lying within a range of 10 degrees. In the second case, the principal directions of the grains are taken randomly. Additionally, to make a comparison, the temperature profile is also computed using the conductivities obtained by the rule of mixtures. Further on, to investigate qualitatively the effect of thermo-mechanical damage (i.e. disconnected grains) due to abrupt temperature changes and cycles, a pre-damaged RVE with a diagonal crack (see figure 4.5) is introduced. The domain within the crack is assumed to have the properties of air which are already given in the previous example. The structure is modeled as a two dimensional problem with boundary conditions as in-

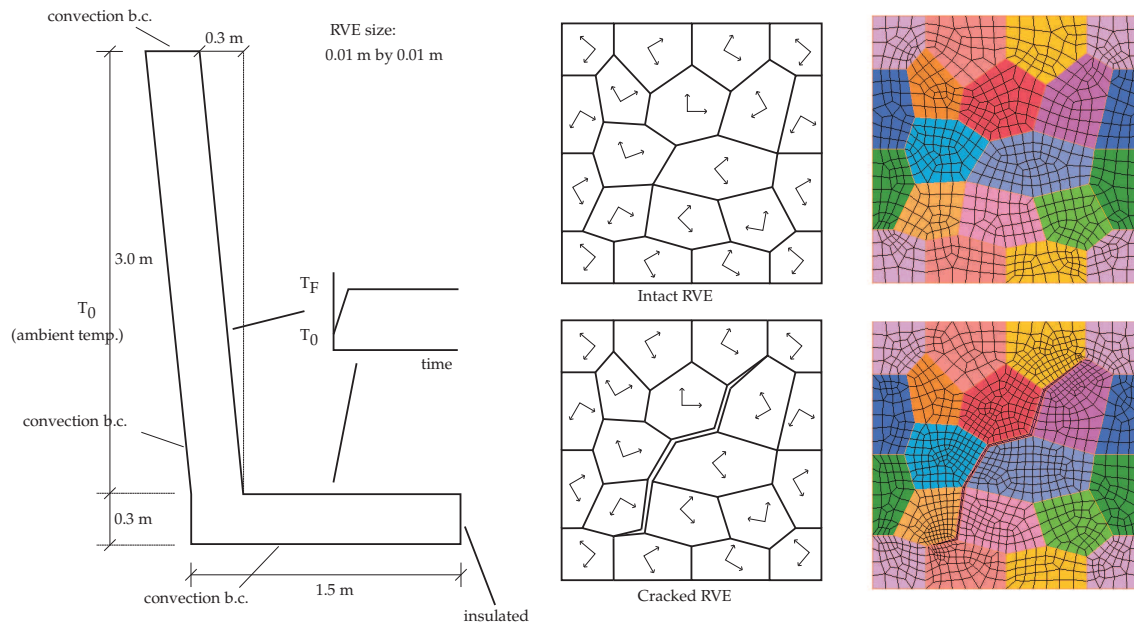


Figure 4.5: Ladle structure and RVE composed of grains with an anisotropic heat conductivity

indicated in figure 4.5. Starting from an initial temperature of 20°C , the inner faces of the structure are exposed to a final temperature of 800°C , reached in 2 seconds and kept constant thereafter. The reference conductivity tensor is taken to be orthotropic with principal values of 38 W/mK and 10 W/mK . The density and heat capacity are taken to be 1820 kg/m^3 and 120 J/kgK , respectively. The macroscopic mesh consists of 3125 4-noded quadrilaterals with 4 integration points (total dofs = 3276) and the micro-domain is divided into 1305 elements with the total dofs number of 1348. As mentioned in the previous example, due to constant conductivities, computation times are comparable with those of the conventional FE analysis. In figure 4.6, the temperature profiles along the cross-section indicated are compared at $t=50\text{ s}$, for small-scatter and random anisotropy. For the small-scatter case (shown left) the results following the rule of mixtures and the computational homogenization are obviously close since the microstructure is more or less homogeneous in terms of its global conductivity. However in the large-scatter case (shown right), the differences are pronounced; where the computational homogenization results reflects the microstructural information more adequately. For both cases, the effect of pre-damage which leads to locally reduced conductivities can clearly be observed in the temperature profiles. Evidently, the rule of mixtures cannot discriminate between these two cases which locally differ up to 100°C . In figure 4.7, the distribution of the temperature and the magnitude of the heat flux at the micro level are shown for $t=2\text{ s}$. The microstructural profiles depicted are taken at a distance of 0.3 m from the top edge of the structure on the inclined wall. Obviously, the temperature distributions become less smooth as scatter and damage are introduced in the microstructure. The crack acts as a barrier for the heat flow and therefore the heat is forced to flow over

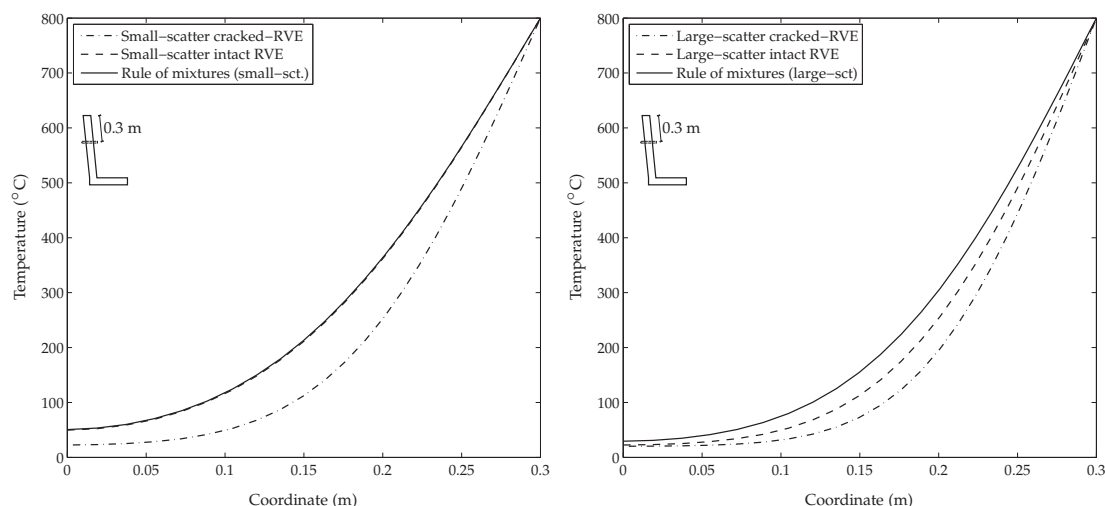


Figure 4.6: Comparison of the temperature distribution for a small-scatter RVE (left) and a large-scatter RVE (right) at the indicated cross-section

the intact narrow top and bottom regions. These microstructural phenomena are particularly important in the case of temperature induced stress fields, as needed in thermo-mechanical damage predictions. The latter is an important issue in assessing thermo-shock damage in refractories.

4.7 Summary and Conclusion

In this contribution, a multi-scale analysis method for the heat conduction in heterogeneous solids is presented. The approach is based on a two level homogenization strategy, which incorporates a rigorous scale transition. The heat conduction problem is treated consistently at two distinct scales which are linked by the outlined scale bridging scheme. The macro to micro transition is achieved through the RVE boundary conditions introduced, whereas the micro to macro transition results from proper averaging relations. The macroscopic (tangent) conductivity is derived in a consistent manner. Finally, a nested finite element solution scheme is presented and implemented into a FE framework. As shown by the example problems, the method offers the possibility to include a microstructural morphology and a temperature dependent microstructural material behavior and transfers the microstructural response properly to the macro level. Original aspects and the added values of the proposed approach are:

- A rigorous method for the heat conduction analysis in heterogeneous solids has been developed. The approach is particularly superior when the coupling

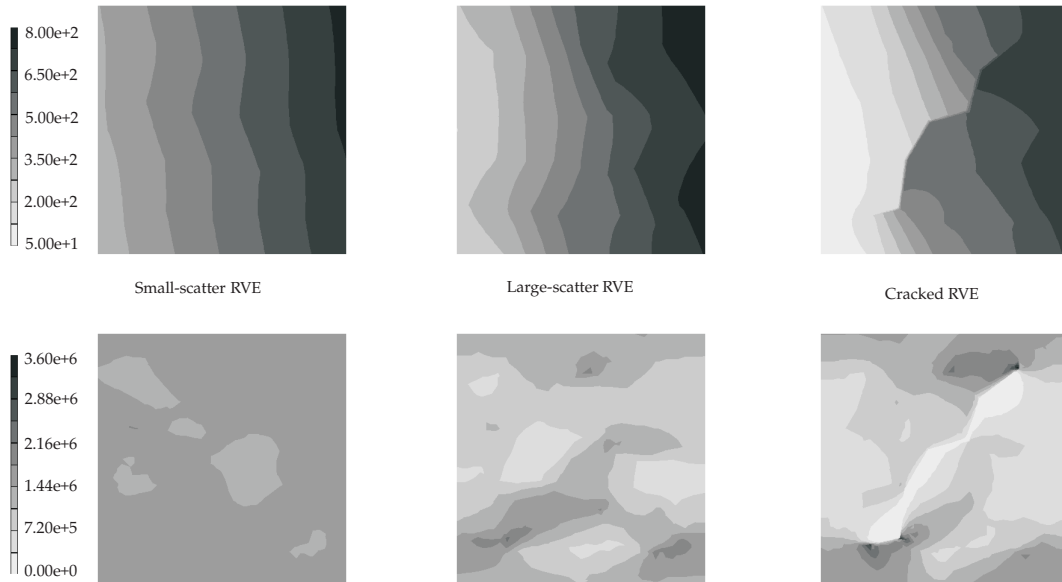


Figure 4.7: Comparison of the temperature fields (in °C) and the magnitude of the heat flux vector (in W/m²) distribution at RVE level (top row, temperatures and bottom row, heat fluxes)

between micro and macro scales becomes stronger, e.g. in case of a temperature sensitive microstructural response or materials with evolving microstructure.

- Anisotropy, nonlinearity and microstructure morphology can be easily introduced and investigated effectively. Particularly, temperature dependent conductivity problems which cannot be handled by classical homogenization techniques, can easily be dealt with.
- The method offers considerable potential for thermo-mechanical damage predictions when combined with mechanical homogenization, with the capability to capture and quantify the interaction between thermal and mechanical fields.
- Results obtained through the proposed methodology may serve as a reference for any other simplified homogenization scheme.

The proposed method, when combined with mechanical homogenization, constitutes a powerful tool, especially at high temperatures where the material properties become strongly dependent on the temperature. The influence of microstructural evolution (e.g. damage and micro-cracking) on the mechanical and thermal fields and their interaction can be introduced and treated effectively. This enhances the understanding and modeling of failure phenomena and opens the possibility to identify some interesting mechanisms of failure initiation and field interaction effects which

cannot be captured and described trivially without incorporating the relevant microstructural details, as done here.

FE² Computational Homogenization for the Thermo-mechanical Analysis of Heterogeneous Solids¹

Abstract

This chapter presents a two-scale thermo-mechanical analysis framework for heterogeneous solids based on a computational homogenization technique. The evolution of the mechanical and thermal fields at the macroscopic level is resolved through the incorporation of the microstructural response. Within the proposed multi-scale approach, the temperature dependent non-linear thermo-mechanical response is accounted by solving a boundary value problem at the micro scale, the results of which are properly averaged and transferred to the macro level in a consistent way. The framework does not require explicitly determined homogenized material properties (e.g. macroscopic thermal expansion coefficients) since no constitutive equations are required for the macroscopic stresses and heat fluxes at the macro level. A nested finite element solution procedure with an operator split implementation is outlined and the effectiveness of the approach is demonstrated by illustrative key examples.

¹Based on: I. Özdemir, W.A.M. Brekelmans, M.G.D. Geers (2008). FE² Computational Homogenization for the Thermo-mechanical Analysis of Heterogeneous Solids. *Computer Methods in Applied Mechanics and Engineering*, **130**(3).

5.1 Introduction

In a wide spectrum of engineering structures and assemblies, premature failure of components is frequently due to severe thermal loading conditions in the form of rapid temperature changes (thermal shocks) and temperature cycles. Variations of the operating temperature of a material is mostly accompanied by physical and geometrical changes at some scale. In heterogeneous systems, local thermal expansion mismatches and thermal anisotropy of different constituents naturally triggers the appearance of internal stresses. Under highly transient external thermal loading conditions, the resulting heterogeneous temperature distribution may lead to a complicated mechanical response and a non-uniform mechanical and physical property degradation accompanied by irreversible geometrical changes. The altered distribution of mechanical properties dictates the macroscopic response as the external mechanical loading is further varied as well. Therefore, a strong coupling between the evolving microstructure and the macroscopic response arises. Moreover, microstructural configurational changes may trigger a significant interaction between the mechanical and thermal fields, for instance, in the form of a reduced heat transfer across a damaged interface. Due to the aforementioned complications, the thermo-mechanical analysis of heterogeneous material systems constitutes a challenging task.

Numerous homogenization techniques have been developed to predict the effective mechanical and thermo-physical properties of materials with complex microstructures. Early research work [60,61] resulted in bounds for the effective material properties which are particularly suitable for relatively simple geometries and a restricted class of constitutive models for the phases. More general asymptotic homogenization approaches were exploited for the determination of the mechanical and thermal constitutive tensors of composites with a periodic microstructure. Starting with the work of Guedes and Kikuchi [66], the use of computational techniques within the homogenization theory has received considerable attention including applications to other field problems [68,71,84,85]. Recently the focus has shifted to extend the theory and solution algorithms to the nonlinear and inelastic range [86–88]. A subclass of computational homogenization techniques which addresses both the influence of the microstructure and the coupling with the resulting macroscopic response is presented in [15–17,74,75]. In this multi-scale approach, the macroscopic material response is obtained from the underlying microstructure by solving a boundary value problem defined on a representative volume element (RVE) of the material. The detailed treatment with underlying principles is described in [18]. At present, this method has been applied successfully for (I) stress and structural damage analysis [17,19,75], (II) the mechanical analysis of structured thin sheets (shells) [20], (III) failure analysis of cohesive interfaces [89] and (IV) heat conduction analysis in heterogeneous solids [90]. In this chapter, the multi-scale framework is extended to the fully coupled thermo-mechanical analysis of heterogeneous material systems including an appropriate solution algorithm.

The interaction of the thermal and mechanical fields within a multi-scale model-

ing framework requires comprehensive treatment and depends on the characteristic micro-failure mechanisms. For typical high temperature resistant materials (e.g. refractory ceramics), micro-failure mechanisms such as debonding of the grain-grain interfaces, evolve at an apparent microstructural level, which motivates a two-level treatment as adopted in the following sections. Furthermore, damage and failure at the micro level takes place without significant inelasticity (e.g. plasticity), which implies that the effect of mechanical energy dissipation on the thermal field is negligible and therefore not taken into account in the analysis. Similarly, the reduction of the heat flow as a result of mechanical damage is not explicitly considered although the constructed framework can easily accommodate such coupling effects. Before proceeding further, the essential points on which the proposed framework differs from the existing approaches can be summarized as:

- The proposed approach does not require macroscopic material properties such as the homogenized coefficient of thermal expansion as opposed to other alternative homogenization schemes.
- The framework has the flexibility to include a non-linear and temperature dependent thermo-mechanical material response at the microstructural level, which is transmitted to the macro level in a consistent way. Furthermore, for different combinations and types of constitutive equations at the micro level, re-derivation of certain effective quantities (expressions) is not necessary.
- The presented solution algorithm resolves the interaction of the fields in a proper way and can accommodate thermo-mechanically induced coupling mechanisms accompanying microstructural evolution.

The presentation of the chapter is organized as follows. After the introduction of the assumptions in the next section, the thermo-mechanical analysis problems at micro and macro levels are formulated in section 5.3. Then, the scale transition structure is summarized in section 5.4. Thereupon, a two-scale solution strategy is presented which leads to an operator-split nested finite element solution algorithm further detailed in section 5.5. Illustrative examples are presented in section 5.6, followed by the discussion and conclusion section.

5.2 Preliminaries

In this chapter, a first order theory is adopted for both the mechanical and thermal homogenization procedure which hinges on the principle of scale separation [17, 75, 90]. A first order theory for mechanical homogenization implies that the macroscopic deformation gradient varies mildly and therefore deformation localization (softening) is excluded from the considerations. However, for typical high temperature resistant structures, the onset of softening is practically the end of service life (failure) since after the onset the bearing capacity is very limited. Theoretically,

the principle of scale separation assumes an infinitesimally small underlying fine scale structure (infinitesimal neighbourhood of a material point) though finite sized RVE's are used in real predictive computations. As a matter of fact, at the micro level, it is assumed that a steady-state temperature profile is attained instantaneously in virtue of the negligibly small size of the RVE. As will be clarified in section 5.5, the RVE analysis is performed to extract macroscopic stresses, heat fluxes and associated tangent operators. Therefore, the RVE analysis can be partly considered as a substitute for the so-called 'algorithmic stress update boxes' (stress integration algorithms) derived from phenomenological models for which the body forces and heat sources are irrelevant [91]. Furthermore, for stationary mechanical loading, inertia effects are neglected.

5.3 Micro and Macro-scale Problem Formulations

5.3.1 Micro-scale problem

The evolution of thermal and mechanical fields at the micro level is defined and monitored on a representative volume element (RVE) provided with the essential physical and geometrical information about the microstructural components. Particularly for materials with random microstructures, the choice of the RVE is a delicate task. The difficulty arises due to the fact that RVE should be statistically representative of all microstructural heterogeneities and at the same time remain small enough so that the principle of scale separation is not violated. Furthermore the RVE response should be independent of the applied boundary conditions. A detailed discussion and relevant techniques to determine the RVE size is given in [92, 93] and the references therein. Here, it is assumed that an appropriate RVE has already been selected. In figure 5.1, the reference and current configuration of a microstructured 2-D domain is shown where the subscript '0' is used for referential quantities. For a particular material point P, the underlying 2-D initially square RVE is depicted in both configurations, for which V and Γ are the current volume and boundary of the micro-domain, respectively. The RVE boundary is further split up into Γ^L for the left side of the boundary, Γ^R for the right, etc. The thermal and mechanical characterizations of the phases at the RVE level are described by their respective constitutive relations. Note that there are no a priori restrictions on the specification of the constitutive laws and material parameters (e.g. temperature dependent, anisotropic, etc.) other than the fundamental thermodynamical limitations.

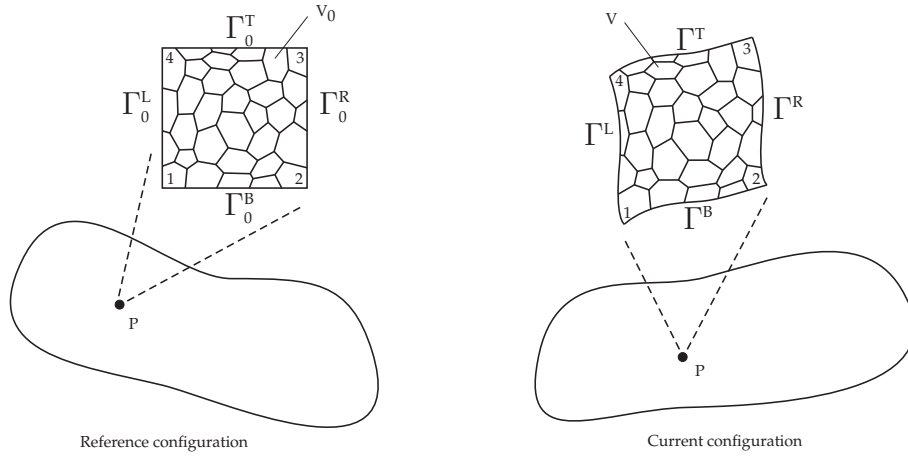


Figure 5.1: Macroscopic and microstructural domain

In a geometrically non-linear setting, in the absence of body forces and inertia effects, the mechanical equilibrium at the micro domain takes the form,

$$\vec{\nabla}_m \cdot \boldsymbol{\sigma}_m = \vec{0} \quad (5.1)$$

in which $\boldsymbol{\sigma}_m$ is the microscopic Cauchy stress tensor defined by the corresponding constitutive law whose description might be anisotropic and depending on the temperature and a set of internal variables. In (5.1), $\vec{\nabla}_m$ indicates the gradient operator with respect to the current micro-domain. The mechanical RVE problem is complemented with standard boundary conditions, for which periodic boundary conditions provide the best approximation [80]. Based on the assumptions introduced in section 5.2, the steady-state heat balance at the micro level is expressed as,

$$\vec{\nabla}_m \cdot \vec{q}_m = 0 \quad (5.2)$$

where \vec{q}_m is the microscopic heat flux vector. To construct a well-posed problem, the balance equation is to be complemented with the temperature and heat flux boundary conditions. The specific form of the boundary conditions will be outlined in section 5.4.

5.3.2 Macro-scale problem

At the macro level, the mechanical equilibrium has an identical structure as at the micro level

$$\vec{\nabla}_M \cdot \boldsymbol{\sigma}_M = \vec{0} \quad (5.3)$$

which is complemented by the macroscopic mechanical boundary conditions. In the absence of heat sources, the conservation of thermal energy equation at the macro

level takes the general time dependent form according to,

$$(\rho c_v)_M \dot{\theta}_M + \vec{\nabla}_M \cdot \vec{q}_M = 0 \quad (5.4)$$

where θ_M , \vec{q}_M and $(\rho c_v)_M$ represent the temperature, the heat flux and the heat storage capacity, respectively. In addition to proper thermal boundary conditions, also initial conditions have to be specified for the temperature distribution at the macro level.

Within the proposed computational homogenization procedure, the macroscopic Cauchy stress and the macroscopic heat flux are obtained from the solution of the micro-scale thermo-mechanical problem defined on the underlying microstructure (RVE). In addition to these flux quantities, the discretized weak forms of the macroscopic governing equations require the macroscopic (tangent) conductivity, the macroscopic mechanical tangent stiffness and the macroscopic heat storage capacity $(\rho c_v)_M$ to enable the solution of the resulting system of equations. Consistent derivations of these macroscopic quantities are elaborated in the following sections.

5.4 Scale transitions

5.4.1 The macro-micro scale transition

Within the framework of a first order multi-scale analysis, the actual microscopic displacement and temperature fields at a location \vec{x} in the current configuration can be decomposed without loss of generality as,

$$\vec{u}_m(\vec{x}) = (\mathbf{F}_M - \mathbf{I}) \cdot (\vec{X} - \vec{X}_1) + \vec{u}_f(\vec{x}) \quad (5.5a)$$

$$\theta_m(\vec{x}) = \theta_m^1 + \vec{\nabla}_M \theta_M \cdot (\vec{x} - \vec{x}_1) + \theta_f(\vec{x}) \quad (5.5b)$$

in a macroscopic contribution and a fluctuation field (subscript 'f') that represents the fine scale deviations with respect to the average fields as a result of the variations in material properties within the RVE. In equations (5.5), the displacement \vec{u}_m and the temperature θ_m are presented with respect to the corresponding values of corner 1. In equation (5.5a), \vec{X} denotes the position vector in the reference configuration, whereas in equation (5.5b) the current position vector, \vec{x} , is used implying that two different configurations are involved for the decomposition of displacement and temperature fields, respectively. For equation (5.5a), although other referential or spatial kinematic quantities could be used, the description in terms of \mathbf{F}_M and referential position vectors leads to compact scale transition relations, [18]. For the decomposition (5.5b), a formulation based on the current configuration is preferred since a fully referential description requires pull-back of the primary quantities (temperature gradient and heat fluxes) leading to more complicated scale bridging relations. To suppress the rigid body translation, corner 1 is taken to be fixed, $\vec{u}_f(\vec{x}_1) = \vec{0}$,

whereas the rigid body rotation is excluded by the periodic displacement constraint introduced further on. However, fixing the temperature level for the RVE is less trivial. The temperature profile at the micro level results from the imposed boundary conditions and the distinct conductivities of the microstructural phases, which may be temperature dependent. Therefore, the determination of the reference temperature in the micro-domain which has been indicated by θ_m^r is required for a reliable solution. To this end, an additional constraint,

$$(\rho c_v)_M \theta_M = \frac{1}{V} \int_V (\rho c_v)_m \theta_m dV \quad (5.6)$$

is proposed. This condition is sufficient to obtain a unique temperature profile and enforces a temperature distribution that respects the consistency of the stored heat at micro and macro level.

In computational homogenization, the macro-to-micro transition is achieved by enforcing the conditions,

$$\mathbf{F}_M = \frac{1}{V_0} \int_{V_0} \mathbf{F}_m dV_0 \quad (5.7a)$$

$$\vec{\nabla}_M \theta_M = \frac{1}{V} \int_V \vec{\nabla}_m \theta_m dV \quad (5.7b)$$

which essentially imposes a volumetric averaging of the primary deformation characteristics (\mathbf{F} , deformation gradient) and the essential driving forces for the heat flow ($\vec{\nabla}\theta$, temperature gradient), bridging the two scales.

The substitution of equations (5.5) into the scale transition relations equations (5.7) leads to the conditions,

$$\int_{\Gamma_0} \vec{u}_f d\Gamma_0 = \vec{0} \quad (5.8a)$$

$$\int_{\Gamma} \theta_f d\Gamma = 0 \quad (5.8b)$$

which are the basis for different types of boundary conditions that can be imposed at the micro level. For instance, enforcing periodic fluctuation fields results in

$$\vec{u}_f^L = \vec{u}_f^R \rightarrow \vec{u}_R = \vec{u}_L + (\mathbf{F}_M - \mathbf{I}) \cdot (\vec{X}_R - \vec{X}_L) \quad (5.9a)$$

$$\vec{u}_f^T = \vec{u}_f^B \rightarrow \vec{u}_T = \vec{u}_B + (\mathbf{F}_M - \mathbf{I}) \cdot (\vec{X}_T - \vec{X}_B) \quad (5.9b)$$

$$\theta_f^L = \theta_f^R \rightarrow \theta_R = \theta_L + \vec{\nabla}_M \theta_M \cdot (\vec{x}_R - \vec{x}_L) \quad (5.9c)$$

$$\theta_f^T = \theta_f^B \rightarrow \theta_T = \theta_B + \vec{\nabla}_M \theta_M \cdot (\vec{x}_T - \vec{x}_B) \quad (5.9d)$$

which are known to yield better convergence to apparent macroscopic properties as compared to other options (e.g., fully prescribed boundary conditions: $\vec{u}_f = \vec{0}$ and $\theta_f = 0$ on Γ), see [80]. Periodically micro-fluctuating temperature boundary

conditions result in non-homogenous linear relations between the temperatures of the opposite edges which are similar to the constraints arising in second order computational homogenization [94]. Therefore, the stored heat consistency condition (equation (5.6)) and the periodically micro-fluctuating temperature boundary conditions lead to a time-independent (steady-state) temperature profile dictated by the macroscopic temperature, macroscopic temperature gradient and local conductivities within the RVE. However, it is important to note that the macroscopic temperature and the temperature gradient changes as the macroscopic loading is further varied. Therefore, the ‘steady-state’ problem is driven by some non-stationary macroscopic quantities and ‘time-independency’ is just to emphasize that the microscopic temperature profile does not evolve as long as the macroscopic loading is kept at the same level. It is worth to note that the current geometry of the RVE influences the thermo-mechanical response through the imposition of the boundary conditions in the current state, equations (5.9c) and (5.9d). Furthermore, particularly in the vicinity of macroscopic Dirichlet boundary conditions, the temperature gradient can vary rapidly so that the principle of scale separation might be violated. In other words, the variation of the macroscopic temperature profile should be mild enough as compared to the RVE dimensions so that the macroscopic temperature gradient can be taken as constant over an RVE area. This is a limitation of the proposed method. Due to the different configurations employed, referential and current volume integrals are used in equations (5.7a) and (5.7b) from which boundary integrals (5.8a) and (5.8b) are obtained, respectively.

5.4.2 The micro-macro scale transition

For the determination of the macroscopic heat storage capacity $(\rho c_v)_M$, used in equation (5.4), the following volume averaging is proposed

$$(\rho c_v)_M = \frac{1}{V} \int_V (\rho c_v)_m dV \quad (5.10)$$

which is fully in line with the equivalent result obtained through an asymptotic homogenization method [64]. This equation implies that the heat capacity is consistently preserved upon scale bridging.

The micro-to-macro transition is essentially based on two principles. The mechanical coupling hinges on the macro-homogeneity (Hill-Mandel) condition, written in terms of the work conjugate pair \mathbf{F} (deformation gradient tensor) and \mathbf{P} (1st Piola-Kirchhoff stress tensor) as,

$$\mathbf{P}_M : \delta \mathbf{F}_M = \frac{1}{V_0} \int_{V_0} \mathbf{P}_m : \delta \mathbf{F}_m dV_0 \quad (5.11)$$

The symbol ‘:’ indicates the double contraction and for second order tensors yields, $\mathbf{A} : \mathbf{B} = A_{ij} B_{ij}$. This principle simply expresses the volumetric consistency of the

macroscopic internal virtual work and that of the underlying microstructural volume.

For the thermal part, the motivation originates from the 2nd law of thermodynamics, which requires a positive entropy change due to heat conduction. Enforcing the volumetric consistency of the micro and macro entropy increase due to heat conduction leads to,

$$\vec{\nabla}_M \theta_M \cdot \vec{q}_M = \frac{1}{V} \int_V \vec{\nabla}_m \theta_m \cdot \vec{q}_m dV \quad (5.12)$$

which is the basis for the micro-to-macro transition in the context of the conservation of thermal energy. Note that equation (5.12) is not exactly the entropy statement (no temperature scaling applied), but is nevertheless well motivated, see [81].

It can be shown that for each of the boundary conditions of interest, the scale bridging principles lead to [18,90],

$$\mathbf{P}_M = \frac{1}{V_0} \int_{V_0} \mathbf{P}_m dV_0 \quad (5.13a)$$

$$\vec{q}_M = \frac{1}{V} \int_V \vec{q}_m dV \quad (5.13b)$$

From equation (5.13a) the macroscopic Cauchy stresses are obtained by the standard relation $\boldsymbol{\sigma}_M = \frac{1}{\det \mathbf{F}_M} \mathbf{P}_M \cdot \mathbf{F}_M^T$, where \mathbf{F}_M^T is the transpose of \mathbf{F}_M .

5.5 Two-scale Numerical Solution Framework

Since analytical solutions are limited to relatively simple geometries and constitutive relations, a general approximate solution procedure is pursued on the basis of the finite element method at both scales (FE²). Both mechanical and thermal boundary conditions are parameterized in a (pseudo-)time setting and applied incrementally. Furthermore, in case of transient thermal problems, a proper numerical time integration scheme is introduced to convert the spatially discretized rate equations into a fully discrete form. Non-linear equations resulting from the mechanical and heat balances have to be solved with an incremental-iterative solution procedure. To incorporate the constitutive behaviour at the macro level, an RVE is associated to each macroscopic integration point.

The interaction between the mechanical and thermal fields through the temperature induced stresses, temperature dependent material properties and the influence of geometrical changes (large displacements and internal discontinuities) on the thermal field leads to a coupled problem at both micro and macro levels.

The implementation of the coupling between both fields is based on an operator-split approach in which two sub-problems are solved sequentially leading to two incre-

mentally uncoupled balance equations. For this purpose, a thermal balance with an updated and frozen mechanical field is solved, followed by a mechanical equilibrium problem with an updated and frozen thermal field. The resulting numerical scheme has a simple structure with symmetric system matrices but is only conditionally stable. Since an incremental-iterative solution scheme already requires small time steps to handle the nonlinearities, the operator-split approach does not necessarily involve higher computational costs.

In the following sections, the macroscopic boundary value problem (BVP) and the microscopic BVP are further elaborated within the aforementioned framework.

5.5.1 Macroscopic boundary value problem

As a result of geometrical and/or material nonlinearities, the resulting balance equations are non-linear as well and have to be solved by a Newton-Raphson technique in an incremental-iterative way. In the current increment, at iteration k , estimates are denoted as $\underline{u}^{(k)}$ for the nodal displacements and $\underline{\theta}^{(k)}$ for the nodal temperatures, where a bar under a symbol is used to indicate columns (representation of vectors with respect to a certain basis in matrix notation) and matrices. Upon linearization, the out-of-balance (residual) nodal forces and heat fluxes have to vanish, i.e.

$$\underline{r}_{mech}(\underline{u}^{(k)}) = \underline{f}_{int}(\underline{u}^{(k)}) - \underline{f}_{ext} \rightarrow \underline{r}_{mech}(\underline{u}^{(k)}) + \delta\underline{r}_{mech} = \underline{0} \quad (5.14a)$$

$$\underline{r}_{th}(\underline{\theta}^{(k)}) = \underline{q}_{int}(\underline{\theta}^{(k)}) - \underline{q}_{ext} \rightarrow \underline{r}_{th}(\underline{\theta}^{(k)}) + \delta\underline{r}_{th} = \underline{0} \quad (5.14b)$$

where $\delta\underline{r}_{th}$ and $\delta\underline{r}_{mech}$ are the iterative updates of the nodal heat fluxes and forces which tend to zero within the limit of the adopted convergence norm. Using an updated Lagrangian framework (whereby the current configuration is taken as the reference for volume integration, [95]), the corrections $\delta\underline{r}_{th}$ and $\delta\underline{r}_{mech}$ are expressed in the nodal variations $\delta\underline{u}$ and $\delta\underline{\theta}$ as

$$\delta\underline{r}_{mech} = \sum_{e=1}^{n_{el}} \left[\int_{V^e} (\underline{B}^T \underline{C}_M \underline{B} + \underline{H}^T \underline{S} \underline{H}) dV \right] \delta\underline{u} \quad (5.15a)$$

$$\delta\underline{r}_{th} = \sum_{e=1}^{n_{el}} \left[\int_{V^e} \left(\frac{1}{\Delta t} (\rho c_v)_M \underline{N}^T \underline{N} + \underline{B}^T \underline{K}_M \underline{B} \right) dV \right] \delta\underline{\theta} \quad (5.15b)$$

A backward Euler time integration scheme is employed to construct the fully discrete system of equations (5.15b). The key ingredients of these equation systems (equations (5.15a) and (5.15b)) are the macroscopic spatial material tangent stiffness in Voigt notation \underline{C}_M , the macroscopic heat storage capacity $(\rho c_v)_M$ and the macroscopic tangent conductivity \underline{K}_M , respectively. In a standard manner, spatial derivatives of the shape functions are placed in matrix \underline{B} and the matrix \underline{N} is composed of the shape functions. Furthermore, the second term in the integrand of (5.15a) is the so called initial stress component of the tangent stiffness for which \underline{H} and \underline{S} are

defined as,

$$\underline{H} = \begin{bmatrix} N_{1,x} & 0 & N_{2,x} & 0 & \cdots \\ N_{1,y} & 0 & N_{2,y} & 0 & \cdots \\ 0 & N_{1,x} & 0 & N_{2,x} & \cdots \\ 0 & N_{1,y} & 0 & N_{2,y} & \cdots \end{bmatrix} \text{ and } \underline{S} = \begin{bmatrix} \underline{\sigma}_M & \underline{0} \\ \underline{0} & \underline{\sigma}_M \end{bmatrix} \text{ with } \underline{\sigma}_M = \begin{bmatrix} \sigma_{11} & \sigma_{12} \\ \sigma_{21} & \sigma_{22} \end{bmatrix} \quad (5.16)$$

for a two dimensional discretization [96], where $\underline{\sigma}_M$ is the macroscopic Cauchy stress matrix.

The solution algorithm for time step $[t_n \text{ to } t_{n+1}]$ is depicted in table 5.1 (the symbols are defined in the following sub-sections). At the macro level, each increment consists of a ‘thermal pass’ and a ‘mechanical pass’ for which the heat fluxes, stresses and relevant tangent operators are extracted from the RVE level problem. In the following sections, essential components of the multi-scale solution scheme will be explained in more detail. The high computational cost of this scheme can be reduced substantially by parallel computing. Although an implicit solution algorithm is presented here, explicit time marching which requires much smaller time steps, could be equally used. However, this wouldn’t bring considerable gain since the computational burden is on the solution of RVE level problem but not on the extraction of macroscopic tangent stiffnesses and the solution of the macroscopic systems.

It is worth to note that a staggered approach with a proper bookkeeping allows the use of different time stepping for mechanical and thermal problems. This might be particularly useful in case of Dirichlet type thermal boundary conditions at the beginning of the loading history.

5.5.2 RVE level boundary value problem

Essential components of the macroscopic solution procedure (fluxes and tangent operators) require the solution of the micro level BVP’s for both macroscopic thermal and mechanical passes. Similar to the macro level BVP, a finite element solution procedure is adopted for the micro BVP’s including the extraction of the macroscopic heat fluxes, stresses and tangent operators.

RVE-BVP coupled to the macroscopic thermal pass

This section is essentially based on the computational homogenization scheme introduced in [90]. Related details are therefore not given here.

On an updated micro-domain (RVE at t_n passed to micro level in the macroscopic thermal pass, see table 5.1), the discretization of the weak form of the microscopic heat balance equation leads to a system of (non)-linear algebraic equations in the unknown nodal temperatures $\underline{\theta}$, which can be written as,

$$\underline{q}_{int}(\underline{\theta}) = \underline{q}_{ext} \quad (5.17)$$

Table 5.1: Two scale staggered solution scheme for the thermo-mechanical analysis

MACRO		MICRO
Next increment		
I. Thermal pass :		
(a) Next iteration		
<ul style="list-style-type: none"> ▷ assemble the tangent conductivity ▷ solve the system and update θ_M ▷ loop over all integration points 	$\xrightarrow{\theta_M, \vec{\nabla}_M \theta_M}$ $\text{RVE at } t_n$	<ul style="list-style-type: none"> ▷ solve the RVE problem ▷ calculate macroscopic heat flux and conductivity
	$\xleftarrow{\vec{q}_M, K_M}$	
<ul style="list-style-type: none"> ▷ store \vec{q}_M and K_M ▷ end integration point loop ▷ assemble the internal nodal fluxes ▷ check for convergence, if not repeat step (a), else continue 		
II. Mechanical pass :		
(b) Next iteration		
<ul style="list-style-type: none"> ▷ assemble the tangent stiffness ▷ solve the system and update \mathbf{F}_M ▷ loop over all integration points 	$\xrightarrow{\Delta \mathbf{F}_M, \theta_M, \vec{\nabla}_M \theta_M}$ $\text{RVE at } t_n$	<ul style="list-style-type: none"> ▷ solve the RVE problem ▷ calculate the macroscopic stresses and stiffness tensor (\mathbb{A}_M)
	$\xleftarrow{\sigma_M, \mathbb{A}_M}$ updated RVE state	
<ul style="list-style-type: none"> ▷ store σ_M and \mathbb{A}_M ▷ end integration point loop ▷ assemble the internal forces ▷ check for convergence, if not repeat step (b), else save updated RVE state at t_{n+1} and start new increment 		

expressing that the externally applied nodal heat fluxes are equilibrated by the nodal internal fluxes. The system is excited by the macroscopic loading term $\underline{\Upsilon}_M$, a column consisting of the macroscopic temperature and the components of the macroscopic temperature gradient with respect to the base vectors \vec{e}_1, \vec{e}_2

$$\underline{\Upsilon}_M = \begin{bmatrix} \theta_M \\ (\vec{\nabla} \theta_M)_1 \\ (\vec{\nabla} \theta_M)_2 \end{bmatrix} \quad (5.18)$$

which is imposed on the system through the periodically micro-fluctuating temperature boundary conditions (see equations (5.9c), (5.9d)) and the stored heat consis-

tency condition (see equation (5.6)). In case of temperature dependent conductivities at the micro level, the equilibrium solution can be obtained iteratively using a classical Newton-Raphson scheme. To this purpose, equation (5.17) is linearized with respect to the incremental estimates $\underline{\theta}^k$, which yields the following system for the iterative corrections $\delta\underline{\theta}$

$$\underline{K}\delta\underline{\theta} = \underline{q}_{ext} - \underline{q}_{int}(\underline{\theta}^k) \quad (5.19)$$

where the tangent conductivity matrix \underline{K} is defined by $\underline{K} = \frac{\partial \underline{q}_{int}}{\partial \underline{\theta}} \big|_{\underline{\theta}^k}$.

In order to impose the periodically micro-fluctuating temperature boundary conditions, linear dependencies are introduced in the system in a classical manner. To ease the implementation, the RVE domain is discretized in such a way that the nodes on opposite sides match geometrically, see figure 5.2. The periodically micro-fluctuating boundary conditions applied to the edge nodes ($\underline{\theta}_e$, excluding the corner nodes) lead to a set of linear constraint equations of a non-homogeneous type which can be expressed as,

$$\underline{\theta}_e = \underline{T}\underline{\theta}_n + \underline{G}\underline{\Upsilon}_M \quad (5.20)$$

where \underline{T} and \underline{G} are the coefficient matrices of the tying relations and $\underline{\theta}_n$ is the column with the independent (master) degrees of freedom (left and bottom edges, excluding corner nodes). With the introduced transformation, the explicit form of the partitioned system of equations is given as,

$$\begin{bmatrix} \underline{T}^T \underline{K}_{ee} \underline{T} & \underline{T}^T \underline{K}_{ei} & \underline{T}^T \underline{K}_{ec} \\ \underline{K}_{ie} \underline{T} & \underline{K}_{ii} & \underline{K}_{ic} \\ \underline{K}_{ce} \underline{T} & \underline{K}_{ci} & \underline{K}_{cc} \end{bmatrix} \begin{bmatrix} \delta\underline{\theta}_n \\ \delta\underline{\theta}_i \\ \delta\underline{\theta}_c \end{bmatrix} = \begin{bmatrix} -\underline{q}_n^{int} - \underline{q}_d^{int} \\ -\underline{q}_i^{int} \\ \underline{q}_c^{ext} - \underline{q}_c^{int} \end{bmatrix} \quad (5.21)$$

where \underline{q}_n^{int} (independent, left and bottom edges) and \underline{q}_d^{int} (dependent, right and top edges) appearing on the right hand side are the corresponding sub-columns of the internal nodal heat flux column of edge nodes. In equation (5.21) the subscript 'i' refers to the internal (not located on the boundaries) degrees of freedom and subscript 'c' designates the quantities associated with corner nodes, see figure 5.2.

Further on, the periodically micro-fluctuating temperature boundary conditions for the corner nodes (e.g. $\theta_2 = \theta_1 + \vec{\nabla}_M \theta_M \cdot (\vec{x}_2 - \vec{x}_1)$) and the stored heat consistency condition (equation (5.6)) lead to four independent equations which can be compactly expressed in a variational (incremental or iterative) form as,

$$\begin{bmatrix} \underline{M}_{ce} & \underline{M}_{ci} & \underline{M}_{cc} \end{bmatrix} \begin{bmatrix} \delta\underline{\theta}_e \\ \delta\underline{\theta}_i \\ \delta\underline{\theta}_c \end{bmatrix} = \begin{bmatrix} \underline{M}_{ce} \underline{T} & \underline{M}_{ci} & \underline{M}_{cc} \end{bmatrix} \begin{bmatrix} \delta\underline{\theta}_n \\ \delta\underline{\theta}_i \\ \delta\underline{\theta}_c \end{bmatrix} = \underline{0} \quad (5.22)$$

where $\underline{M}_{(ce, ci, cc)}$ are the coefficient matrices. Using these constraints, the resulting system of equations can be solved and an update for the unknown temperature column $\underline{\theta}$ is obtained, [90].

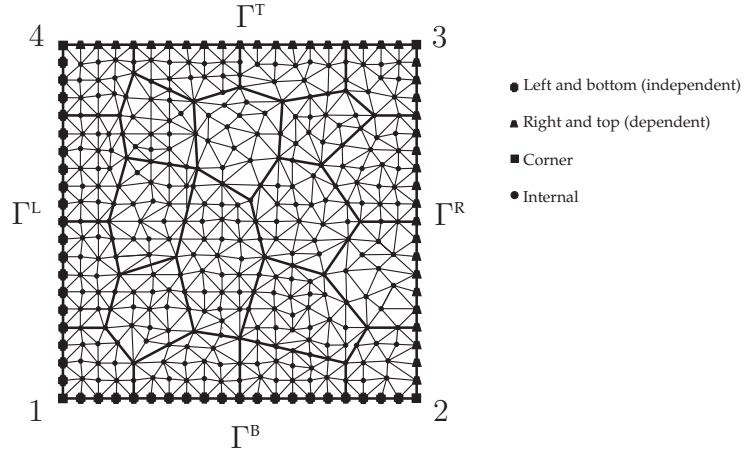


Figure 5.2: Discretized RVE example

Extraction of the macroscopic heat flux

As shown in reference [90], after discretization, the volume averaging relation for \vec{q}_M can be expressed as,

$$\vec{q}_M = \frac{1}{V} \left((\vec{x}_L - \vec{x}_R) \sum \underline{q}_L^{ext} + (\vec{x}_B - \vec{x}_T) \sum \underline{q}_B^{ext} + \vec{x}_c^T \underline{q}_c^{ext} \right) \quad (5.23)$$

where, \underline{q}_L^{ext} and \underline{q}_B^{ext} are the columns of nodal heat fluxes at the left and bottom edges, respectively. The summations are performed over the components of the corresponding columns. The last term $\vec{x}_c^T \underline{q}_c^{ext}$ (with \vec{x}_c , a column with corner node position vectors) represents the contribution of the heat fluxes at the corner nodes. Eq.(5.23) can be conveniently expressed in components using a matrix-column format as,

$$\underline{q}_M = \begin{bmatrix} \underline{L}_n & \underline{L}_c \end{bmatrix} \begin{bmatrix} \underline{q}_n^{ext} \\ \underline{q}_c^{ext} \end{bmatrix} \quad (5.24)$$

where \underline{L}_n and \underline{L}_c are implicitly defined.

Extraction of the macroscopic conductivity

To solve the macroscopic problem, a relation between the variation of the macroscopic heat flux and the variation of the macroscopic temperature gradient is required, which is written as

$$\delta \underline{q}_M = \underline{K}_M \delta(\underline{\nabla}_M \theta_M) \quad (5.25)$$

where \underline{K}_M is the macroscopic (tangent) conductivity at integration point level of the macroscopic discretization. To this end, the variation of the macroscopic heat flux

expression equation (5.24) is taken:

$$\delta \underline{q}_M = \begin{bmatrix} \underline{L}_n & \underline{L}_c \end{bmatrix} \begin{bmatrix} \delta \underline{q}_n^{ext} \\ \delta \underline{q}_c^{ext} \end{bmatrix} \quad (5.26)$$

Considering the system of equations in a converged micro energy balance state [90], the variations $\delta \underline{q}_n^{ext}$ and $\delta \underline{q}_c^{ext}$ can be extracted as,

$$\begin{bmatrix} \delta \underline{q}_n^{ext} \\ \delta \underline{q}_c^{ext} \end{bmatrix} = \begin{bmatrix} -\underline{T}^T \underline{K}_{ee} \underline{G} \\ -\underline{K}_{ce} \underline{G} \end{bmatrix} \delta \underline{\Upsilon}_M \quad (5.27)$$

where the variations of the macroscopic quantities (loading terms) are involved. Using this relation in equation (5.26) finally yields the macroscopic tangent conductivity as,

$$\underline{K}_M = (-\underline{L}_n \underline{T}^T \underline{K}_{ee} \underline{G} - \underline{L}_c \underline{K}_{ce} \underline{G}) \quad (5.28)$$

RVE-BVP coupled to the macroscopic mechanical pass

On an updated micro-domain (RVE at t_n passed to micro level in the macroscopic mechanical pass, see table 5.1), the system is excited by the periodically micro-fluctuating displacement boundary conditions (see equations (5.9a) and (5.9b)) which can be expressed in a constraint form as,

$$\vec{x}_R = \vec{x}_L + \vec{x}_2 - \vec{x}_1 \quad (5.29a)$$

$$\vec{x}_T = \vec{x}_B + \vec{x}_4 - \vec{x}_1 \quad (5.29b)$$

where $\vec{x}_L, \vec{x}_R, \vec{x}_B$ and \vec{x}_T denote current position vectors of the periodic points of the corresponding boundaries and $\vec{x}_i, i = 1, 2, 4$ are the position vectors of the corner nodes 1, 2 and 4 (see figure 5.2). Furthermore, with the updated temperature and temperature gradient calculated at each macroscopic integration point, the periodically micro-fluctuating temperature profile is enforced within the micro-domain as explained in section 5.5.2. The resulting thermo-mechanical problem is solved in a staggered way.

The discretization of the weak form of the microscopic equilibrium equation yields a system of (non-)linear algebraic equations in the nodal displacements \underline{u} which can be written as,

$$\underline{f}_{int}(\underline{u}) = \underline{f}_{ext} \quad (5.30)$$

with \underline{f}_{int} and \underline{f}_{ext} , the internal and external nodal forces, respectively. Linearization leads to the system of equations, as expressed in equations (5.14a) and (5.15a), written in a compact form as

$$\underline{K} \delta \underline{u} = \delta \underline{r} \quad (5.31)$$

where $\delta \underline{r}$ is the column with the out of balance residual forces. As a result of the periodically micro-fluctuating displacement boundary conditions, the displacement vectors of the corner nodes 1,2 and 4 are kinematically fully prescribed by,

$$\vec{u}_i = (\mathbf{F}_M - \mathbf{I}) \cdot \vec{X}_i \quad (5.32)$$

where the node corresponding to corner 1 is fixed to eliminate rigid body translations. The displacement of the node located at corner 3 is fully described by the displacement of corner 2 and corner 4. Therefore it is not an independent quantity anymore and consequently does not appear in the equations. Furthermore, as emphasized in the macroscopic thermal pass, the discretization of opposite sides of the RVE matches geometrically.

In the discrete setting, periodically micro-fluctuating displacement boundary conditions are handled through standard linear dependencies, $\delta \underline{u}_d = \underline{C}_{id} \delta \underline{u}_i$ with \underline{u}_i the independent displacement degrees of freedom (dofs) and \underline{u}_d the dependent dofs, mutually linked through the linear dependency matrix \underline{C}_{di} . Eliminating the dependent dofs from equation (5.31) leads to a condensed system

$$\underline{K}^* \delta \underline{u}_i = \delta \underline{r}^* \quad (5.33)$$

which is further decomposed to account for the different contributions emanating from the macroscopically prescribed dofs, $\delta \underline{u}_p$ and the remaining free dof variations, $\delta \underline{u}_f$. At equilibrium of the RVE, this partitioned system reads,

$$\begin{bmatrix} \underline{K}_{pp}^* & \underline{K}_{pf}^* \\ \underline{K}_{fp}^* & \underline{K}_{ff}^* \end{bmatrix} \begin{bmatrix} \delta \underline{u}_p \\ \delta \underline{u}_f \end{bmatrix} = \begin{bmatrix} \delta \underline{f}_p^* \\ \underline{0} \end{bmatrix} \quad (5.34)$$

where $\delta \underline{f}_p^*$ corresponds to the variations of the external forces at the prescribed nodes. By condensing out the free degrees of freedom from the system, a reduced stiffness matrix linking $\delta \underline{f}_p^*$ and $\delta \underline{u}_p$ can be obtained as,

$$\underline{K}_M^* \delta \underline{u}_p = \delta \underline{f}_p^* \text{ with } \underline{K}_M^* = \underline{K}_{pp}^* - \underline{K}_{pf}^* (\underline{K}_{ff}^*)^{-1} \underline{K}_{fp}^* \quad (5.35)$$

which will be used for the extraction of the macroscopic material tangent.

Extraction of the macroscopic stresses

The volume average of the microscopic 1st PK stresses can be converted into the following integral form,

$$\mathbf{P}_M = \frac{1}{V_0} \int_{\Gamma_0} \vec{p} \vec{X} d\Gamma_0 \quad (5.36)$$

for which the microscopic equilibrium and the identity $\vec{\nabla}_0 \vec{X} = \mathbf{I}$ are used and \vec{p} is defined as $\vec{p} = \mathbf{P}_m \cdot \vec{N}$, where \vec{N} is the unit outward normal to Γ_0 , [18]. After the solution of the micro-BVP, it can be verified that, in case of periodically micro-fluctuating displacement boundary conditions, the boundary integral (equation (5.36)) takes the following simple form,

$$\mathbf{P}_M = \frac{1}{V_0} \sum_{i=1,2,4} \vec{f}_i \vec{X}_i \quad (5.37)$$

where $\vec{f}_i, i=1,2,4$ are the external forces at the three prescribed corner nodes, [18]. The macroscopic Cauchy stresses can be obtained from \mathbf{P}_M by a classical push-forward $\boldsymbol{\sigma}_M = \frac{1}{\det \mathbf{F}_M} \mathbf{P}_M \cdot \mathbf{F}_M^T$.

Extraction of the macroscopic stiffness

For a constitutive relation formulated in the conjugate pair \mathbf{P} and \mathbf{F} , the material tangent is the fourth order tensor \mathbb{A} which satisfies the linear relation,

$$\delta \mathbf{P} = \mathbb{A}_M : \delta \mathbf{F} \quad (5.38)$$

Reconsidering equation (5.37), in a variational format,

$$\delta \mathbf{P}_M = \frac{1}{V_0} \sum_{i=1,2,4} \delta \vec{f}_i \vec{X}_i \quad (5.39)$$

in combination with the expression for $\delta \underline{f}_p^*$ (see equation (5.35)) and $\delta \vec{u}_j = \delta \mathbf{F}_M \cdot \vec{X}_j$, with $j = 1, 2, 4$ leads to the consistent tangent operator \mathbb{A}_M (see [17, 18] for the derivation) according to

$$\mathbb{A}_M = \frac{1}{V_0} \sum_i \sum_j (\vec{X}_i \underline{K}_M^{*(ij)} \vec{X}_j)^{LC} \quad i, j = 1, 2, 4 \quad (5.40)$$

where the left conjugation implies, $T_{ijkl}^{LC} = T_{jikl}$. \underline{K}_M^* is a 6×6 matrix for a 2-D RVE configuration and $\underline{K}_M^{*(ij)}$ is a square sub-matrix of \underline{K}_M^* corresponding to the dofs of the nodes i and j ($i, j = 1, 2, 4$).

Once \mathbb{A}_M is obtained, the required material tangent in an updated Lagrangian framework can be derived through a push-forward (see [97]) written in index notation as

$$C_{pqmn} = F_{qJ} A_{pJmS} F_{nS} - J \delta_{mp} \sigma_{nq} \quad (5.41)$$

where C_{pqmn} is the material tangent consistent with equation (5.15a), $J = \det \mathbf{F}_M$ and δ_{mp} is the Kronecker delta.

5.6 Two-scale Homogenization Examples

The proposed two-scale thermo-mechanical framework has been implemented in a commercial FE environment (MSC MARC), and is next demonstrated by two example problems. The selected problems are 2-D, preferred due to computational cost reasons, although the presented framework is applicable to 3-D cases as well.

5.6.1 Thermo-mechanically loaded plate

In figure 5.3, a long plate, made of boron fiber reinforced aluminum is shown. The fibers are unidirectionally oriented parallel to the z-axis. The plate is clamped on its side surfaces and exposed to a rapidly increasing uniform temperature and mechanical load on the top surface. The final temperature of 250 °C is reached in 10 seconds (in 50 steps) on the top surface whereas the temperature at the bottom surface is kept constant at $T_0 = 20\text{ °C}$. The uniformly distributed mechanical load has a final value of 100 N/m², which is reached in 10 seconds as well. The problem can be idealized as a plane strain problem (no deformation in z-direction) and due to symmetry, only one half of the plate is modeled with 120 eight-noded elements with a reduced integration scheme. The boundary conditions and the dimensions are sketched in figure 5.3. It is assumed that the geometrical pattern of the fibers is regular so that the underlying microstructure can be fully described by a two-phase unit cell visualized in figure 5.3, which serves as the representative volume element (RVE) for the microstructural computations.

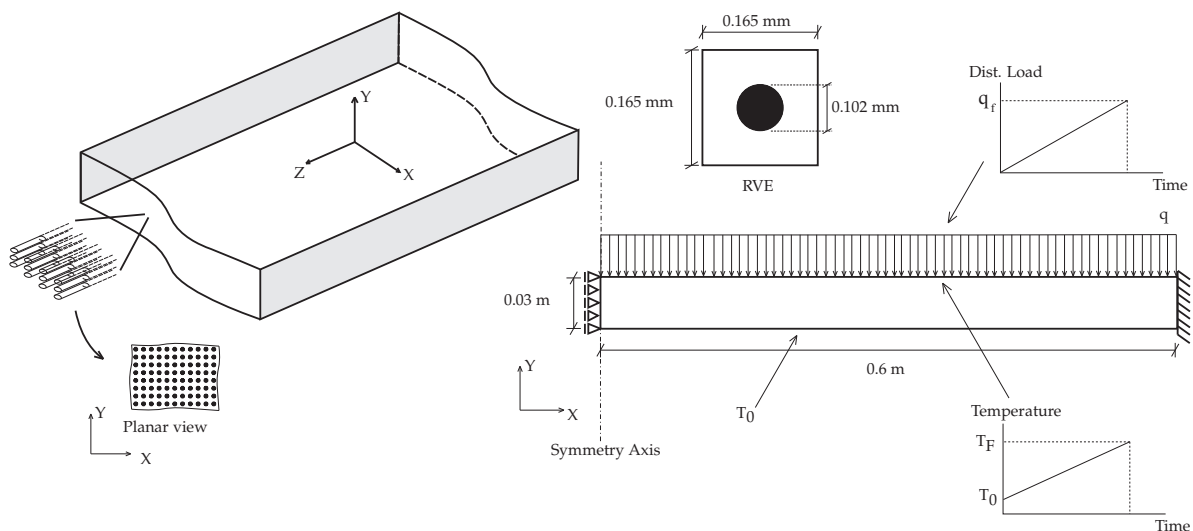


Figure 5.3: Thermo-mechanically loaded plate; geometry, boundary conditions and RVE

Mechanically, the boron fibers are linearly elastic with a modulus of elasticity $E = 385$ GPa, Poisson's ratio $\nu = 0.2$, and a coefficient of thermal expansion $\alpha = 5.0 \cdot 10^{-6}/\text{°C}$.

The aluminum matrix is taken to be elasto-plastic with isotropic hardening. The corresponding mechanical parameters for the matrix are, $E = 75$ GPa, $\nu = 0.33$, $\alpha = 2.36 \cdot 10^{-5}/^{\circ}\text{C}$, with a yield stress $\sigma_y = 300$ MPa and a hardening modulus $h = 150$ MPa. Thermally, both constituents are described by Fourier's law with the temperature independent material data for the fibers, given by their conductivity $K = 38$ W/mK and their heat capacity, $c_v = 1.3$ kJ/kgK. The corresponding material data set for the matrix is, $K = 247$ W/mK and $c_v = 0.9$ kJ/kgK. The densities used for the heat storage capacity calculations are $\rho = 2600$ kg/m³ for the fibers and $\rho = 2700$ kg/m³ for the matrix, respectively. At the RVE level, 4-noded quadrilaterals with a constant dilatation formulation are used for the discretization. A convergence criterion which compares the maximum residual and maximum reaction forces, is used at the RVE level and the ratio is forced to be smaller than 10^{-8} , in order to obtain accurate results for quantities to be transferred to the macro level. The same convergence criterion with a threshold of 10^{-3} is used at the macro level.

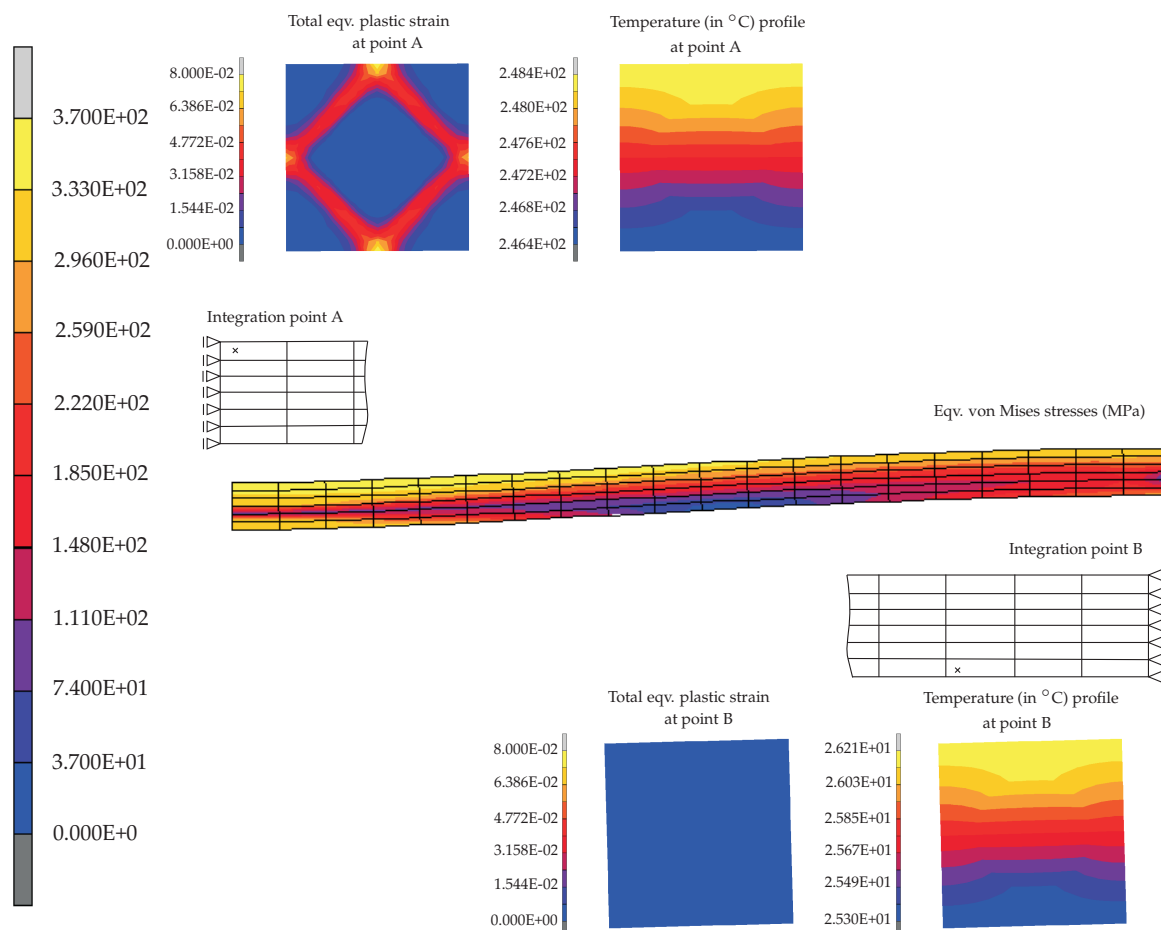


Figure 5.4: Two scale solution via computational homogenization at $t=10.0$ seconds

For comparison purposes, the same problem is analyzed with a Taylor approach and

a modified Sachs approach. Basically, the Taylor approach assumes that: (I) mechanically both phases experience the same deformation and (II) thermally the same temperature gradient is effective within each phase. Therefore traction and heat flux continuity across the fiber matrix interface will be violated. On the other hand, the classical Sachs approach enforces that stresses and fluxes are same in both phases while the ‘macroscopic’ displacement gradient and the temperature gradient are assumed to be the weighted sum (by volume fractions) over the two phases. Here a slight modification is introduced assuming that the rotation tensors in both phases are identical. It is noteworthy to mention that most relatively simple and more accurate alternative methods [98,99] are applicable only in a uni-axial stress/strain state.

In figure 5.4, the deformed configuration of the plate with the resulting von Mises stresses is presented and two RVE’s which are located at the integration points A and B are depicted. Both the mechanical and thermal fields are shown. From the plastic strain distribution at the micro level, it can be concluded that the matrix experiences severe yielding particularly at the locations of large curvature (e.g., integration point A).

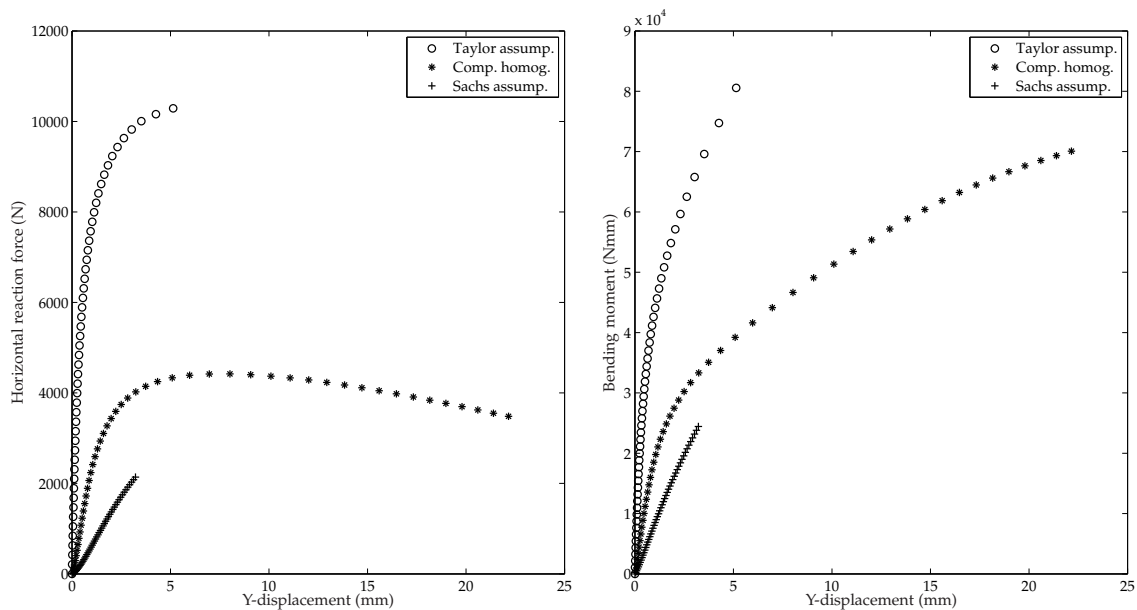


Figure 5.5: Horizontal reaction force and bending moment at the mid-section (sym. axis)

The horizontal reaction force and the bending moment per unit length in z-direction developing at the mid-section (symmetry axis) are presented graphically in figure 5.5. On the horizontal axis, the vertical displacement of the mid-section is given (through the thickness, the variations of the vertical displacements are negligible). The responses obtained through the Taylor assumption and modified Sachs approach are also depicted. For the Taylor solution, (where both phases experience the same deformation) the relatively stiff fiber contributes excessively to the cross-sectional re-

sistance which leads to high axial and bending stiffnesses, reflecting the well-known Taylor upper bound. The Sachs assumption leads to a very compliant structure which does not show any yielding with a smaller axial force and bending moments, typically associated with the lower bound. As expected, the computational homogenization scheme provides a solution in between these two bounds, yet obviously substantially different. Furthermore, to assess the chosen time step size, the problem is solved for four different step sizes which has yielded 25, 50, 100 and 200 steps. The vertical displacement of the mid-section for four different cases is presented in figure 5.6 which clearly shows the convergence of the displacement. Furthermore, the graph also indicates that the chosen step size is sufficiently small to avoid instabilities.

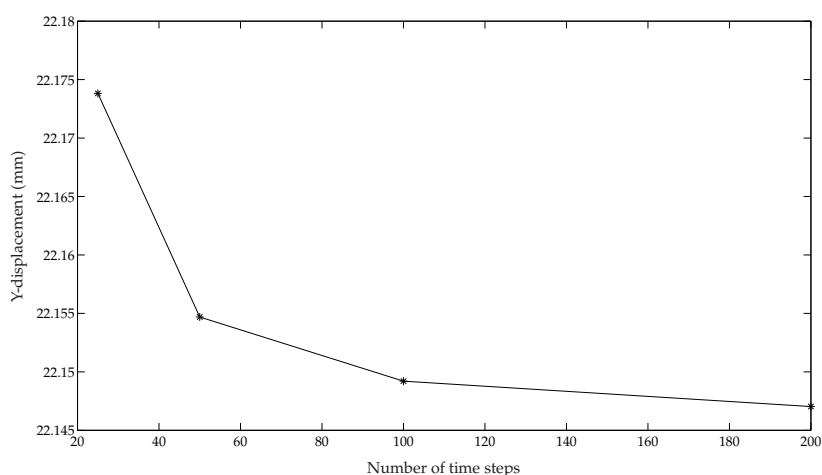


Figure 5.6: Vertical displacement at the mid-section (sym. axis) vs. number of time steps

5.6.2 Thermally shocked channel

In the second example, the thermo-mechanical analysis focuses on a long channel, which is typically used for hot molten metal transport as shown in figure 5.7. Due to symmetry and the high channel length, the problem is idealized as a plane strain problem of the half-width channel for which the corresponding dimensions and boundary conditions are sketched in the figure. The channel is exposed to a temperature shock at the inner surface which reaches a final temperature T_F of 500 °C in 4 seconds starting from an initial temperature T_0 of 20 °C. The outer surface is kept at its initial temperature level throughout the entire loading history.

Due to its high temperature resistance, an alumina based refractory ceramic is typically used for this type of structures. The underlying microstructure is of a granular type with directionally distinct characteristics resulting from the raw base materi-

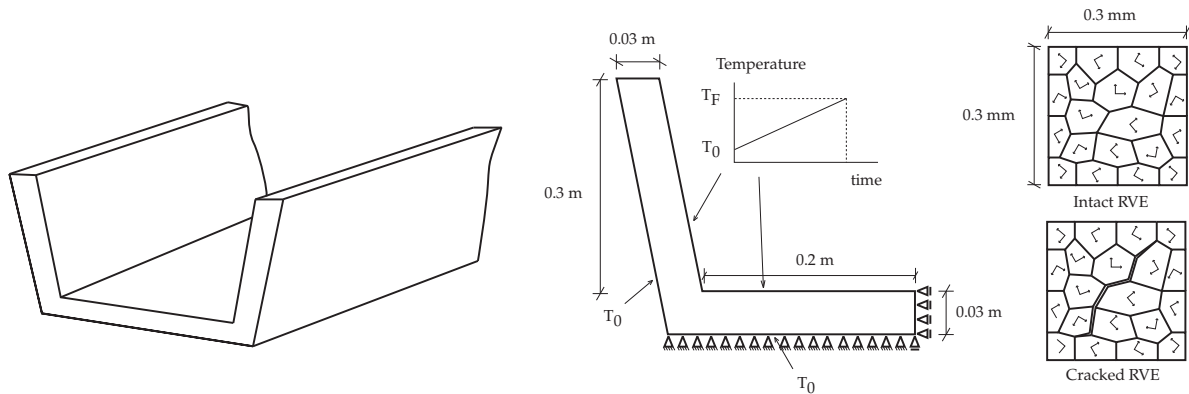


Figure 5.7: Channel exposed to thermal shock; geometry, boundary conditions and RVE's

als and the production process. The RVE's used for the microstructural representation are also shown in figure 5.7. To investigate the effect of prior damage on the thermo-mechanical response, an 'intact RVE' as well as a diagonally cracked RVE are considered. The crack in the latter is modeled by assuming a locally degenerated mechanical stiffness and thermal properties of air within the crack domain. Both mechanically and thermally, it is assumed that individual grains at the RVE level have an anisotropic behaviour. The principal directions of anisotropy are differently oriented from grain to grain as indicated in figure 5.7.

Based on the crystal structure (tetragonal) of Alumina [100], anisotropic mechanical constants equal to $c_{11} = 465$ GPa, $c_{22} = 465$ GPa, $c_{33} = 563$ GPa, $c_{12} = 124$ GPa, $c_{13} = 117$ GPa, $c_{44} = 233$ GPa are used [34]. The principal values of the conductivity tensor are 38 W/mK and 10 W/mK. Heat capacity and the density are taken to be $c_v = 120$ J/kgK and $\rho = 2700$ kg/m³, respectively. The principal directions of the grains are distributed randomly. Both at micro and macro level, the same convergence norms as used in the first problem are employed.

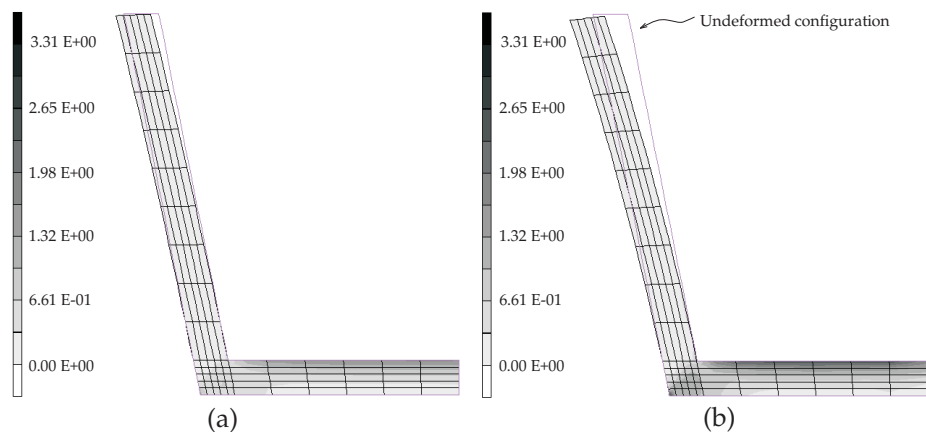


Figure 5.8: Macroscopic equivalent von Mises stresses obtained by computational homogenization; (a) based on intact RVE (b) based on pre-damaged RVE

To investigate qualitatively the effect of thermo-mechanical damage (i.e. disconnected grains) e.g. due to abrupt temperature changes and cycles, the equivalent macroscopic response is also predicted using the RVE with prior damage (see figure 5.7). In figure 5.8, the resulting von Mises stresses obtained at the end of the loading history are visualized. As seen from the contour plot, the maximum stress values are reached on the horizontal part of the channel and the inclined part experiences limited stresses due to the lack of boundary constraints there. Mechanically, the crack leads to a more flexible response which results in larger displacements.

In figure 5.9, the temperature and the equivalent von Mises stresses in a typical cross-sections are presented. The difference between the maximum stresses obtained by the rule of mixture (which is presented for comparison purposes) and the computational homogenization is about 30 % which would make a significant difference for crack initiation predictions. The difference between the two solutions for the temperature profile reaches about 10 % at the centre of the cross-section which remains significant.

In figure 5.10, the microscopic von Mises stresses and the temperature profiles of the intact and pre-damaged RVE's, which are located at the same macroscopic position, are depicted. Obviously, the crack leads to a significant change in the thermal and mechanical response, both qualitatively and quantitatively.

5.7 Summary and Conclusion

Motivated by the results obtained in [17,75] and [90], a two-scale analysis framework for the thermo-mechanical analysis of heterogeneous solids has been presented. Thermo-mechanical approaches at both scales are treated consistently and linked by a rigorous scale bridging procedure. Using an extended computational homogenization framework, macroscopic thermal and mechanical excitations are passed to the micro level through appropriate RVE boundary conditions. The resulting microscopic response is homogenized to the macro scale by means of consistent averaging relations. Tangent operators for a coupled FE² solution strategy are derived in a consistent manner. An operator-split implementation has been elaborated, separating thermal and mechanical passes. As demonstrated by the example problems, the method resolves the interaction between the mechanical and thermal fields at the micro level, accounting for temperature dependent microscopic properties. Both coarse scale and fine scale results are revealed, providing insight on the structural level and the material level in a simultaneous manner. Original aspects and the added values of the proposed approach are:

- A rigorous method for the thermo-mechanical analysis of heterogeneous solids has been developed, which does not require explicit macroscopic (homogenized) quantities such as an effective thermal expansion coefficient.
- Anisotropy, nonlinearity and temperature dependence of both mechanical and

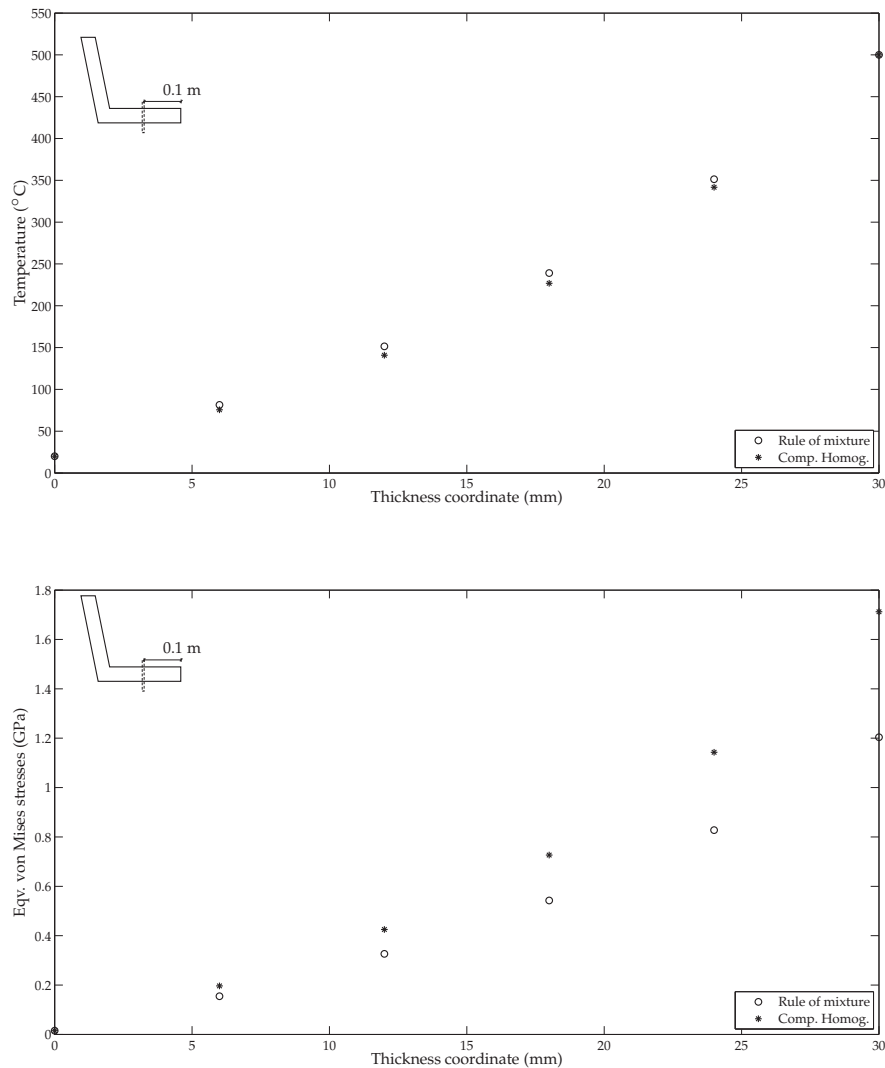


Figure 5.9: Temperature profile and equivalent von Mises stresses along the depicted cross-section

thermal material characteristics can be introduced at the micro level with various morphologies enabling an effective structure-property analysis. Classical homogenization techniques are inadequate in this context if temperature dependent and mechanically non-linear micro-phase properties have to be resolved.

- The interaction between the thermal and mechanical fields is tackled at the micro level and the proposed algorithmic framework has the potential to include further interactions which may result from microstructural evolution (e.g. thermo-mechanical damage and debonding). Failure mechanisms induce a strong coupling between micro and macro scales for which this approach is undoubtedly beneficial.

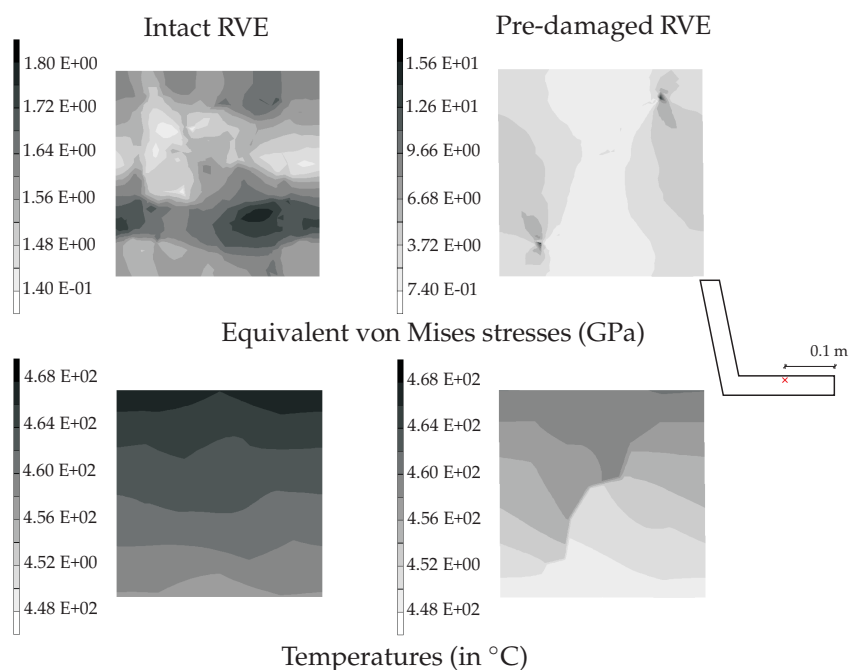


Figure 5.10: Comparison of RVE responses located at the same macroscopic location

- Results obtained through the proposed methodology may serve as a reference for alternative simplified homogenization schemes.

For typical high temperature resistant materials, the failure cannot really be qualified as perfectly brittle, however, the microstructural evolution can be modeled by the use of cohesive zones along the interfaces and diffusive thermo-mechanical damage within different phases. In combination with these techniques, the proposed method can be used to investigate the effect of microstructural variables (both geometrical and physical) on the macroscopic failure initiation including the relation to the underlying thermal and mechanical microstructural evolution. This allows to enhance the understanding and modeling of failure and clarifies the active field interaction effects. These insights cannot be extracted from a single scale phenomenological modeling approach.

Multi-scale Thermo-mechanical Analysis of a Ladle Refractory Lining¹

Abstract

In this chapter, the thermo-mechanical analysis of a refractory ladle structure is carried out by the multi-scale framework outlined in chapter 4 and chapter 5. On the basis of the material microstructure and constitutive models employed in chapter 3, a representative volume element is constructed and a 2-D model of a refractory ladle under pre-heating conditions is analyzed.

¹*Partially reproduced from: I. Özdemir, W.A.M. Brekelmans, M.G.D. Geers. Multi-scale Thermo-mechanical Analysis of a Ladle Refractory Lining. To be submitted.*

6.1 Introduction

Ladles are long, slender structures typically used to transport molten metal between different units in metal processing plants. As schematically shown in figure 6.1, the cross-section consists of multiple layers and for the most inner layer, coarse-grained alumina based refractory materials are used. Under operation conditions, ladles are

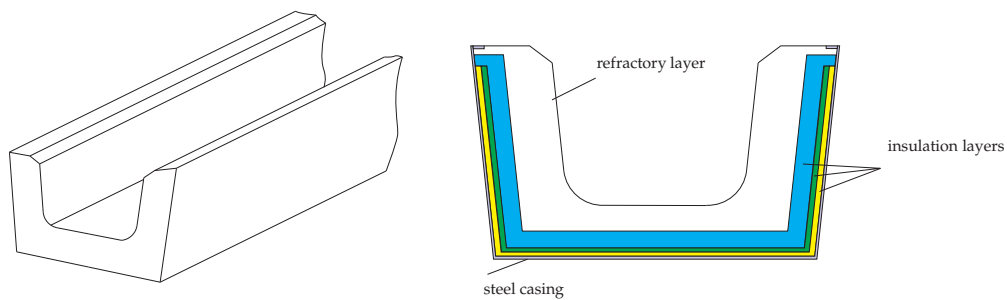


Figure 6.1: Ladle structure and typical cross-section

first pre-heated before they are exposed to molten metal. In this chapter, the thermo-mechanical analysis of a real size ladle structure under pre-heating conditions is carried out using the multi-scale framework presented in chapter 4 and chapter 5. The RVE level microstructural modelling employs the constitutive models and the identified parameters presented in chapter 3.

In the next section, an idealized 2-D representative volume element (RVE) is introduced. Then, the macroscopic boundary value problem along with the loading conditions are specified. Thereafter the analysis results at both scales are presented.

6.2 Representative Volume Element

Referring to chapter 3, the selected microstructure is idealized as a two-phase system where two different sizes of alumina grains are embedded in a matrix which is in fact the representation of a relatively fine grained continuous phase of mullite and small alumina. Based on the volume fractions, the initial grain size distribution and the chemical composition, the representative volume element shown in figure 6.2 is constructed. It should be emphasized that the determination of the RVE size is a rather delicate task and requires an extensive analysis. Furthermore, the representativeness in case of a coupled problem is another issue which hasn't been addressed so far in the literature and is a potential research question for future studies. Here, the geometrical information on the microstructure is taken as the basis for the RVE, whereby the size is deliberately kept reasonable taking into account the limitations of the computational resources. Therefore the results of the analysis are only indicative from a qualitative perspective.

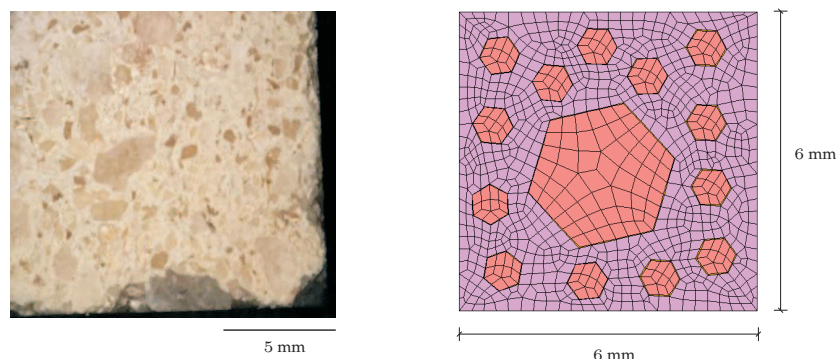


Figure 6.2: Light microscopy image of the microstructure and the simplified representative volume element

The mechanical and thermal constitutive descriptions for each phase and the interfaces have been presented in chapter 3 and therefore not repeated here. Since an implicit gradient damage mechanics formulation is used for the matrix, the multi-scale analysis framework should be extended such that the ‘RVE-BVP coupled to the macroscopic mechanical pass’ (see section 5.5.2) is now a three field problem and the Helmholtz equation (equation (3.17c)) is to be embedded into the staggered solution procedure at the micro level after the solution of the thermal and mechanical fields, successively. The solution procedure and the associated boundary conditions for the Helmholtz equation are presented in chapter 3.

The implementation of the heat storage consistency condition used in chapter 4 and 5 assumes a temperature independent heat storage capacity. Therefore, instead of the temperature dependent heat capacities used in chapter 2, for the grains and the matrix, temperature independent heat capacities of 953.2 J/kg K and 1137 J/kg K are used, respectively. For other material properties, temperature dependent data is given in the figures 6.3 and 6.4 (identical to the data used in chapter 2). The fracture energies and the maximum traction values for the cohesive interfaces are taken as $\phi_n = 25 \text{ J/m}^2$, $\phi_t = 50 \text{ J/m}^2$, $t_n^{\max} = 14 \text{ MPa}$ and $t_t^{\max} = 28 \text{ MPa}$, respectively.

6.3 Macroscopic Boundary Value Problem

The ladle structure is idealized as a plane strain configuration and only half the cross-section is modeled due to the symmetry, as shown in figure 6.5. A two-scale analysis is performed for the inner refractory layer whereas the remaining insulation layers and the steel casing (see figure 6.1 or figure 6.5) are analyzed by a conventional finite element method approach assuming linear elastic behaviour implemented by the temperature independent material parameters given in table 6.1. For the macroscopic discretization within the refractory layer 141 8-noded reduced integrated quadrilaterals are used. For the RVE level model, 4-noded quadrilaterals and 2-noded inter-

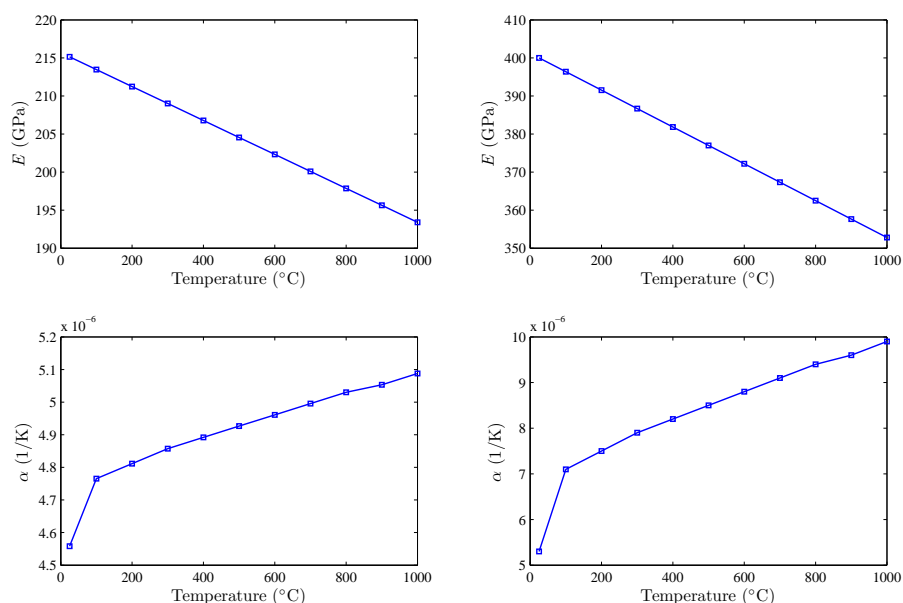


Figure 6.3: Temperature dependency of Young's Modulus (E) and the coefficient of thermal expansion (α), left column for the matrix, right column for the grains; based on [47–50]

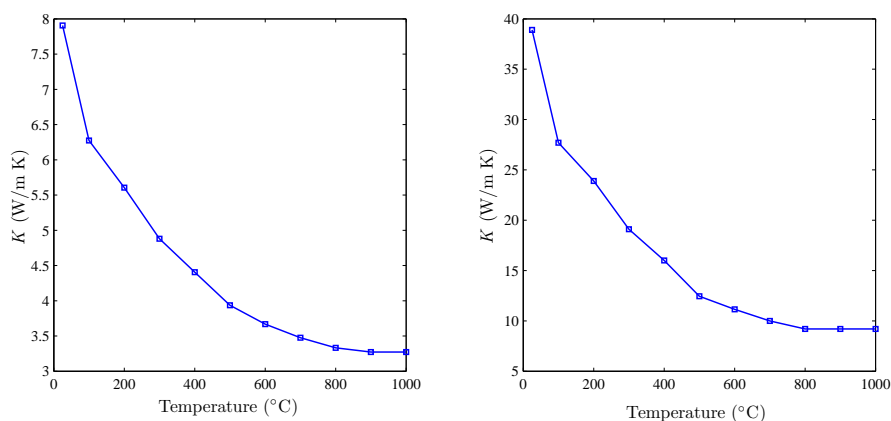


Figure 6.4: Temperature dependency of the conductivity (K) left column for the matrix, right column for the grains; based on [50–53]

face elements (totally 1118 elements) are employed.

As shown in figure 6.5, the structure is mechanically supported and a convective type boundary condition is applied on the inner surface with a heat transfer coefficient of $h = 1.5 \text{ W}/\text{m}\cdot\text{K}$. Initially, the temperature throughout the structure is $25 \text{ }^{\circ}\text{C}$. The ambient temperature is taken to be $1100 \text{ }^{\circ}\text{C}$ and the duration of the heat transfer is 12 hours, which is completed in 60 time steps.

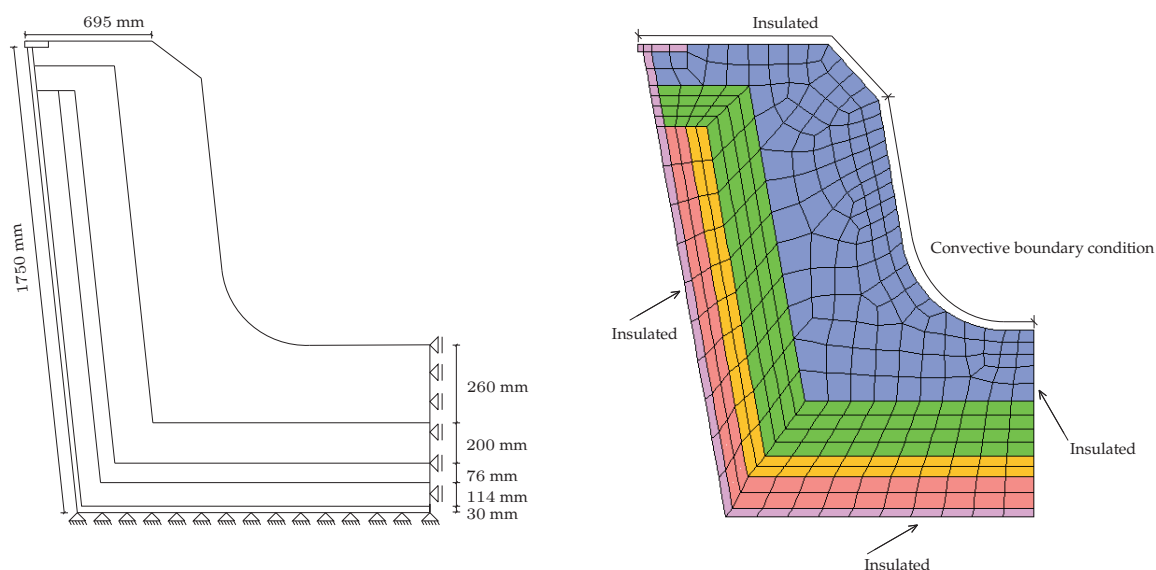


Figure 6.5: Dimensions, boundary conditions and discretization

	Steel casing	Insulation layers
$E(\text{GPa})$	205	220
ν	0.3	0.25
$\alpha(1/\text{K})$	$1.23 \cdot 10^{-5}$	$4.5 \cdot 10^{-6}$
$K(\text{W/m K})$	50	2.5
$c_v(\text{J/kg K})$	447	1000
$\rho(\text{kg/m}^3)$	7850	2975

Table 6.1: Material parameters used for different layers

6.4 Analysis Results

The multi-scale analysis is carried out up to the moment of the macroscopic localization. In figure 6.6, macroscopic temperature distribution and equivalent von Mises stress distribution is shown, when the temperature at the surface of the lining reaches 326.4 °C. At this stage the macroscopic temperature gradient is large, which has a marked influence on the micro-mechanical response. Since the macroscopic temperature gradient reaches its maximum during the initial phase of temperature loading, the matrix and interface damage evolution in the RVE are likely dominant.

The corresponding RVE responses at two representative macroscopic integration points are given in figures 6.7, 6.8, 6.9 and 6.10, respectively. In addition to various mechanical and thermal quantities (see figure 6.7 and figure 6.9), the evolution of matrix and interfacial damage are resolved at the RVE level.

These results can be beneficial to investigate the potential crack initiation locations and the role of the geometry of the microstructural constituents, e.g. grain sizes,

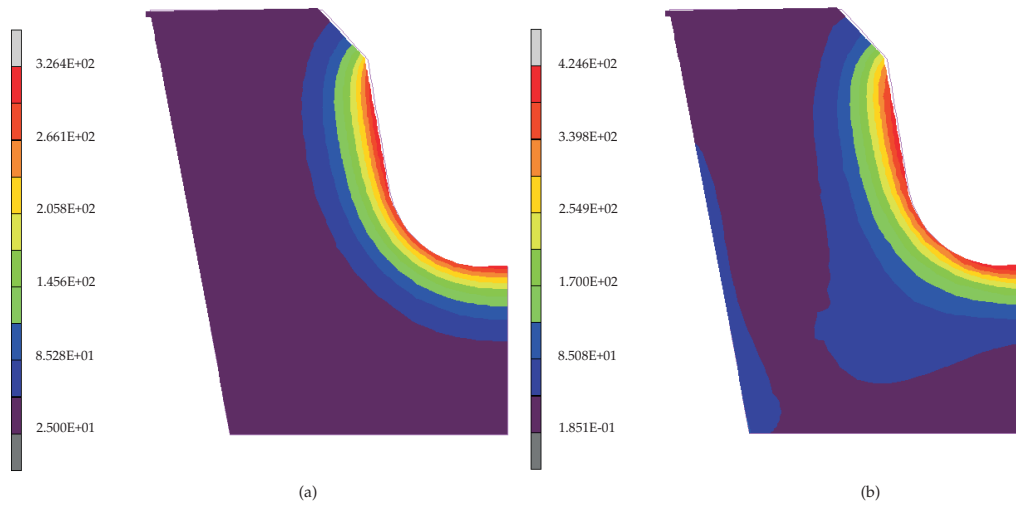


Figure 6.6: Macroscopic response when the maximum temperature at the surface of the lining reaches to 326.4 °C, (a) temperature (°C) (b) equivalent von Mises stress (MPa)

which can be varied to retard the damage initiation and evolution. As seen in figure 6.8 and 6.10, the effective openings along the larger grain-matrix interfaces are more significant and initiate earlier than those of smaller grains. As far as the damage evolution is concerned, the compressive regions between the large grains and the surrounding smaller grains are the critical zones, which is also closely related with the evolution of interfacial damage. The interplay between the interfacial and the matrix damage in conjunction with the grain size and distances between them can be further investigated to optimize the microstructural response under thermal loading conditions. Furthermore, all the parametric variations carried out in chapter 3, can be incorporated within the multi-scale analysis framework as well.

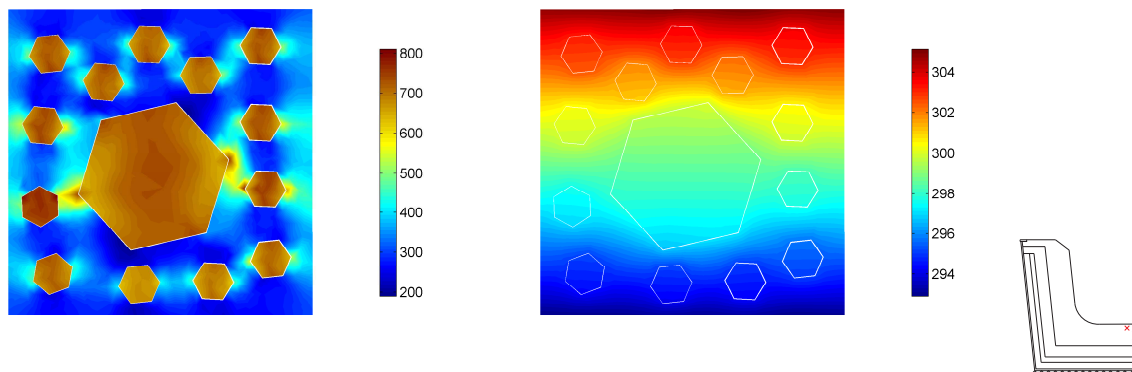


Figure 6.7: Microscopic response at the depicted macroscopic integration point; left: equivalent von Mises stress (MPa), right: temperature (°C)

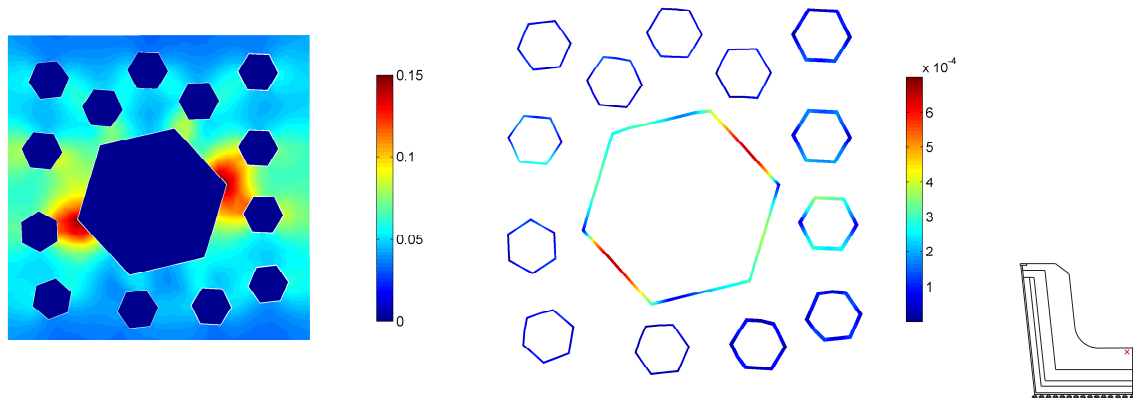


Figure 6.8: Microscopic response at the depicted macroscopic integration point; left: damage, right: effective interface opening (mm)

Beyond the initiation of macroscopic localization, the scale separation is violated and the physical representativeness of the microscopic response is lost. As soon as the macroscopic localization is triggered, the macroscopic deformation gradient varies non-smoothly (as compared to RVE size) within the localization region, violating the basic assumption of macro-micro scale bridging structure. It is also important to note that the precise onset of localization is not further investigated here, since this may be quite sensitive to the boundary conditions applied to the RVE.

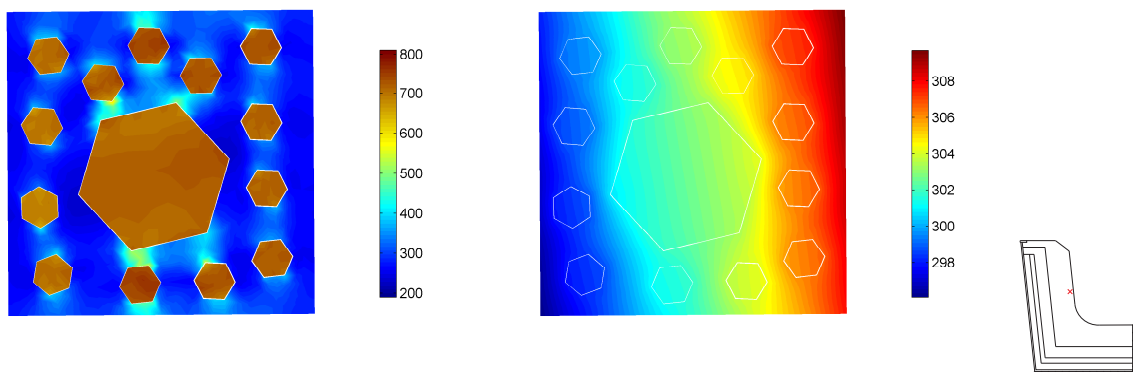


Figure 6.9: Microscopic response at the depicted macroscopic integration point; left: equivalent von Mises stress (MPa), right: temperature (°C)

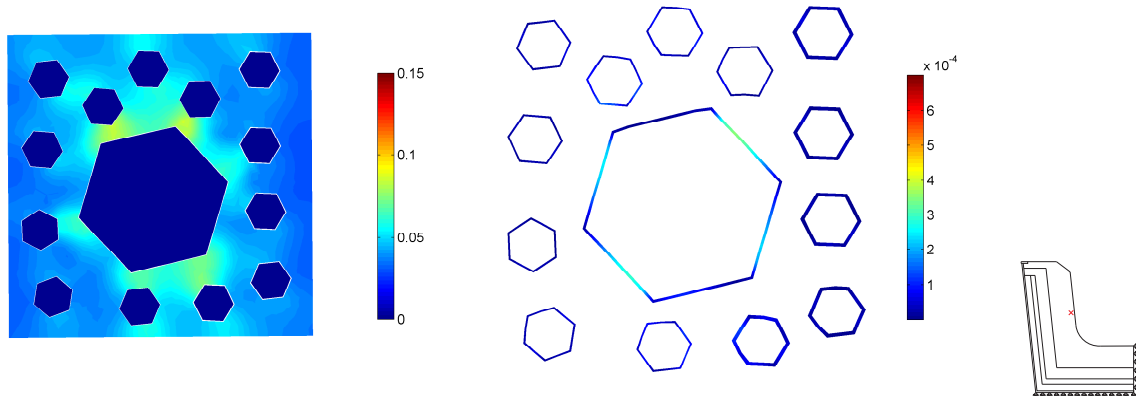


Figure 6.10: Microscopic response at the depicted macroscopic integration point; left: damage, right: effective interface opening (mm)

6.5 Summary and Conclusion

In this chapter, the proposed multi-scale framework along with the identified parameters in chapter 3, is used to analyze the macroscopic response of a refractory lining of a real size ladle. Using certain idealizations, a representative volume element is constructed where essential damage mechanisms are incorporated. Within the limitations of the underlying theory (principle of scale separation), the proposed methodology can be used to investigate qualitatively the influence of different microscopic parameters, both geometrical and physical, on the initiation of macroscopic unstable crack. The presented case study highlights the potential of the proposed multi-scale analysis framework to investigate the thermo-mechanical damage mechanisms at the micro level along with the parameter variations. The link between the macroscopic response and the microstructure can be systematically examined in the context of thermal shock type loading conditions.

CHAPTER SEVEN

Conclusion and Outlook

The research work presented in this thesis aimed to develop a multi-scale framework to model thermo-mechanical behaviour of refractory type heterogeneous materials, under severe thermal loading conditions. To this end, with a particular focus on coarse grained refractory ceramics, a number of different aspects have been addressed at two distinct scales. The multi-scale paradigm based on the computational homogenization technique has been extended for thermal and thermo-mechanical analyses of heterogeneous solids. The description of the decohesion process at the grain-matrix interface level is enhanced with a thermal/cohesive zone concept by which the obstruction of heat transport through damaging material interfaces can be taken into account. For the majority of the multi-scale models, the predictive capabilities rely on the availability of the local mechanical and thermo-physical properties at the constituent level. In the research described in this thesis these properties have been determined through direct numerical simulations of molten aluminium thermal shock tests. Finally, the developed framework is assessed by means of the two-scale analysis of a real size ladle refractory lining, based on the identified microstructural parameters.

As far as the developed computational tools are concerned, the essential characteristics and the findings can be summarized as follows:

- The presented thermo-mechanical cohesive zone description is suitable for the analysis of material interfaces at different scales. The physical heat transport mechanisms are taken into account within the limitations of a macroscopic cohesive zone formulation. As the heat conduction characteristics evolve due to interfacial damage, the heat flow pattern and local stress state may change significantly. Therefore, the proposed formulation assists in acquiring a better understanding of the failure initiation and propagation under severe thermal loading conditions.
- A rigorous multi-scale strategy for the heat conduction analysis in heteroge-

neous solids has been developed. The approach is particularly superior when the coupling between micro and macro scales becomes stronger, e.g. in case of a temperature sensitive microstructural response or for materials with an evolving microstructure.

- A rigorous method for the thermo-mechanical analysis of heterogeneous solids has been developed, which does not require explicit macroscopic (homogenized) quantities such as an effective thermal expansion coefficient.
- Anisotropy, non-linearity and temperature dependence of both mechanical and thermal material characteristics can be introduced at the micro level with various morphologies enabling an effective structure-property analysis. Classical homogenization techniques are inadequate in this context if temperature dependent and mechanically non-linear micro-phase properties have to be resolved.
- The interaction between the thermal and mechanical fields is tackled at the micro level and the proposed algorithmic framework has the potential to include further interactions which may result from microstructural evolution (e.g. thermo-mechanical damage and debonding).
- Results obtained through the proposed methodology may serve as a reference solution for alternative simplified homogenization schemes.

Based on a geometrically simplified microstructure, a limited set of parametric studies has been conducted through a direct numerical simulation technique. The following conclusions have been drawn for a two-phase material system under thermal shock loading conditions:

- In case of strong temperature gradients, the damage evolution is markedly sensitive to the CTE mismatch between the phases. Damage values increase significantly as a result of a slight change in the difference between the CTE of the phases.
- The brittleness of the interfaces has a strong influence as long as there exists a strong temperature gradient. More brittle interfaces (with a limited strength) yield higher damage values. However, as the temperature profile gets milder, the influence of the mechanical characteristics of the interfaces becomes less significant.
- For highly heat conductive materials, the damage distribution tends to be uniform throughout the specimen. The influence of the interface parameters diminishes since the deformation mode is approaching a homogenous state. The damage values are smaller due to the fact that the CTE mismatch is the only source of the damage evolution.
- Increasing the stiffness of the matrix has a favorable effect in the context of the thermal shock response since the damage values become smaller.

A more extensive parametric study can be carried out to investigate the distinct effects of different parameters. In this context, the direct numerical simulation approach and the parametric study provide information on the mechanisms of damage evolution and the significance of certain parameters of the material system of interest.

The two-scale analysis of a ladle refractory lining has demonstrated the capabilities of the proposed framework in terms of the representation of micro failure mechanisms that can be accommodated at a RVE level. Furthermore, it is shown that the approach has the potential to assess the influence of different geometrical and physical microstructural parameters in order to retard the initiation of a macroscopic unstable crack.

The main criticism on computational homogenization techniques, namely the computational cost, still holds with an increased expense due to the multi-scale and multi-physics nature of the studied problem. Although substantial gains in computational times can be achieved by parallel computing and selective use of computational homogenization as done in this thesis, a 3-D multi-scale analysis is still prohibitive.

On the theoretical side, probably more important issues have to be addressed since the proposed framework has certain limitations which can be summarized as follows:

- The proposed multi-scale approach relies on a first order computational homogenization framework both for the thermal and mechanical sub-problems. This implies that the macroscopic temperature and strain fields should vary mildly as compared to the microstructural size, more specifically within an RVE size. This imposes limitations on the macroscopic temperature and displacement profiles that can be handled accurately. With respect to the thermal shock conditions, this is a severe restriction. The proposed framework can be extended to handle steep macroscopic temperature profiles following an approach similar to the second order computational homogenization for mechanical problems [75]. However, it should be kept in mind that such an approach would have certain limitations as well and addressing extremely sharp temperature profiles would necessitate some hybrid technique which combines fully resolved models with a multi-scale approach.
- Throughout the thesis, it is assumed that an adequate RVE has been selected although this is a delicate task. The representativeness of the RVE impacts on the predictive capabilities of the model. Furthermore, the coupled problem brings a new challenge into play which is to determine a representative RVE in a thermal, mechanical and thermo-mechanical analysis context. The simplest approach would be to decouple the fields and to establish the appropriateness of RVE's on the basis of thermal and mechanical sub-problems. However, this seems to be yet an open problem and might require more attention in the future.
- The analysis results presented in this thesis are mainly qualitative. Experimen-

tal identification of material parameters at micro-scale is intrinsically difficult and has to be addressed in order to obtain quantitative predictions. Furthermore, in combination with well-identified RVE's and local material properties at the micro-level, a 3-D analysis is necessary since generalization of 2-D analysis results is difficult due to the geometrically complex nature of refractory microstructures.

Bibliography

- [1] Kingery W.D. Factors affecting thermal stress resistance of ceramic materials. *Journal of the American Ceramic Society*, 38-1:3–15, 1954.
- [2] Hasselman D.P.H. Elastic energy at fracture and surface energy as design criteria for thermal shock. *Journal of the American Ceramic Society*, 46-11:535–540, 1963.
- [3] Hasselman D.P.H. Unified theory of thermal shock fracture initiation and crack propagation in brittle ceramics. *Journal of the American Ceramic Society*, 52-11:600–604, 1969.
- [4] Ziegler G. Microstructural aspects of thermal stress resistance of high-strength engineering ceramics - part I. *Zeitschrift für Werkstofftechnik*, 16:12–18, 1985.
- [5] Ziegler G. Microstructural aspects of thermal stress resistance of high-strength engineering ceramics - part II. *Zeitschrift für Werkstofftechnik*, 16:45–55, 1985.
- [6] Lu T.J. and Fleck N.A. The thermal shock resistance of solids. *Acta Materialia*, 46-13:4755–4768, 1998.
- [7] Evans A.G. and Fu Y. Some effects of microcrack on the mechanical properties of brittle solids-I. stress, strain relations. *Acta Metallurgica*, 33:1515–1523, 1985.
- [8] Evans A.G. and Fu Y. Some effects of microcrack on the mechanical properties of brittle solids-II. microcrack toughening. *Acta Metallurgica*, 33:1525–1531, 1985.
- [9] Tvergaard V. and Hutchinson W. J. Microcracking in ceramics induced by thermal expansion or elastic anisotropy. *Journal of the American Ceramic Society*, 71-3:157–166, 1988.
- [10] Laws N. and Lee J. C. Microcracking in polycrystalline ceramics: Elastic isotropy and thermal anisotropy. *Journal of the Mechanics and Physics of Solids*, 37-5:603–618, 1989.

- [11] Ortiz M. and Suresh S. Statistical properties of residual stresses and intergranular fracture in ceramic materials. *Journal of Applied Mechanics*, 60:77–84, 1993.
- [12] Espinoza D.H. and Zavattieri P.D. A grain level model for the study of failure initiation and evolution in polycrystalline brittle materials. part ii: Numerical examples. *Mechanics of Materials*, 35:365–394, 2003.
- [13] Feyel F. *Parallélisme et approches multi-échelles en mécanique des matériaux*. PhD thesis, École Normale Supérieure de Mines de Paris, 1998.
- [14] Miehe C., Schröder J., and Schotte J. Computational homogenization analysis in finite plasticity. simulation of texture development in polycrystalline materials. *Computer Methods in Applied Mechanics and Engineering*, 171:387–418, 1999.
- [15] Miehe C. and Koch A. Computational micro-to-macro transitions of discretized micro-structures undergoing small strain deformations. *Archive of Applied Mechanics*, 72:300–317, 2002.
- [16] Feyel F. and Chaboche J.L. FE² multiscale approach for modeling the elastoviscoplastic behaviour of long fibre sic/ti composite materials. *Computer Methods in Applied Mechanics and Engineering*, 183:1309–330, 2000.
- [17] Kouznetsova V.G., Brekelmans W.A.M., and Baajens F.P.T. An approach to micro-macro modeling of heterogeneous materials. *Computational Mechanics*, 27:37–48, 2001.
- [18] Kouznetsova V.G. *Computational homogenization for the multi-scale analysis of multi-phase materials*. PhD thesis, Eindhoven University of Technology, 2002.
- [19] Massart T.J., Peerlings R.H.J., and Geers M.G.D. Structural damage analysis of masonry walls using computational homogenisation. *International Journal of Damage Mechanics*, 16:199–226, 2007.
- [20] Geers M.G.D., Coenen E., and Kouznetsova V.G. Multi-scale computational homogenization of structured thin sheets. *Modeling and Simulation in Material Science and Engineering*, 15:S393–S404, 2007.
- [21] Van den Bosch M., Schreurs P.J.G., and Geers M.G.D. On the development of a 3d cohesive zone element in the presence of large deformations. *Computational Mechanics*, 42:171–180, 2008.
- [22] Chandra N., Li H., Shet C., and Ghonem H. Some issues in the application of cohesive zone models for metal-ceramic interfaces. *International Journal of Solids and Structures*, 39:2827–2825, 2002.
- [23] Xu X-P. and Needleman A. Void nucleation by inclusion debonding in a crystal matrix. *Modeling and Simulation in Materials Science and Engineering*, 1:111–132, 1993.

- [24] Willam K., Rhee I., and Xi Y. Thermal degradation of heterogeneous concrete materials. *ASCE Journal of Materials in Civil Engineering*, 17:276–285, 2003.
- [25] Hattiangadi A. and Siegmund T. An analysis of the delamination of an environmental protection coating under cyclic heat loads. *European Journal of Mechanics A/Solids*, 24:361–370, 2005.
- [26] Willam K., Rhee I., and Shing B. Interface damage model for thermomechanical degradation of heterogeneous materials. *Computer Methods in Applied Mechanical and Engineering*, 193:3327–3350, 2004.
- [27] Steinmann P. and Häsner O. On material interfaces in thermomechanical solids. *Archives of Applied Mechanics*, 75:31–41, 2005.
- [28] Krol O. *Thermo-mechanical Modeling of Solids and Interfaces*. PhD thesis, Technische Universität Kaiserslautern, 2007.
- [29] Fagerström F. and Larsson R. A thermo-mechanical cohesive zone formulation for ductile fracture. *Journal of the Mechanics and Physics of Solids*, 56:3037–3058, 2008.
- [30] Hattiangadi A. and Siegmund T. A numerical study on interface crack growth under heat flux loading. *International Journal of Solids and Structures*, 42:6335–6355, 2005.
- [31] Tzou D.Y. The singular behaviour of the temperature gradient in the vicinity of a macrocrack tip. *International Journal of Heat and Mass Transfer*, 33:2625–2630, 1990.
- [32] Zavarise G., Wriggers P., Stein E., and Schrefler B.A. Real contact mechanisms and finite element formulation—a coupled thermomechanical approach. *International Journal for Numerical Methods in Engineering*, 35:767–785, 1992.
- [33] Van den Bosch M., Schreurs P.J.G., and Geers M.G.D. An improved description of the exponential Xu and Needleman cohesive zone law for mixed-mode decohesion. *Engineering Fracture Mechanics*, 73:1220–1234, 2006.
- [34] Swain M. *Structure and Properties of Ceramics, Materials Science and Technology, Volume 11*. VCH, 1994.
- [35] Kregting R. Cohesive zone models: Towards a robust implementation of irreversible behaviour. *Eindhoven University of Technology, Department of Mechanical Engineering, Internal Report*, www.mate.tue.nl/mate/showabstract.php/5169, 2005.
- [36] Damhof F., Brekelmans W.A.M., and Geers M.G.D. Experimental analysis of the evolution of thermal shock damage using transit time measurement of ultrasonic waves. *Journal of the European Ceramics Society*, available online, 2009.

- [37] Hasselman D.P.H. Strength behaviour of polycrystalline alumina subjected to thermal shock. *Journal of the American Ceramic Society*, 53-9:490–495, 1970.
- [38] Gupta T.K. Strength degradation and crack propagation in thermally shocked Al_2O_3 . *Journal of the American Ceramic Society*, 55-5:249–253, 1971.
- [39] Joliff Y., Absi J., Glandus J.C., Huger M., and Tossier-Doyen N. Experimental and numerical study of the thermo-mechanical behaviour of refractory model materials. *Journal of the European Ceramic Society*, 27:1513–1520, 2007.
- [40] Andreev K. and Harmuth H. Fem simulation of the thermo-mechanical behaviour and failure of refractories-a case study. *Journal of the Materials Processing Technology*, 143-144:72–77, 2003.
- [41] Gawin D., Pesavento F., and Schrefler B.A. Simulation of damage-permeability coupling in hygro-thermo-mechanical analysis of concrete at high temperature. *Communications in Numerical Methods in Engineering*, 18:113–119, 2002.
- [42] Pearce C.J., Nielsen C.V., and Bicanic N. Gradient enhanced thermo-mechanical damage model for concrete at high temperatures including transient thermal creep. *International Journal for Numerical and Analytical Methods in Geomechanics*, 28:715–735, 2004.
- [43] Damhof F., Brekelmans W.A.M., and Geers M.G.D. Non-local modeling of thermal shock damage in refractory materials. *Engineering Fracture Mechanics*, 75:4706–4720, 2008.
- [44] Özdemir I., Brekelmans W.A.M., and Geers M.G.D. Fe^2 computational homogenization for the thermo-mechanical analysis of heterogeneous solids. *Computer Methods in Applied Mechanics and Engineering*, 198:602–613, 2008.
- [45] Gorter H. et al. Betere temperatuurwissel bestendigheid (btw) eindrapport (in dutch). *Netherlands Organisation for Applied Scientific Research Report*, 2008.
- [46] Damhof F., Tesselaar W., and Van den Eynden J.C. A novel experimental approach to investigate thermal shock damage in refractory materials. *Ceramic Forum International*, 84:75–79, 2007.
- [47] Kumazawa T., Ohta S., Kanzaki S., Sakaguchi S., and Tabata H. Elastic properties of mullite ceramics at elevated temperature. *Journal of Materials Science Letters*, 8:47–48, 1989.
- [48] Ledbetter H., Kim S., and Balzar D. Elastic properties of mullite. *Journal of the American Ceramic Society*, 81-4:1025–1028, 1998.
- [49] Schreuer J., Hildmann B., and Schneider H. Elastic properties of mullite single crystals up to 1400 °C. *Journal of the American Ceramic Society*, 89-5:1624–1631, 2006.

- [50] Morrel R. *Handbook of properties of technical and engineering ceramics*. HSMO publications, 1987.
- [51] Barea R., Osendi M.I., Ferreira J.M.F., and Miranzo P. Thermal conductivity of highly porous mullite material. *Acta Materialia*, 53:3313–3318, 2005.
- [52] Schneider H., Schreuer J., and Hildmann B. Structure and properties of mullite—a review. *Journal of the European Ceramic Society*, 28:329–344, 2008.
- [53] Hildmann B. and Schneider H. Heat capacity of mullite: New data and evidence for a high-temperature phase transformation. *Journal of the American Ceramic Society*, 87-2:227–234, 2004.
- [54] Peerlings R.H.J. *Enhanced Damage Modelling for Fracture and Fatigue*. PhD thesis, Technische Universiteit Eindhoven, 1999.
- [55] de Vree J.H.P., Brekelmans W.A.M., and Van Gils M.A.J. Comparison of non-local approaches in continuum damage mechanics. *Computers and Structures*, 55:581–588, 1995.
- [56] Van den Bosch M. J., Schreurs P.J.G., and Geers M.G.D. An improved description of the exponential Xu and Needleman cohesive zone law for mixed-mode decohesion. *Engineering Fracture Mechanics*, 73-9:1220–1234, 2006.
- [57] Özdemir I., Brekelmans W.A.M., and Geers M.G.D. A thermo-mechanical cohesive zone model. *to be submitted*.
- [58] Boers S. H. A., Schreurs P.J.G., and Geers M.G.D. Operator-split damage-plasticity applied to groove forming in food can lids. *International Journal of Solids and Structures*, 42:4154–4178, 2005.
- [59] Mediavilla J., Peerlings R.H.J., and Geers M.G.D. An integrated continuous-discontinuous approach towards damage engineering in sheet metal forming processes. *Engineering Fracture Mechanics*, 73-7:895–916, 2006.
- [60] Hashin Z. The elastic moduli of heterogeneous materials. *Journal of Applied Mechanics*, 29:143–150, 1962.
- [61] Rosen B.W. and Hashin Z. Effective thermal expansion coefficients and specific heats of composite materials. *International Journal of Engineering Science*, 8:157–173, 1970.
- [62] Gibiansky L.V. and Torquato S. Thermal expansion of isotropic multiphase composites and polycrystals. *Journal of the Mechanics and Physics of Solids*, 45:1223–1252, 1997.
- [63] Noor A.K. and Shah R.S. Effective thermoelastic and thermal properties of unidirectional fiber-reinforced composites and their sensitivity coefficients. *Composite Structures*, 26:7–23, 1993.

- [64] Auriault J. L. Effective macroscopic description of heat conduction in periodic composites. *International Journal of Heat and Mass Transfer*, 26:861–869, 1983.
- [65] Boutin C. Microstructural influence on heat conduction. *Composite Structures*, 38-17:3181–3195, 1995.
- [66] Guedes J.M. and Kikuchi N. Preprocessing and postprocessing for materials based on the homogenization method with adaptive finite element methods. *Computer Methods in Applied Mechanics and Engineering*, 83:143–198, 1990.
- [67] Takano N., Zako M, Kubo F., and Kimura K. Microstructure-based stress analysis and evaluation for porous ceramics by homogenization method with digital image-based modeling. *International Journal of Solids and Structures*, 40:1225–1242, 2003.
- [68] Ghosh S. and Li Y. Voronoi cell finite element model based on micropolar theory of thermoelasticity for heterogeneous materials. *International Journal for Numerical Methods in Engineering*, 38:1361–1398, 1995.
- [69] Jiang M., Jasiuk I., and Ostoja-Starzewski M. Apparent thermal conductivity of periodic two-dimensional composites. *Computational Materials Science*, 25:329–338, 2002.
- [70] Ostoja-Starzewski M. and Schulte J. Bounding of effective thermal conductivities of multiscale materials by essential and natural boundary conditions. *Physical Review B*, 54-1:278–285, 1996.
- [71] Golanski D., Terada K., and Kikuchi N. Macro and micro scale modeling of thermal residual stresses in metal matrix composite surface layers by the homogenization method. *Computational Mechanics*, 19:188–202, 1997.
- [72] Sigmund O. and Torquato S. Design of materials with extreme thermal expansion using a three-phase topology optimization. *Journal of the Mechanics and Physics of Solids*, 45:1037–1067, 1997.
- [73] Smit R.J.M. *Toughness of heterogeneous polymeric systems. A modeling approach*. PhD thesis, Eindhoven University of Technology, 1998.
- [74] Smit R.J.M., Brekelmans W.A.M., and Meijer H.E.H. Prediction of the mechanical behaviour of non-linear heterogeneous systems by multi-level finite element modeling. *Computer Methods in Applied Mechanics and Engineering*, 155:181–192, 1998.
- [75] Kouznetsova V.G., Geers M.G.D., and Brekelmans W.A.M. Multi-scale constitutive modelling of heterogeneous materials with a gradient-enhanced computational homogenization scheme. *International Journal for Numerical Methods in Engineering*, 54:1235–1260, 2002.

- [76] Bigaud D., Goyheneche J.-M., and Hamelin P. A global-local non-linear modeling of effective thermal conductivity tensor of textile-reinforced composites. *Composites: Part A*, 32:1443–1453, 2001.
- [77] Kwon Y. W. and Cho W.M. Multilevel, micromechanical model for thermal analysis of woven-fabric composite materials. *Journal of Thermal Stresses*, 21:21–39, 1998.
- [78] Kwon Y. W. Micromechanical and thermomechanical study of a refractory fiber/matrix/coating system. *Journal of Thermal Stresses*, 28:439–453, 2005.
- [79] Kouznetsova V.G., Geers M.G.D., and Brekelmans W.A.M. Size of a representative volume element in a second-order computational homogenization framework. *International Journal of Multiscale Computational Engineering*, 4:575–598, 2004.
- [80] van der Sluis O., Schreurs P.J.G., Brekelmans W.A.M., and Meijer H.E.H. Overall behaviour of heterogeneous elastoviscoplastic materials: effect of microstructure modelling. *Mechanics of Materials*, 32:449–462, 2000.
- [81] Ostoja-Starzewski M. Towards stochastic continuum thermodynamics. *Journal of Non-equilibrium Thermodynamics*, 27:335–348, 2002.
- [82] Gibson L.J. and Ashby M.F. *Cellular Solids*. Cambridge Solid State Science Series, 1997.
- [83] Lu T. J. and Chen C. Thermal properties and fire retardance properties of cellular aluminium alloys. *Acta Materialia*, 47-5:1469–1485, 1999.
- [84] Chung P.W. and Tamma K.K. Homogenization of temperature-dependent thermal conductivity in composite materials. *AIAA Journal of Thermophysics and Heat Transfer*, 15-1:10–17, 2001.
- [85] Chung P.W. and Tamma K.K. Woven fabric composites-development in engineering bounds, homogenization and applications. *International Journal for Numerical Methods in Engineering*, 45:1757–1790, 1999.
- [86] Moorthy S., Ghosh S., and Liu Y.S. Voronoi cell finite element model for thermo-elastoplastic deformation in random heterogeneous media. *Applied Mechanics Reviews*, 47-1:207–221, 2001.
- [87] Fish J. and Shek K.L. Finite deformation plasticity of composite structures: Computational models and adaptive strategies. *Computer Methods in Applied Mechanics and Engineering*, 172:145–174, 1999.
- [88] Fish J. and Yu Q. Multiscale damage modeling for composite materials: Theory and computational framework. *International Journal for Numerical Methods in Engineering*, 52:161–192, 2001.

- [89] Matouš K., Kulkarni M.G., and Geubelle P.H. Multiscale cohesive failure modeling of heterogeneous adhesives. *Journal of the Mechanics and Physics of Solids*, 56-4:1511–1533, 2008.
- [90] Özdemir I., Brekelmans W.A.M., and Geers M.G.D. Computational homogenization for heat conduction in heterogeneous solids. *International Journal for Numerical Methods in Engineering*, 73-2:185–204, 2008.
- [91] Nemat-Nasser S. and Hori M. *Micromechanics: Overall properties of Heterogeneous Solids*. North-Holland Series in Applied Mathematics and Mechanics, 1993.
- [92] Kanit I., Forest S., Galliet I., Mounoury V., and Jeulin D. Determination of the size of the representative volume element for random composites: Statistical and numerical approach. *International Journal of Solids and Structures*, 40:3647–3679, 2003.
- [93] Zeman J. and M. Šejnoha. Numerical evaluation of effective elastic properties of graphite fiber tow impregnated by polymer matrix. *Journal of the Mechanics and Physics of Solids*, 49-1:69–90, 2001.
- [94] Kouznetsova V.G., Geers M.G.D., and Brekelmans W.A.M. Multi-scale second-order computational homogenization of multi-phase materials: a nested finite element solution strategy. *Computer Methods in Applied Mechanics and Engineering*, 193:5525–5550, 2004.
- [95] McMeeking R.M. and Rice J.R. Finite element formulations for large elastic-plastic deformations. *International Journal of Solids and Structures*, 11:601–616, 1975.
- [96] Bonet J. and Wood R.D. *Nonlinear Continuum Mechanics for Finite Element Analysis*. Cambridge University Press, 1997.
- [97] Simo J.C. and Hughes J.T. *Computational Inelasticity*. Interdisciplinary Applied Mathematics, Springer-Verlag, 2000.
- [98] Byun T.S. and Kim I.S. Stress and strain partition in elastic and plastic deformation of two phase alloys. *Journal of Material Science*, 26:3917–3925, 1991.
- [99] Bouaziz O. and Buessler P. Iso-work increment assumption for heterogeneous material behaviour. *Advanced Engineering Materials*, 6:79–83, 2004.
- [100] Nye J.F. *Physical Properties of Crystals*. Oxford University Press, 1985.
- [101] Hattiangadi A. and Siegmund T. A thermomechanical cohesive zone model for bridged delamination cracks. *Journal of the Mechanics and Physics of Solids*, 52:533–566, 2004.

-
- [102] Hasselman D.P.H. Crack propagation under constant deformation and thermal stress fracture. *International Journal of Fracture Mechanics*, 7-2:157–161, 1971.
- [103] Zhang H.W., Zhang S., Bi J.Y., and Schrefler B.A. Thermo-mechanical analysis of periodic multiphase materials by a multiscale asymptotic homogenization approach. *International Journal for Numerical Methods in Engineering*, 69:87–113, 2007.
- [104] Schmitt N., Burr A., Berthaud Y., and Poirier J. Micromechanics applied to the thermal shock behaviour of refractory ceramics. *Mechanics of Materials*, 34:725–747, 2002.
- [105] Brunauer G., Frey F., Boysen H., and Schneider H. High temperature thermal expansion of mullite: an in situ neutron diffraction study up to 1600 °C. *Journal of the European Ceramics Society*, 21:2563–2567, 2001.
- [106] Munro R.G. Evaluated material properties for a sintered alpha-Al₂O₃. *Journal of the American Ceramic Society*, 80:1919–1928, 1997.

Samenvatting

Met 'vuurvast' wordt een klasse van materialen aangeduid die bestendig zijn tegen (zeer) hoge temperaturen. Deze materialen worden uitgebreid gebruikt in allerlei technische constructies voor een breed spectrum van toepassingen, bijvoorbeeld in de procesindustrie voor de wandbekleding van ovens of voor de realisering van een warmte-isolerende laag. Zulke structuren worden vaak blootgesteld aan extreme thermische belastingen in de vorm van snelle temperatuurwisselingen ('thermo-shock') niet zelden in de vorm van een cyclisch proces. Begrip van de mechanismen die leiden tot falen en de modellering ervan zijn noodzakelijk om betrouwbare levensduurvoorspellingen te kunnen doen voor bestaande constructies en om voorschriften voor het ontwerp van nieuwe constructies te ontwikkelen.

In verband met de hoge bestendigheid tegen thermische belasting is gebruik van vuurvast in de vorm van op aluminiumoxide gebaseerd keramiek, met een verre van homogene poreuze korrelachtige microstructuur, algemeen als gangbaar te beschouwen voor de bovengenoemde toepassingen. In dergelijke heterogene materialen zullen de aanwezige discontinuïteiten in de componentspecifieke thermische uitzettingscoëfficiënten en andere verschillen in de (richtingafhankelijke) materiaaleigenschappen leiden tot het optreden van interne spanningen. Deze interne spanningen kunnen scheurvorming op micro-niveau en andere schade veroorzaken. Bij hoge tijdsafhankelijke thermische belasting zal de resulterende heterogene temperatuurverdeling leiden tot een gecompliceerde mechanische respons, gekenmerkt door een niet-uniforme degradatie van de mechanische en fysische eigenschappen en gepaard gaande met onomkeerbare geometrieveranderingen. Veranderingen in de verdeling van de materiaaleigenschappen zijn van grote invloed op de macroscopische respons bij verdere voortzetting van de externe belasting. Daarom is de macroscopische respons sterk gekoppeld aan de evoluerende microstructuur. Bovendien kunnen microscopische structuurveranderingen tot een aanzienlijke interactie leiden tussen mechanische en thermische velden, bijvoorbeeld in de vorm van een reductie van warmtetransport door schade ter plaatse van contactoppervlakken. Een procedure waarbij met de verschillende mechanismen op een correcte wijze rekening wordt gehouden vormt een geschikt gereedschap om begrip te verkrijgen van de microstructurele invloed van de mechanische en thermische eigenschappen van de diverse componenten en hun interactie.

In dit proefschrift is gekozen voor een zogenaamde ‘concurrent multi-scale’ benadering (een opzet gekarakteriseerd door berekeningen op het niveau van meerdere lengteschalen, waarbij simultaan aan punten op macroscopisch niveau een microscopisch volume-element wordt toegekend) speciaal gericht op grofkorrelig vuurvast keramiek. De werkwijze is in essentie gebaseerd op een rigoureuze uitbreiding van de ruim ingeburgerde FE^2 numerieke homogenisatietechniek waarbij de lokale macroscopische respons wordt bepaald op basis van de oplossing van een randwaarde probleem gedefinieerd voor een representatief volume-element uit de onderliggende microstructuur. In eerste instantie wordt de numerieke homogenisatie uitgewerkt in de context van processen met zuivere warmtegeleiding in heterogene vaste stof media. Daarna volgt de strategie ten behoeve van thermo-mechanische analyses door de eerste-orde mechanische homogenisatie te combineren met de ontwikkelde procedure voor warmtegeleiding, in de vorm van een ‘operator-split’ oplossingsalgoritme bestaande uit incrementeel ontkoppelde vernestelde (FE^2) deeloplossingen voor de thermische en mechanische balansvergelijkingen.

Om voorspellende analyses uit te kunnen voeren moeten voor de individuele componenten op microstructureel niveau en de grensvlakken de mechanische en thermische eigenschappen beschikbaar zijn; dit is karakteristiek voor de gehanteerde multi-scale aanpak. In verband met een gebrek aan relevante kwantitatieve gegevens van de materialen en speciaal van de interfaces wordt een directe numerieke simulatie (DNS) techniek gevolgd om de materiaalparameters op een inverse manier te identificeren, met gebruik van meetresultaten verkregen uit een beperkte set thermo-shock (via gesmolten aluminium) experimenten. Uitgaande van een microstructuur bestaande uit onderling niet-rakende grote korrels ingebed in een homogene matrix die model staat voor een samenstelling van zeer kleine korrels, wordt een thermo-shock test met behulp van realistische randvoorwaarden tot in detail numeriek gesimuleerd. Op basis van de resultaten wordt een aanvullende berekening uitgevoerd leidend tot een maat voor de schade die vergeleken kan worden met uit het experiment volgende schadegegevens. De faalmechanismen optredend in de interface tussen matrix en korrels worden verdisconteerd door de introductie van zogenaamde ‘thermo-mechanische cohesive zone’ elementen die niet alleen de degeneratie van de mechanische samenhang representeren, maar ook het verminderde warmtetransport over de mechanisch beschadigde grensvlakken in rekening brengen. Het effect van microscopisch kleine scheurtjes in het matrixmateriaal wordt denkbeeldig uitgesmeerd door gebruik te maken van klassieke concepten uit de ‘continuüm damage mechanica’ in een zodanige formulering dat ongewenste pathologische lokalisering van de deformatie en mesh-afhankelijkheid worden vermeden. De directe numerieke simulatie van thermo-shock experimenten heeft ook geleid tot inzicht in de ‘short range’ effecten (afkomstig van de lokale verschillen in thermische uitzetting) en ‘long range’ effecten (als gevolg van gradiënten in de temperatuur) op de resulterende verdeling van thermo-mechanische schade, op basis van variaties van de verschillende microstructurele materiaalparameters.

In het laatste gedeelte van dit proefschrift komt ter sprake hoe de hier ontwikkelde numerieke methodiek kan worden ingezet ten behoeve van voorspellingen over het

thermo-mechanisch gedrag van vuurvast configuraties. Voor een realistisch voorbeeld, de vuurvast bekleding van een gietpan, wordt dit gedrag onderzocht waarbij op twee niveau's analyses zijn uitgevoerd. De microstructurele parameters zijn daarbij gekwantificeerd via directe numerieke simulaties.

Acknowledgements

First of all, I would like express my gratitude to my promoter Marc Geers and co-promoter Marcel Brekelmans for their supervision and support throughout these years. The last months were particularly difficult for me and without their careful guidance and help, it would have been hardly possible to finish this work.

I sincerely thank the committee members; prof.dr. N. Bicánić, prof.dr. J. L. Chaboche, dr.ir. Sido Sinnema, prof.dr.-ing. W.A. Wall and prof.dr.ir. B. de With for their interest and constructive comments on this thesis.

I would like to thank the other partners of the BTW project, especially Erik Damhof, Harrie Gorter, Marcel Franken and Johannes Boersma for fruitful discussions and contribution on material characterization. I am thankful to Varvara Kouznetsova whose previous work on parallel implementation helped me a lot. I would also like to thank Henk de Vree and Piet Schreurs, who were very helpful on detailed software problems. My sincere thanks go to Patrick and especially Leo, for their time, effort and solutions. Alice, Marleen and Yvonne, thank you for your kindness.

I would like to acknowledge Johan van den Eynden and Nicholas Feld, who were involved in this work during their internships. Furthermore, I would like to extent my thanks to my colleagues at MaTe; Abdul Matin, Alexei, Arash, Choi, Erica, Gabriel, Hamid, Hans, Kang, Johan, Lars, Matej, Marc, Marco, Mikiel, MK, Murthy, Pieter, Ron, Rudy, Sebastian, Viny, Yuriy; and especially my current and former room-mates, Dafne, Graham, Mahdi, Pina and Linda for the nice working atmosphere.

Atike & Koray, Barış Y., Britta, Seçkin, Çağdaş, İlhan, İsa, Kurtuluş, Mohammad, Müge & William, Tarkan & Sandra and Ulaş; thank you very much for all the good time and help on many things. Furthermore, I would like to express my special thanks to Cem, Frederico, Kanat, Tuncay and Onur for being available during difficult times. It was truly a chance and pleasure for me to come across people like you.

I am also thankful to my landlords Jan & Toon for their hospitality and understanding. It was a big comfort to be your guest. Niels, many thanks for the cover design

on a short notice.

Lastly, I am grateful to my parents, Sultan and Osman Özdemir, my sister Banu and my brother-in-law Hayri Demir for their love and everlasting support. There are no words to express my gratitude to them.

İzzet Özdemir

Eindhoven, May 2009.

Curriculum Vitae

İzzet Özdemir was born in Afyon, Turkey on February 8th, 1976. After completing secondary and high school education at Afyon Kocatepe Anadolu Lisesi, he studied Civil Engineering at Middle East Technical University, Ankara and got his B.Sc. degree in 1999. He worked as a teaching assistant at the same department until August 2001. Afterwards he continued his studies at the University of Stuttgart and got his M.Sc. degree on computational mechanics of materials and structures in 2003. After his graduation, he was employed as a research associate at the Technical University of Munich, Chair of Computational Mechanics from September 2003 to May 2004. Since February 2005, he has been working on multi-scale modeling of thermal shock damage in refractory materials, at the Institute of Materials Technology, Mechanical Engineering Department, TU/e under the supervision of Prof.Dr.Ir. M.G.D. Geers and Dr.Ir. W.A.M. Brekelmans.